

**2001 SUMMER RESEARCH PROGRAM FOR HIGH SCHOOL JUNIORS**  
**AT THE**  
**UNIVERSITY OF ROCHESTER'S**  
**LABORATORY FOR LASER ENERGETICS**

**STUDENT RESEARCH REPORTS**

**PROGRAM COORDINATOR**

**Dr. R. Stephen Craxton**

**March 2002**

**Lab Report 324**

**2001 SUMMER RESEARCH PROGRAM FOR HIGH SCHOOL JUNIORS**

**AT THE**

**UNIVERSITY OF ROCHESTER'S**

**LABORATORY FOR LASER ENERGETICS**

**STUDENT RESEARCH REPORTS**

**PROGRAM COORDINATOR**

**Dr. R. Stephen Craxton**

**LABORATORY FOR LASER ENERGETICS**

University of Rochester

250 East River Road

Rochester, NY 14623-1299

During the summer of 2001, 13 students from Rochester-area high schools participated in the Laboratory for Laser Energetics' Summer High School Research Program. The goal of this program is to excite a group of high school students about careers in the areas of science and technology by exposing them to research in a state-of-the-art environment. Too often, students are exposed to "research" only through classroom laboratories, which have prescribed procedures and predictable results. In LLE's summer program, the students experience many of the trials, tribulations, and

rewards of scientific research. By participating in research in a real environment, the students often become more excited about careers in science and technology. In addition, LLE gains from the contributions of the many highly talented students who are attracted to the program.

The students spent most of their time working on their individual research projects with members of LLE's scientific staff. The projects were related to current research activities at LLE and covered a broad range of areas of interest including optics modeling, laser characterization, cryogenic materials properties, liquid crystal chemistry, laser damage, electro-optic sampling, and the development, modeling, and control of laser fusion diagnostics. The students, their high schools, their LLE supervisors, and their project titles are listed in the table. Their written reports are collected in this volume.

The students attended weekly seminars on technical topics associated with LLE's research. Topics this year included lasers, fusion, holography, the OMEGA Cryogenic Target System, laboratory astrophysics, experimental error analysis, and scientific ethics. The students also received safety training, learned how to give scientific presentations, and were introduced to LLE's resources, especially the computational facilities.

The program culminated on 29 August with the "High School Student Summer Research Symposium," at which the students presented the results of their research to an audience including parents, teachers, and LLE staff. Each student spoke for approximately ten minutes and answered questions. At the symposium the William D. Ryan Inspirational Teacher award was presented to Mr. David Dussault, a mathematics and computer science teacher at Livonia High School. This annual award honors a teacher, nominated by alumni of the LLE program, who has inspired outstanding students in the areas of science, mathematics, and technology.

A total of 130 high school students have participated in the program since it began in 1989. The students this year were selected from approximately 50 applicants. Each applicant submitted an essay describing their interests in science and technology, a copy of their transcript, and a letter of recommendation from a science or math teacher.

LLE plans to continue this program in future years. The program is strictly for students from Rochester-area high schools who have just completed their junior year. Applications are generally mailed out in early February with an application deadline near the end of March. For more information about the program or an application form, please contact Dr. R. Stephen Craxton at LLE.

This program was supported by the U.S. Department of Energy Office of Inertial Confinement Fusion under Cooperative Agreement No. DE-FC03-92SF19460.

### High School Students and Their Projects (2001)

Student	High School	Supervisor	Project
David Bowen	Greece Arcadia	C. Stoeckl	Controlling Scientific Instruments with JAVA
Matthew Fiedler	Brighton	W. Donaldson	Modeling Streak Camera Sweep Speeds
Melisa Gao	Brighton	J. Marozas	Two-Dimensional Phase Unwrapping for the Design of Distributed Phase Plates
Brian Ha	Gates Chili	R. Sobolewski	Optical Characterization of GaAs with MSM Structures
Gabrielle Inglis	Honeoye Falls-Lima	R. Boni	Building and Characterizing 14-GHz InGaAs Fiber-Coupled Photodiodes
Jennifer Jung	Victor	K. Marshall	Guest-Host Dye Systems for Liquid Crystal Electro-Optical Device Applications
Joshua Keegan	Aquinas Institute	M. Guardalben	Numerical Modeling of Optical Parametric Chirped Pulse Amplification to Design a Petawatt Laser Front End
Kevin Monajati	Pittsford-Sutherland	K. Marshall	Computational Modeling of Physical Properties in Liquid Crystalline Polymer Systems
Christopher Piro	Honeoye Falls-Lima	R. S. Craxton	Modeling the LCPDI with Refraction and Diffraction
Abigail Rhode	Brockport	J. Taniguchi	Experimental Simulation of Damage in Spatial Filter Lenses
Uyen Tran	Wilson Magnet	S. Regan	Experimental Investigation of the Far Field on OMEGA with an Annular Apertured Near Field
James Wang	McQuaid Jesuit	D. Harding	Cryogenic Permeability of Polyimide Shells
Jeffrey Wilbur	Victor	J. Lambropoulos	Inclusion Models of Laser Damage

Controlling Scientific Instruments with JAVA  
University Of Rochester Laboratory for Laser Energetics  
Advised by Dr. Christian Stoeckl  
David Bowen

**Abstract**

Recording electrical waveforms on OMEGA is a task that has usually required a computer for controlling oscilloscopes that capture data from the diagnostic equipment. With a new generation of oscilloscopes integrated with a fully functional computer, the oscilloscope can run control software itself, removing the need for a control computer. However, the control software, written in JAVA, must be changed and updated to be operational on this new generation of oscilloscopes. By changing the interface layers of the software, it is possible to apply these changes to all diagnostics software instead of being particular to one program. This means that all of various control programs could easily be updated to operate on the newer oscilloscopes. The software was changed to have more reliable treatment of interface errors and was also changed graphically as to appear friendlier to new users.

**Introduction**

The concept of laser fusion, like the type attempted here at LLE, uses the inertia of an exploding shell to compress two isotopes of hydrogen, Deuterium and Tritium, to high density and high temperature. Some of the Deuterium and Tritium atoms combine to form an intermediate particle immediately breaking down into an Alpha particle and a neutron. As the unstable particle breaks down it releases energy. An important part of the diagnostics of laser fusion is measuring the amount and energy of neutrons escaping the chamber. Though neutron radiation is not the only diagnostic being performed on OMEGA, Dr. Stoeckl was a neutronics scientist so neutron detection was the diagnostic I was made familiar with. These neutrons are measured using scintillating detectors. A scintillating detector consists of scintillating plastic connected to a photomultiplier tube. Neutrons emitted from the chamber hit the scintillating plastic and strike protons in the hydrocarbon molecule of the plastic. The elastically scattered

protons, the neutrons excite the molecules causing them to emit photons, or scintillate. The photons strike an extremely negatively charged photocathode in the photomultiplier tube, causing a serial amplification by knocking one electron into the next plate, knocking more electrons into the next plate, and so on until the photomultiplier tube delivers the resulting charge to an oscilloscope. The signal can then be recorded by an oscilloscope and transferred into a computer for further analysis.

The computer system for controlling oscilloscopes is a bulky and demanding setup. A computer must be connected to the scope using an interface called a GPIB or General Purpose Interface Bus. The only way for a computer to use this connection successfully is if the computer is fitted with a GPIB card. So a computer must not only be loaded with all of the correctly debugged software necessary for control, but also an interface card and its driver software. The computer would also require network capabilities to receive pre-shot notifications. So to receive data properly, the above system would have to be added to the data acquisition location. Though this may not seem to be the worst of possible data acquisition situations, it can be improved.

The most recent models of oscilloscopes have been designed to be a computer operating in parallel with an oscilloscope. The computer side of the newer models runs an operating system that, by default, runs the software that displays the oscilloscopes data. This new generation of oscilloscope is capable of replacing the previous two-machine setup. The oscilloscope would have no need for GPIB hardware and the scope is already fully equipped with networking capabilities. The computer could run the control software in parallel with the oscilloscope and remove the need for any added hardware.

Though conceptually the idea of running the control software on these new oscilloscopes seems a reasonable idea, it requires some interesting reverse engineering. The problem lies with changing all of the control software, which was written to interface with GPIB cards and GPIB cables to an external oscilloscope, so that it now interfaces with the oscilloscope which functions as a part of the new generation of computer/oscilloscope hybrids. Before the potential of these new computer/oscilloscope hybrids can be fully taken advantage of, the current software has to be updated so it can smoothly go from an internal environment to an external GPIB interface.

### **Learning the structure of the Software**

The existing software had been written for GPIB connections. However, now the

software must run on a computer talking to the scope not with GPIB, but through some sort of internal interface.

So, where would this new interface start? Where was the backdoor that could be used to access the data the oscilloscope was capturing? It turns out that the answer lied within software provided by Tektronix® .

The software engineers at Tektronix had written a software interface to allow their own analysis software to run on the scope and to access its data. All one would have to do, is to use the methods of the classes defined by Tektronix® to talk to the internal scope.

From there, I proceeded with further examination of the code of the program and the supplied classes. The program I was using specifically was ScopeControl, a good choice as it was designed for single scope acquisitions. The situation was even better, though, because the software had been written in layers. Each layer was a link from one part of the program to a lower part. The part that I had to update, the interface, was at the very bottom. The layer, or class, named Gpib contained the methods for communicating with the oscilloscopes through a GPIB connection. Since all control software uses the same layering, changes could be made in one copy of Gpib.java, tested using ScopeControl, and then distributed amongst all control programs. However, Gpib now had to be two different classes; one to accommodate internal interface and one to accommodate GPIB interfaces for a program to truly be useful and work with both interfaces.

To first write an interface based on this software by Tektronix®, we must first know what this software contains. Unfortunately, Tektronix® did not supply us with source code. So, to view the contents of the software, it was necessary to disassemble the classes. From doing this, I obtained the knowledge that the class GpibDevice appeared to be the super class of InstGpibBus. GpibDevice seemed to contain mostly private methods and its constructor required an object of InstGpibBus. InstGpibBus revealed the public methods required for the program to operate and communicate properly with the scope. My task was to synthesize a Gpib class with method definitions redefined for the classes provided by Tektronix®. So, by analyzing the disassembled code, I learned about methods that performed the same operations that were required by the interface; *read*, *write*, *clear*, *get*, and *status*.

With the redefined Gpib class and some routine debugging, ScopeControl was able to communicate internally with the scope, using Tektronix® supplied access classes and .DLL's.

## Versatility

At this point, I had successfully created an internal interface, though not efficient or reliable. It was not quite of the quality where it could be reliably used and distributed. In fact, it was certain that the current version of the program would simply not work with a GPIB connection. Further extension was necessary.

A quality that seems to be the mark of a well-written program is automation. The less that the user must define, the more user friendly the program is, the better the program is. However, research may continue into the automation of the GPIB connection selection. As of now, the GPIB connection type is a user defined setting and will result in error if selected incorrectly.

The design of the Gpib setup is another interesting part of this versatile program. There exists the new internal version, *Gpibint* (see figure 1 for a diagram of the structure of the new internal interface), and the external GPIB cable version, *Gpibext*. They were tied together as extensions of a super class, *Gpib*. *Gpib* contained the methods common to both *Gpibint* and *Gpibext*. However, the program still must be told which class file to use. On the user side, this is done with a check box in the settings menu.

## ScopeControl

The program that I subjected to the testing of the internal interface was a program called ScopeControl, its purpose being for a computer to capture data from an oscilloscope, either once or repeatedly as with a log or a run. However, with the new type of oscilloscope capable of writing its data to a hard drive or network drive, many of the functions of ScopeControl are not necessary. The only remaining useful function would be its ability to take and record data in intervals, known as logging. However, the very design of ScopeControl made it an ideal program with which to do testing with scope interfacing. The functions were clear and user executed making this an instant results type of program.

By using ScopeControl and changing it's layers, the goal was achieved of creating the internal interface and making it reliable. Updating ScopeControl was more a tool of education of software layering and design rather than a practical expenditure (see Figure 2 and Figure 3 for screenshots of ScopeControl's user interface before and after the updates). The redesign of ScopeControl did, however, create a user friendly and reliable example of the internal interface.

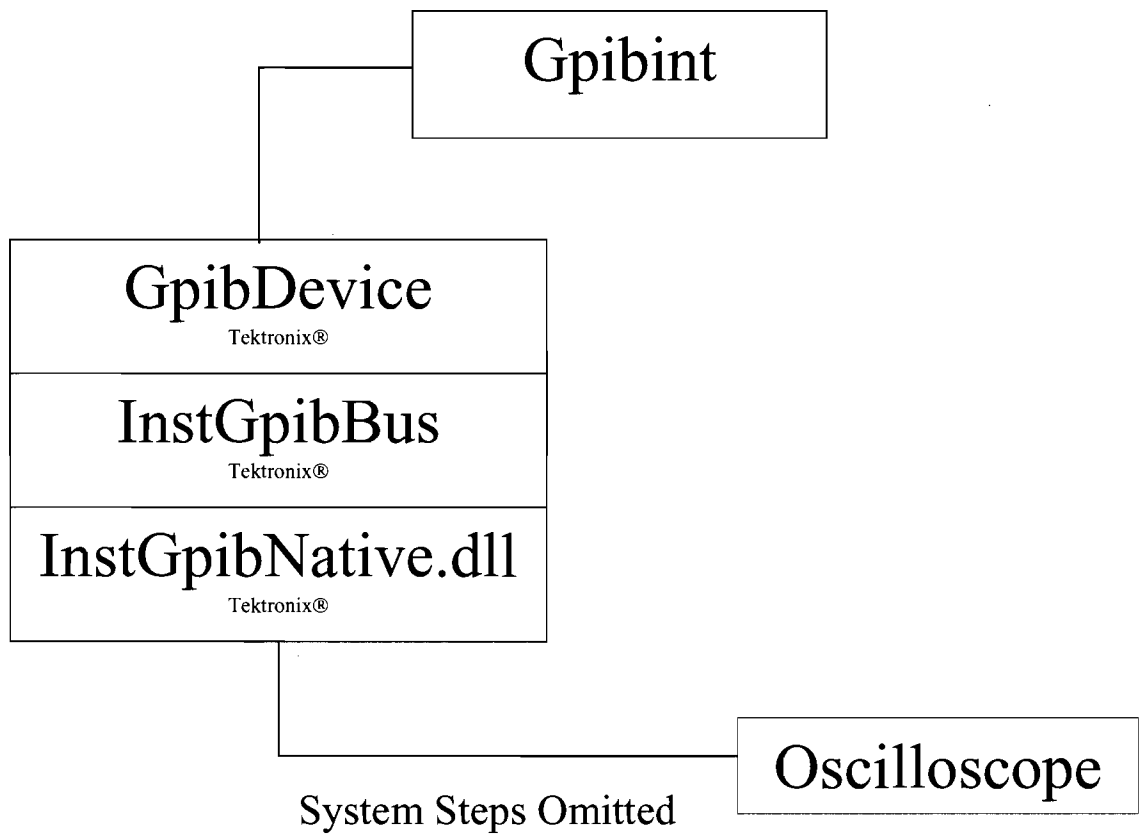
## **Conclusion**

By changing the layering structure of diagnostic software, such as ScopeControl, a single version of any diagnostic program can be made to run on either a control computer or on the newer computer-oscilloscope hybrids. ScopeControl was updated to exemplify the ability to make diagnostic software not only versatile but also reliable and user friendly. ScopeControl was only an example. The low level interface software developed in this project will be used by many applications running on the new generation of oscilloscopes. This will end the necessity of a separate computer to archive data collected by previous generations of oscilloscopes on OMEGA.

Figure 1

**ScopeControl internal interface structure**

As the diagram shows, the Gpibint layer uses methods defined in InstGpibBus.class to interface with InstGpibNative.dll which in turn communicates with the oscilloscope.



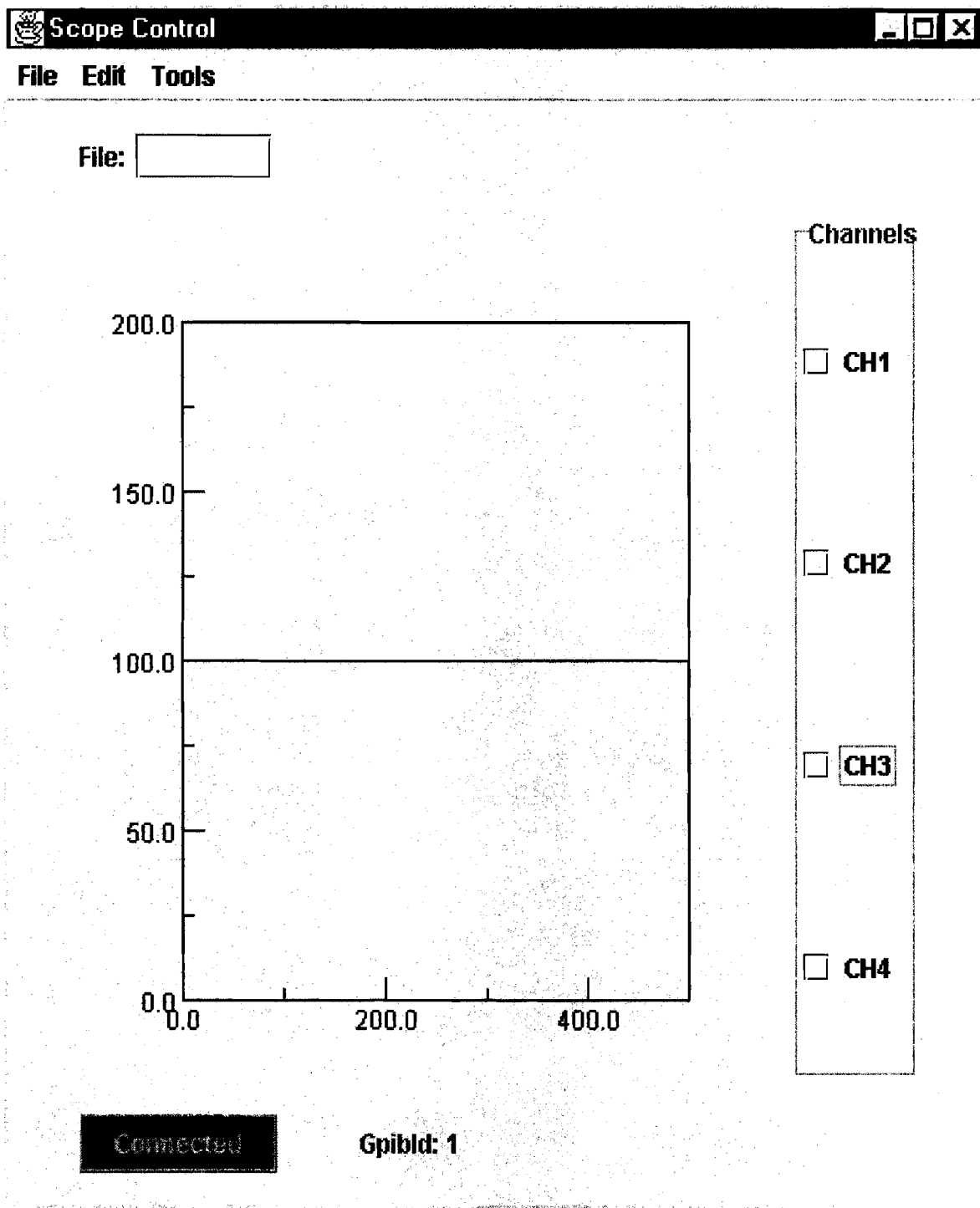


Figure 2.

ScopeControl

July 9<sup>th</sup>, 2001

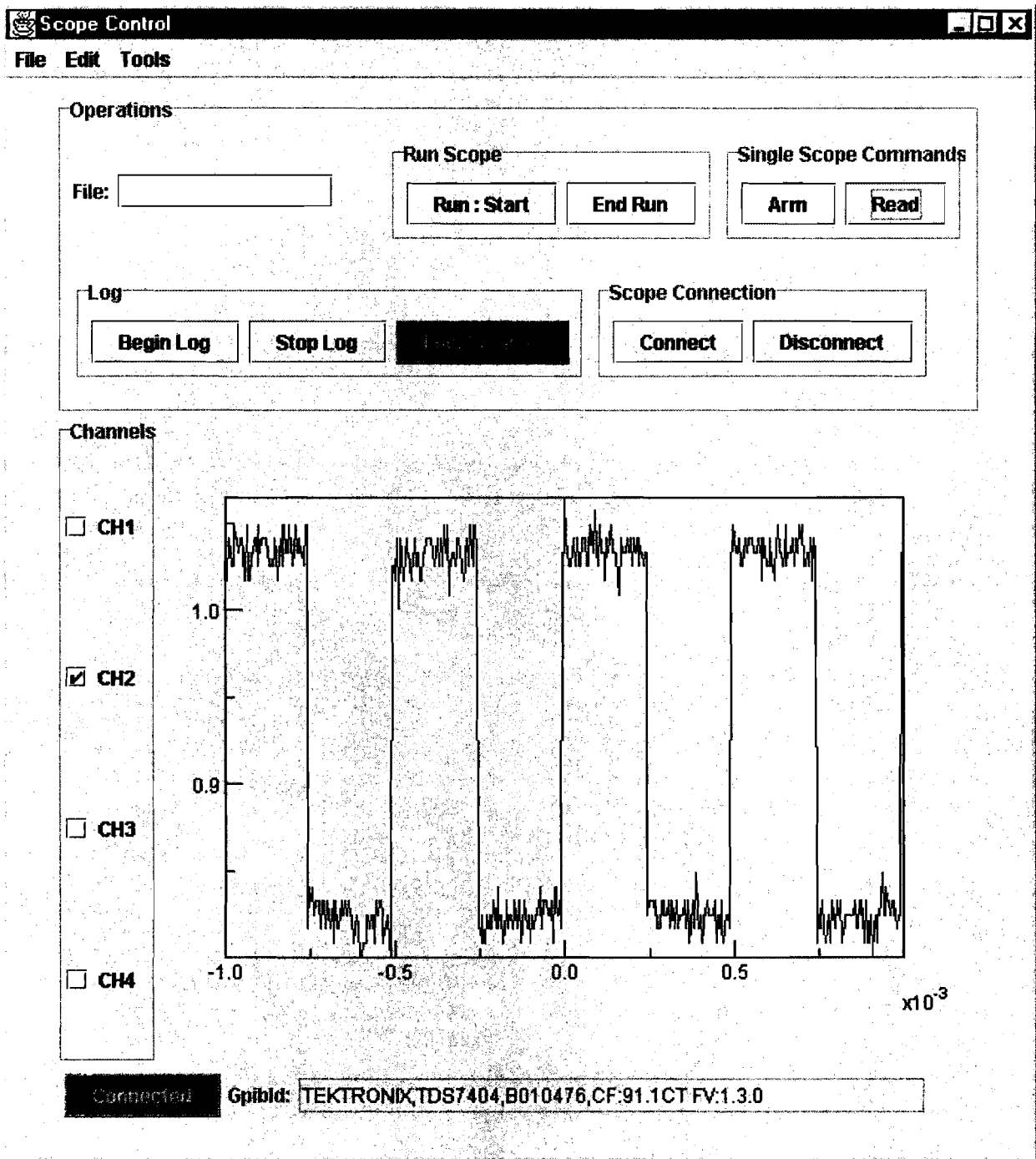


Figure 3.

ScopeControl

Modified by Dave Bowen  
as of August 31<sup>st</sup>, 2001

Appears with updated user interface and underlying error messaging improvements.

# Modeling Streak Camera Sweep Speeds

M. Fiedler

## LABORATORY FOR LASER ENERGETICS

University of Rochester  
250 East River Road  
Rochester, NY 14623-1299

### Abstract

On the OMEGA laser system at the University of Rochester's Laboratory for Laser Energetics (LLE), six P510 streak cameras measure the pulse shape of the 60 OMEGA beam lines. These cameras use a photocathode to convert an optical signal into an electron beam. A voltage ramp then sweeps this electron beam across a phosphor screen which is in turn imaged by a CCD. Currently, 120 images of an eight-pulse fiducial laser with a period of 548 ps are used to obtain approximately 700 measurements of the speed at which the electron beam sweeps across the image (sweep speed). A spline interpolation is then used to obtain sweep speed values at all points on the CCD. Unfortunately, this introduces noise, and fails when the sweep window changes due to unexpected variations in the camera's voltages. In order to deal with these issues, a model was constructed using frequencies obtained from a PSPICE simulation of the camera's sweep circuitry. This model will replace the spline interpolation, yielding a more accurate sweep and allowing data recovery in case of malfunction.

### Introduction

Streak cameras are instruments which convert optical signals into images where time is mapped to spatial displacement. They are extremely useful in measuring many types of short duration optical phenomena.<sup>1</sup> As a result, their uses are extremely varied. Their basic construction, however, is largely the same regardless of their use.

First, a photocathode is exposed to the optical signal to be measured, causing the photocathode to emit a beam of electrons (see fig. 1). The number of electrons emitted is proportional to the intensity of the input signal. This electron beam is then accelerated through a potential difference and focused between two plates which have a changing voltage across them. This changing voltage has the effect of changing the electron beam's deflection over time. Finally, at the end of the system, the electron beam impacts on a phosphor screen which fluoresces. The fluorescence is then imaged onto some medium.

The image created has two special characteristics. First, movement across the image represents a change in time, a reflection of the fact that the electron beam moved across the phosphor screen during the exposure. Second,

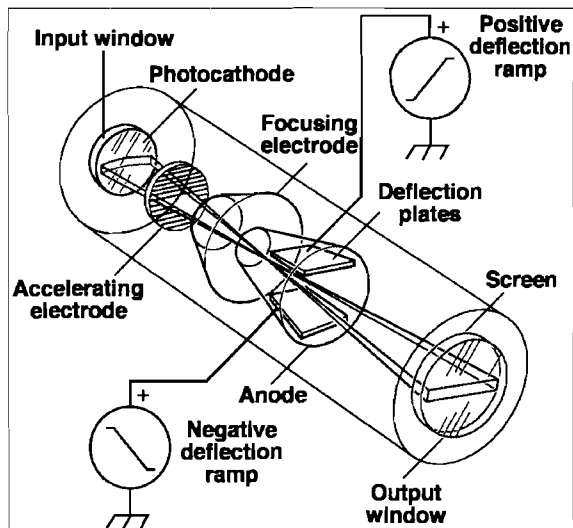


Figure 1

Streak tubes use changing voltages to sweep an electron beam across a phosphor screen over time.

the intensity of the image at a given location is proportional to the intensity of the input signal at the moment in time which corresponds to that image location. This happens because a stronger optical signal causes more electrons to be emitted by the photocathode and thus stronger fluorescence.<sup>1</sup>

Interpreting the image requires that the mapping between time and displacement (the image's time axis) be known. In addition, it is necessary to know the rate at which the electron beam is moving (the sweep speed) at all points in the image in order to normalize the image intensities (i.e. account for the fact that certain parts of the image were exposed for longer periods of time). On most cameras some sort of pulsed, fixed-period laser is used to approximate the time axis and sweep speed. The exact way in which this is done varies from camera to camera.<sup>1</sup>

This work was conducted at the University of Rochester's Laboratory for Laser Energetics (LLE). The lab's main focus is using the 60 beam OMEGA laser system for direct-drive inertial confinement fusion experiments. Such experiments involve hitting a deuterium-tritium target with lasers arrayed in a spherical configuration.<sup>2</sup> At LLE, six P510 streak cameras (all built at LLE) are used to measure the pulse shapes of each of the 60 OMEGA beam lines (ten beams in each camera) as shown in Fig. 3. This data can then be used for power balancing the OMEGA system (i.e. adjusting the laser system in order to improve irradiation uniformity). Better power balance improves the efficiency of inertial confinement fusion.<sup>3</sup> All work for this project was done using P510 cameras. Different types of streak cameras are also used a variety of other purposes at LLE; however, these cameras are not as well calibrated.<sup>4</sup>

Two pieces of software were used during this project. All analysis of P510 data was done using PV-WAVE, a language developed by Visual Numerics. Output from P510's can easily be loaded and manipulated in PV-WAVE using routines developed at LLE. In addition, PSPICE, developed by Cadence Design Systems, was used for circuit simulations.

### P510 Characteristics

Each P510 camera receives twelve fiber-optic feeds onto its photocathode and is capable of simultaneously collecting data on all twelve feeds (see fig. 2). Ten of these feeds are hooked up to OMEGA beam lines. The other two are connected to a fiducial timing laser. A CCD

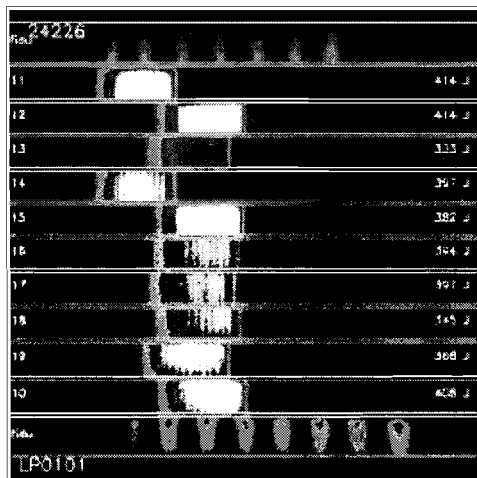


Figure 2  
P510's produce images with 12 different channels.

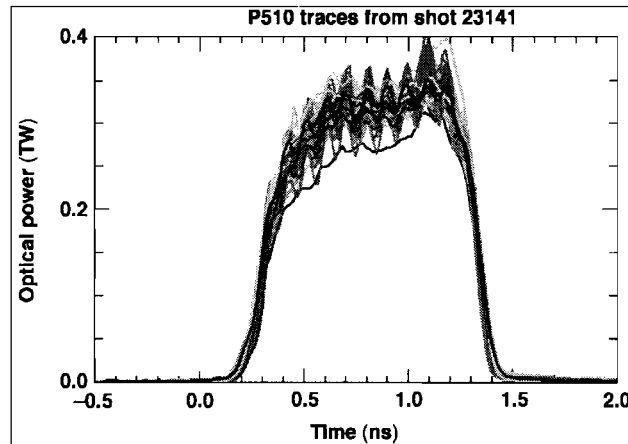


Figure 3  
Image intensity is used to produce measurements of the beam's optical power with respect to time. This graph shows measurements of the 60 OMEGA beam lines collected using all six P510 cameras.

configured to produce a 512 x 512 image serves as the output device.<sup>3</sup>

One problem with P510 streak cameras is that their voltages drift significantly on a weekly time scale. In order to make measurements at the desired level of a couple percent uncertainty, they must be calibrated weekly. Since the cameras were built at LLE, the calibration routines had to be developed at LLE. This calibration procedure is a three step process. First, geometric distortions resulting from imperfections in the camera's electron optics are corrected by projecting a regular pattern of rectangles through the camera and calculating the distortions in that regular pattern. These distortions can then be undone in the images the camera outputs. Next, the camera is flat fielded in order to compensate for variations in the relative sensitivity of the part of the system which maps to each pixel. This is done by exposing all parts of the system to a light source of uniform intensity for an identical amount of time. Finally, the sweep speed calibration is done, allowing calibration of the time axis and calculation of the electron beam's dwell time on each pixel.<sup>3</sup>

In order to do the sweep speed calibration, an eight-pulse fiducial laser is fed into all twelve channels of the streak camera. As result of the way it is configured, the fiducial has a period of 548 ps. In order to obtain data at as many locations as possible on the CCD, the camera's trigger settings are incremented in order to gradually move the fiducial train across the image. In total, approximately 120 images like those in Fig. 4 are taken with the fiducials at different locations in the image. These images are analyzed by calculating the number of pixels between each fiducial peak and then dividing by the time between peaks (the fiducial period of 548 ps). The resulting approximation of the derivative  $dx/dt$  is then assigned to the pixel midway between the peaks. From 120 images, this method yields 700 approximations of the sweep speed for each channel. Since any given calibration run does not calculate a value of  $dx/dt$  at every pixel across the CCD, a spline interpolation is used to calculate values at every pixel. The time axis can then be generated by integrating this data.<sup>3</sup>

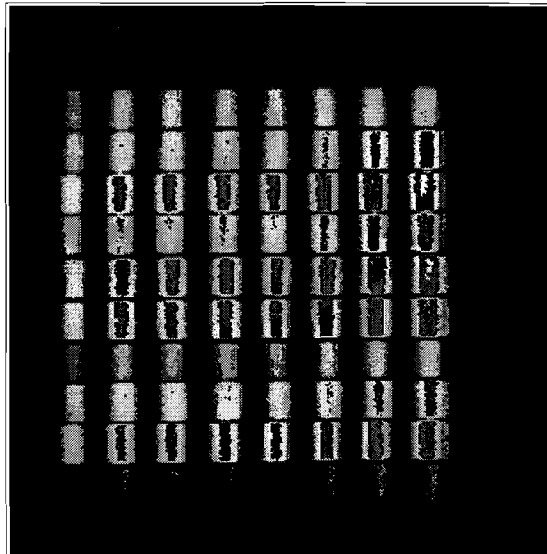


Figure 2

*Sweep speed calibration uses 120 images like these in order to calibrate each of the twelve channels.*

Unfortunately, this routine has some significant limitations. First, the method for obtaining the sweep speed approximation breaks down at the edges of the image. Once a fiducial pulse gets within 548 ps of the edge of the CCD, the pulse immediately preceding or following it (depending on which edge of the image is involved) does not show up in the image. The result is that sweep speed measurements cannot be obtained within 548 ps of the image's edge (approximately 50 pixels) since there is no second pulse to compare against. This causes the interpolation routine to fail near the edges since it cannot interpolate if no data is available for those portions of the sweep. Another significant limitation is that the data collected is applicable only over the narrow window where the camera is calibrated each week. Unfortunately, during OMEGA shots, the camera's voltages sometimes vary significantly from the set values. The result is a sweep speed different from the one measured during the calibration routine, thus decreasing the accuracy with which the camera's output can be interpreted (see fig. 5). In addition, the

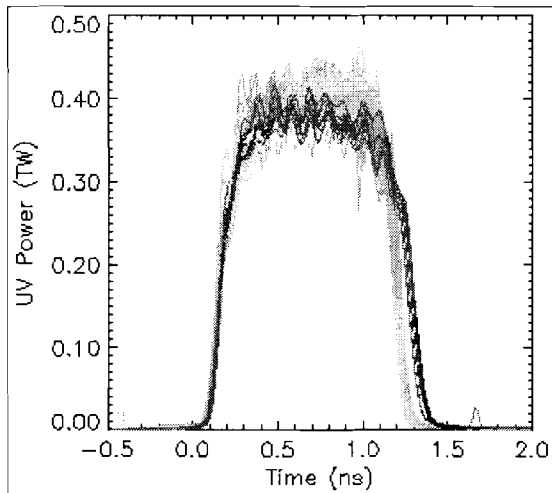


Figure 3

On this OMEGA system shot, one of the six P510 streak cameras malfunctioned and was operating outside of the window for which it was calibrated. As a result, the data obtained on ten of the beam lines have improperly calibrated time axes and do deviate significantly from the other beam lines.

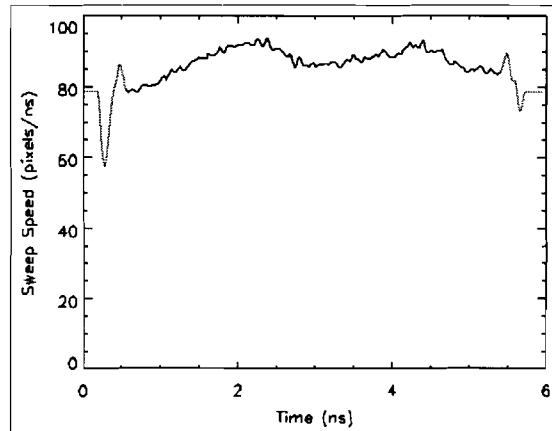


Figure 4

This image illustrates the problems inherent in the current sweep speed calibration routine. The portions .5 ns from the end oscillate wildly since no data is available for the interpolation. Also, high frequency noise is present along the entire sweep due to interpolation errors.

interpolation routine introduces high frequency noise into the data (see fig. 6).<sup>4</sup> The model created in this project will replace the spline interpolation, thus adding the ability to extrapolate beyond where data is collected and eliminating the noise problem.

The circuitry which generates the voltage ramp across the sweep plates was also developed at LLE. These sweep modules have a number of major features. The voltage pulse originates in a MOSFET/avalanche transistor stack which outputs a short pulse a few nanoseconds long. The pulse then goes through a double  $\pi$ -filter which filters out high frequency oscillations from the signal.<sup>5</sup> This filter will be referred to in this paper as the "main sweep filter". The pulse then goes through another  $\pi$ -filter which sets the module's main resonance frequency

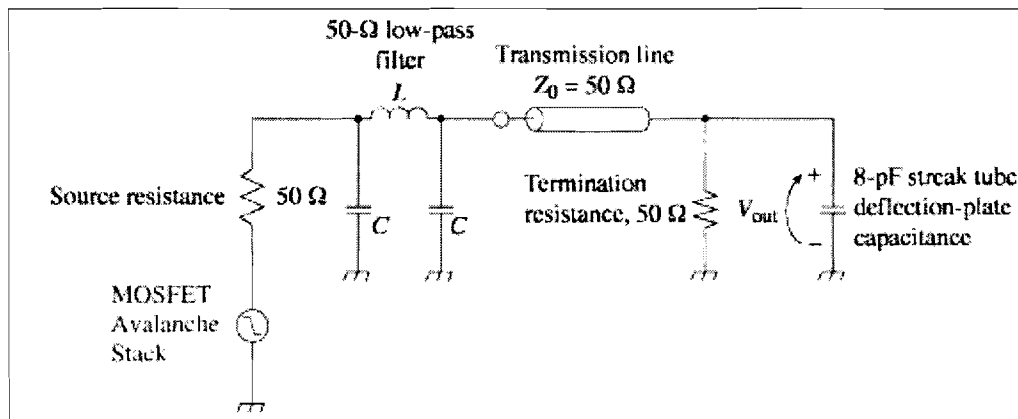


Figure 5

This is a simplified diagram of the circuitry which drives the sweep on P510 cameras. Please note that this simplifies the MOSFET and avalanche stacks, leaves out the  $\pi$ -filter, and does not note the parasitic components present in the circuit.

and thus the duration of the voltage ramp.<sup>5</sup> This filter will be referred to simply as the " $\pi$ -filter". Finally, the signal is then sent through a transmission line to the sweep plates (see fig. 7). In addition to the components actually installed in the system, the wires connecting these components have parasitic inductances and capacitances associated with them. All the units used in P510 cameras at LLE are constructed identically.<sup>5</sup> There are, however, variations between units, particularly in the transistor stacks which provide the initial pulse.<sup>4</sup> As a result, certain characteristics of one unit may be slightly different or absent entirely from another.

One of these units is attached to each sweep plate. Thus the magnitude of the total voltage change across the plates is roughly twice that from one unit. In typical operation, the units are set to produce a voltage ramp approximately 20 ns long; however, only approximately 6 ns of the voltage ramp actually maps onto the image (see fig. 8).

### Analyzing Voltage

In a P510 streak camera, the sweep speed is fundamentally related to the rate at which the voltage across the sweep plates changes. The mathematical relationship is as follows:

$$\frac{\partial V}{\partial t} = \frac{\partial V}{\partial x} \frac{\partial x}{\partial t} \quad (1)$$

This equation basically means that the derivative of the voltage ramp with respect to time is equal to the sweep speed multiplied by the volts per pixel value of the camera (the amount the voltage must be changed to yield a deflection of one pixel). The volts per pixel value was found to be roughly constant at all points on the CCD for each camera. Comparison of the derivative of measured voltage and sweep speed data confirmed the relationship between the two (see fig. 9). The basic shapes were comparable, thus confirming that the voltage and sweep speed are in fact closely related. Unfortunately, the measured voltage data was not accurate enough to serve as the basis for sweep speed calibration. As a result of the extremely high voltages involved and the short duration of the voltage ramp, measuring the fine structure of the voltage ramp was impossible. Thus, building a suitably accurate model of the sweep speed from measured voltage data was not a viable option. Instead, quantitative analysis of the circuit was done using a simulation.

The sweep circuitry was simulated using Cadence Design System's PSPICE software. Setting up the simulation required making certain simplifications in the circuit and adding

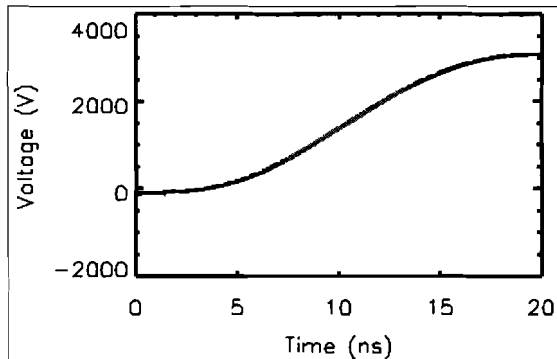


Figure 8

*On any given sweep, only a small portion of the voltage ramp is used. In this case the sweep window is represented by the flat portion from 7 to 13 ns.*

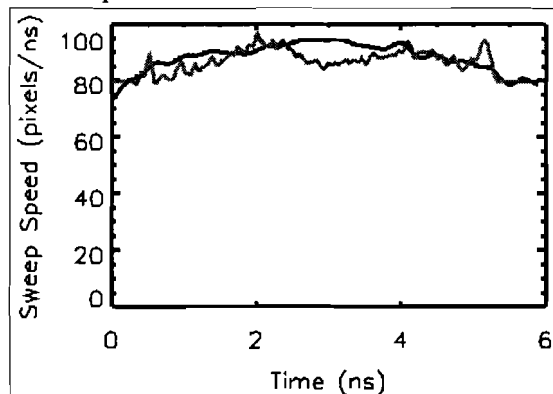


Figure 9

*The jagged line represents sweep speed and smoother one the derivative of measured voltage data. This graph shows that their overall shapes are similar.*

components not present in the actual circuit. First, the MOSFET and avalanche transistor stacks were approximated as piece-wise linear functions. This simplification captures the broad structure of the transistor stacks' output but may neglect certain finer structure. Moreover, considering that much of this fine structure varies from component to component, it could not be suitably modeled in the simulation. In addition, the circuit model included extra inductors and capacitors which compensated for the parasitic capacitive and inductive properties of the lengths of wire connecting the circuit's components.<sup>6</sup> The simulation's output was analyzed using tools built into the PSPICE software.

As a result of the inductive and capacitive elements in the circuit, the presence of certain resonant frequencies was assured. Three such frequencies were found by Fourier transforming the derivative of the voltage output. The part of the circuit creating that frequency was then found by measuring the oscillations across individual inductors and comparing that to the frequencies in the Fourier transform. The lowest frequency (38.62 MHz) was found to originate from the  $\pi$ -filter which sets the duration of the voltage ramp. This frequency had by far the highest amplitude, a logical outcome considering that this frequency is responsible for the broad structure of the entire voltage ramp. The second frequency (106.9 MHz) was linked to the main sweep filter. Finally, the third frequency (182.5 MHz) was found to be caused by the distributed parasitic inductive and capacitive components present in the circuit.

### Creating a Model

These frequencies provided the basis for a model of the sweep speed. The initial model used three sine terms, each of which had a fixed frequency and two free parameters (a phase and an amplitude). It looked as follows:

$$\frac{\partial x}{\partial t} = A_{\pi} \sin(\omega_{\pi} t + \phi_{\pi}) + A_M \sin(\omega_M t + \phi_M) + A_P \sin(\omega_P t + \phi_P) \quad (2)$$

The next step was to take this equation and fit it to sweep speed data. In order to ensure that the model would be useful over all possible sweep windows, it had to be fit over a time window longer than a single sweep. If this was not done, the model fit the peculiar structure of that particular sweep window and was inapplicable outside of it.

Creating this longer data set required some special work. First, five data sets of 30 images with varying trigger settings were taken from one of the P510's. While this data was somewhat less accurate than the usual 120 image calibration sets, it was sufficiently accurate for these purposes. Each of the five data sets represented a sweep speed generated from a different part of the voltage ramp. Once processed, this data was converted to a voltage (using equation 1) and compared to the measured output of the circuit. Although high-frequency structure is lacking in the measured voltage data, it still reflects the magnitude of the function at that point. As a result, one can use this relationship to correlate each sweep speed data set to a time interval on the voltage curve. This allows the relative temporal locations of the data sets to be determined. Once this is known, the five data sets can be combined into a single longer data set. Where sets overlapped, a weighted average was used giving greater weight to data points closer to the center of a data set.

Fitting the model to data was done in PV-WAVE with a non-linear regression routine which uses a modified Levenberg-Marquardt algorithm. The routine seeks to minimize the sum of the squares of the errors between the fit curve and the data, also called the error function. By evaluating the error function while varying the values of the parameters, the routine approximates the gradients of the error function in the parameter space. It uses these gradients to find the minimum of the error function, the location of best fit.<sup>7</sup>

Unfortunately, when this model was fit to data there were higher frequency elements that it could not explain (see fig. 10). While the model was able to explain the broad structure of the voltage ramp, two strong sinusoidal terms were still present in the residuals. This indicated that there were frequencies in the real circuitry that did not show up in the circuit simulations. The exact source of these oscillations is unknown; however, given the fact that the MOSFET/avalanche transistor stack was simplified in the circuit simulation, it is possible that it could produce certain frequencies which were not accounted for in the simulation. Moreover, since each camera uses two separate circuits to generate its sweep voltage, the frequencies may in fact emanate from two separate sweep drivers; however, determining the source of these residual frequencies with any certainty would require further investigation.

In order to create a workable model, two additional terms were added onto it. Each of these terms allowed the frequency to vary in addition to the amplitude and phase. The final model looked as follows:

$$\frac{\partial x}{\partial t} = A_{\pi} \sin(\omega_{\pi} t + \phi_{\pi}) + A_M \sin(\omega_M t + \phi_M) + A_P \sin(\omega_P t + \phi_P) + A_1 \sin(\omega_1 t + \phi_1) + A_2 \sin(\omega_2 t + \phi_2) \quad (3)$$

This refined model led to a much better fit of the long data set (see fig. 11).

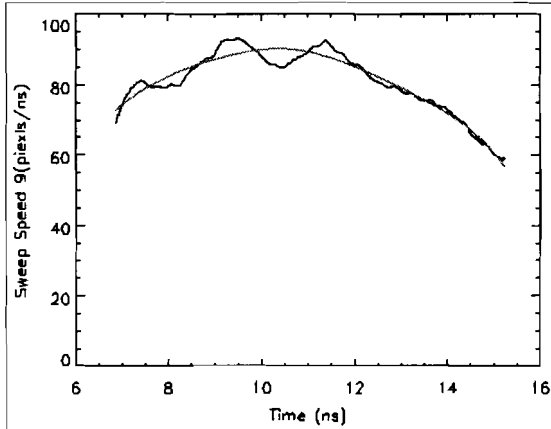


Figure 10

The smooth curve represents the three-term model while the oscillating curve represents the data. The three-term model fails to account for higher frequency structure in the real data.

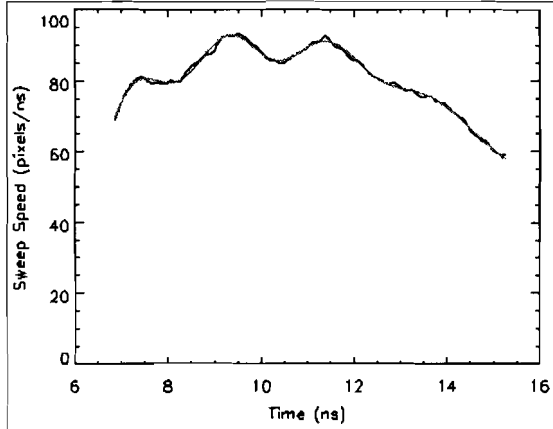


Figure 11

The smooth curve represents the five-term model and the more jagged curve represents the data. Using five-term produces a close correspondence to the measured sweep speed.

Once the model had been created, the uncertainties in each of the parameters were calculated. This was done using the following relationship:

$$\text{uncertainty in } a = \epsilon_a = \Delta a$$

$$\text{where } \chi^2(a + \Delta a) = \chi^2(a) + 1 \text{ and } \chi^2 = \sum \frac{(f(a) - y_i)^2}{\delta_i^2} \quad (4)$$

By varying each parameter from its optimized position one at a time, values of the curve fit's chi-squared function were calculated around its minimum. An interpolation was then used to find where the chi-squared had increased by one from its value when the function was optimized. This change in the parameter was equal the standard deviation of that parameter. This process was repeated for each of the function's parameters.<sup>8,9</sup>

<b>Parameter</b>	$A_\pi$	$\phi_\pi$	$A_M$	$\phi_M$	$A_P$	$\phi_P$
<b>Value</b>	98.7 px/ns	-1.12 rad	13.8 px/ns	3.33 rad	3.24 px/ns	-5.83 rad
<b>Uncertainty (%)</b>	$\pm 0.03$	$\pm 0.04$	$\pm 0.24$	$\pm 0.07$	$\pm 0.99$	$\pm 0.17$
<b>Parameter</b>	$A_1$	$\omega_1$	$\phi_1$	$A_2$	$\omega_2$	$\phi_2$
<b>Value</b>	1.18 px/ns	505 MHz	-1.95 rad	3.43 px/ns	447 MHz	.106 rad
<b>Uncertainty (%)</b>	$\pm 1.75$	$\pm 0.05$	$\pm 0.93$	$\pm 0.92$	$\pm 0.03$	$\pm 9.01$

The final step was to move to a shorter, single-sweep time window while maintaining the shape of the fit over the longer window. Doing this required that the term's phases and amplitudes be fixed relative to each other and that the two fit frequencies be fixed. The only parameters allowed to vary were the amplitude and phase of the  $\pi$ -filter term. All other phases were defined as a function of the  $\pi$ -filter phase in order to keep the terms in relative phase with each other no matter which time window was being examined. The other phases were defined as follows:

$$\phi_n' = \frac{\omega_n}{\omega_\pi} (\phi_\pi' - \phi_\pi) + \phi_n \quad (5)$$

Likewise, the ratios of the amplitudes were fixed. This allows the fit to adjust in instances where the voltage curve is simply dilated, the result of a change in the voltage applied to sweep circuitry. The relationship used here is shown below.

$$A_n' = A_\pi' \frac{A_n}{A_\pi} \quad (6)$$

This two-parameter curve fit weekly 120 image calibration data well (see fig. 12); however, now that the fit had been reduced to two parameters, it was not necessary to have the hundreds of data points which 120 images could provide. On each OMEGA system shot, there are eight fiducial pulses present on the top and bottom of the camera's output. Each set of eight pulses can be used to generate seven approximations of the sweep speed. When the sweep speed was fit to just one set of these fiducials (seven data points), the fit was nearly identical to that obtained from a 120 image, 700 data point data set (see fig. 13). Simply, this means that the

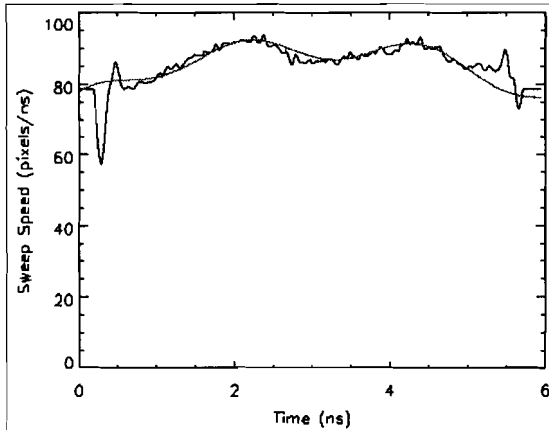


Figure 12

The model is represented by the smooth line and the measured sweep speed by the jagged line. The two-parameter model fits weekly, 120 image data well.

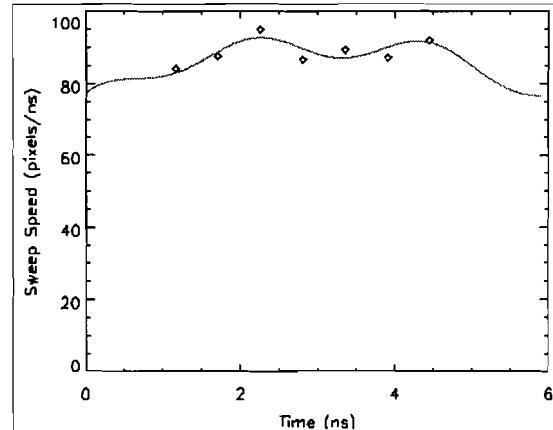


Figure 13

The model is represented by the line and the measured sweep data by the data points. The fit using a single image is very similar to the fit at left which uses 120 images.

sweep speed can be re-calibrated using the fiducial data in the event of malfunction.

### **Conclusion**

Analysis of a streak camera's voltage module provides a suitable basis for a model of its sweep speed. This model will be useful in both better calibrating streak cameras on a weekly basis by avoiding the limitations of an interpolation routine and in recovering data in the event the cameras malfunction. Moreover, this work should be useful beyond the realm of P510 streak cameras. All streak cameras at LLE have fiducial lasers present; however, most cameras do not have weekly calibration procedures like the P510's and simply use the eight fiducial pulses to approximate the sweep speed at seven points during each shot. If a sweep speed model were constructed based on those cameras' circuitry, their calibrations and thus the accuracy of their output could be greatly enhanced.

### **Acknowledgments**

I would like to thank Dr. Stephen Craxton, director of the Summer High School Research Program at LLE for giving me the opportunity to work at LLE during the summer of 2001. I would also like to thank Mr. Robert Boni for his help in collecting data from the P510's, Mr. Wade Bittle for creating the circuit model used in this project, and Dr. James Knauer for help regarding error analysis. Finally, I would like to thank my advisor, Dr. William Donaldson for all the time and help he gave me. There is no question that this project would have been impossible without him.

### **References**

1. R. A. Lerche, D. S. Montgomery and J. D. Wiedwald, "High Contrast Ratio Power Measurements with a Streak Camera" SPIE 1539 68 (1991).
2. T. R. Boehly, R. S. Craxton, T. H. Hinterman, P. A. Jaanimagi, J. H. Kelly, T. J. Kessler, R. L. Kremens, S. A. Kumpan, S. A. Letzring, R. L. McCrory, S. F. B. Morse, W. Seka, S. Skupsky, J. M. Sources, and C. P. Verdon, "The upgrade to the OMEGA laser system," *Fusion Technol.* **26**, 722-729 (1994).
3. W. R. Donaldson, R. Boni, R. L. Keck, and P. A. Jaanimagi, "Self-Calibrating, Multichannel, Streak Cameras for Inertial Confinement Fusion Applications," to be published in *Review of Scientific Instruments*.
4. W. R. Donaldson (private communication).
5. "Design and Performance of a Selectable-Rate Streak-Camera Deflection Ramp Generator," *Laboratory for Laser Energetics LLE Review* **85**, 21-28.
6. W. Bittle (private communication).
7. PV-WAVE Advantage Reference. (Visual Numerics, Houston, 1993), p. 485-494.
8. P. R. Bevington, Data Reduction and Error Analysis for the Physical Sciences. (McGraw-Hill, New York, 1969), p. 242-243.

9. J. Knauer (private communication).

# **Two-Dimensional Phase Unwrapping for the Design of Distributed Phase Plates**

Melisa Gao

*Laboratory for Laser Energetics, University of Rochester  
Rochester, New York 14623-1299*

## **1. ABSTRACT**

When the surface of a distributed phase plate (DPP) is designed via the phase retrieval method, the resulting phase profile is discontinuous because of the use of the inverse tangent function. The precise manufacturing of a discontinuous phase plate is impossible, however, and any imperfections scatter the laser beam out of the desired far-field intensity pattern. Phase unwrapping is therefore employed to create a continuous phase plate by removing discontinuities between adjacent data points.

An unwrapping algorithm that attempts to smooth over the data while retaining the desired far-field mapping was successfully implemented and will be integrated into the phase retrieval method for future calculations of DPPs. The weighted form of the algorithm is expected to increase its effectiveness at unwrapping uncertain data.

## 2. INTRODUCTION

A diffraction-limited focal spot is governed by the focal length ( $f$ ), wavelength ( $\lambda$ ), and diameter of the laser beam ( $D$ ). On the University of Rochester Laboratory for Laser Energetics OMEGA laser system, this yields a focal spot approximately  $2\ \mu\text{m}$  in diameter,

$$\frac{f\lambda}{D} = \frac{1.8\text{m}(351\text{nm})}{28\text{cm}} = 2\ \mu\text{m}, \quad (1)$$

as opposed to the 1-mm target size. This desired focal spot size could be achieved by simply defocusing the laser (i.e. placing the target in front of the focal plane of the lens), but the intensity profile would not be flat enough and is uncontrollable.

To avoid these problems, a distributed phase plate (DPP) is used. A DPP is a plate of glass with an uneven surface profile that adds phase to the rays in the near field, thereby manipulating the far-field image (Fig. 1). These phase changes effectively spread the energy out across the entire target in the far field and define a well-controlled average intensity pattern.

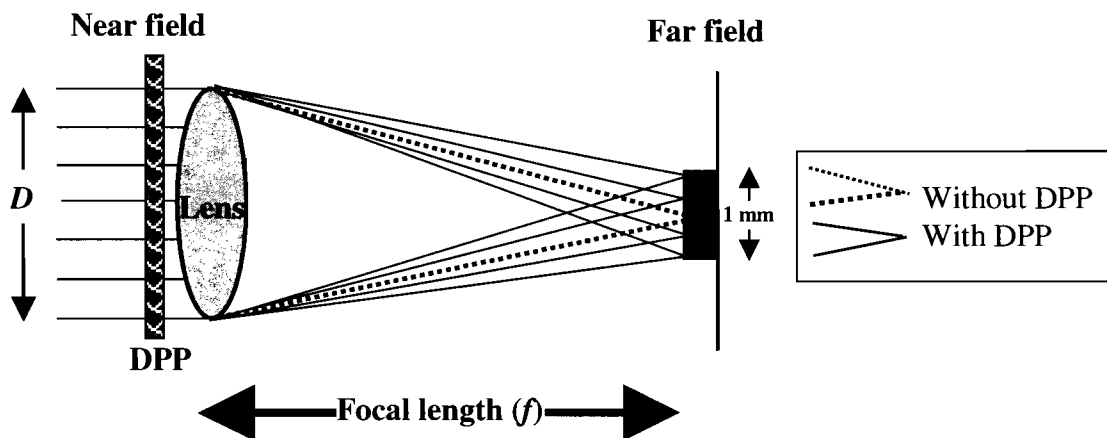


Fig. 1. A DPP spreads the beam across the 1-mm target by adding phase to the incident rays.

The far-field intensity pattern generated by a DPP is actually composed of a finely-grained structure called a speckle, with an average diameter given by Eq. (1). This speckle pattern is smoothed out in a time-integrated sense using smoothing by spectral dispersion (SSD), which randomly changes the speckle pattern on a small time-scale.

A distributed phase plate can be designed to produce almost any desired far-field average intensity pattern. The calculation of a DPP is based on the concept that the complex-valued near and far fields are related through Fourier transforms<sup>1</sup> (Fig. 2). The Fourier transform of the near field, which is a function of the phase and amplitude (defined as the square root of the intensity) of the laser beam as it enters the lens, is proportional to the phase and amplitude of the far field. The inverse Fourier transform of the far field is the near field. Fourier transforms are a one-to-one process, so if the near field is known, the far field can be uniquely determined, and vice versa.

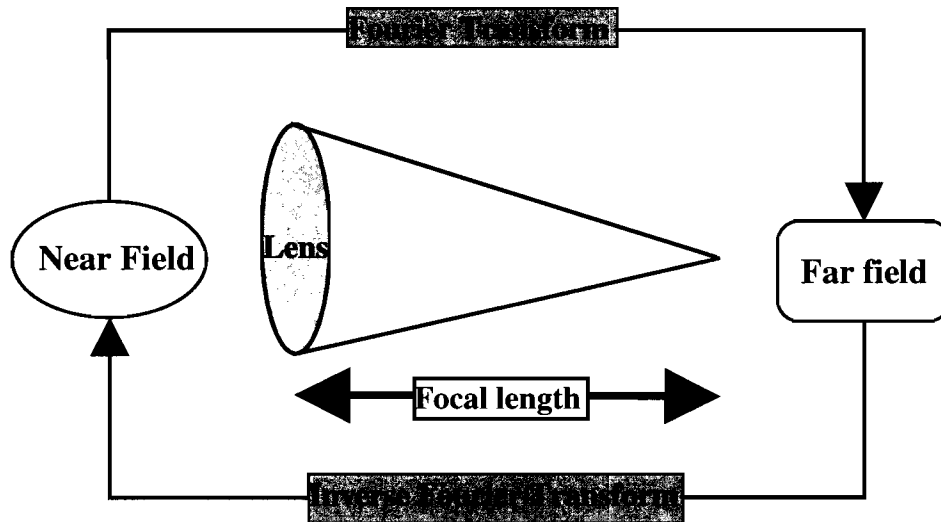


Fig. 2. The far field is the Fourier transform of the near field, which is the inverse Fourier transform of the far field.

### 3. THE PHASE RETRIEVAL METHOD

The phase retrieval method (Fig. 3) designs the surface of a DPP that will generate a desired far-field intensity pattern<sup>2</sup>. Initially, the intensity pattern of the near field,  $I_{NF}$ , is given (as a property of the laser beam itself), and the desired far-field intensity pattern  $I_{FF}$  is chosen. For the first step of the phase retrieval method, the phase profile of the near field is initialized to a guess,  $P_0$ . The Fourier transform of this initial near field ( $I_{NF}$  and  $P_0$ ) is the far field, where the calculated far-field intensity pattern is replaced by  $I_{FF}$ . The inverse Fourier transform of the new far field (the calculated phase profile  $P_1$  and known intensity pattern  $I_{NF}$ ) is the calculated near field for the next iteration of the sequence.

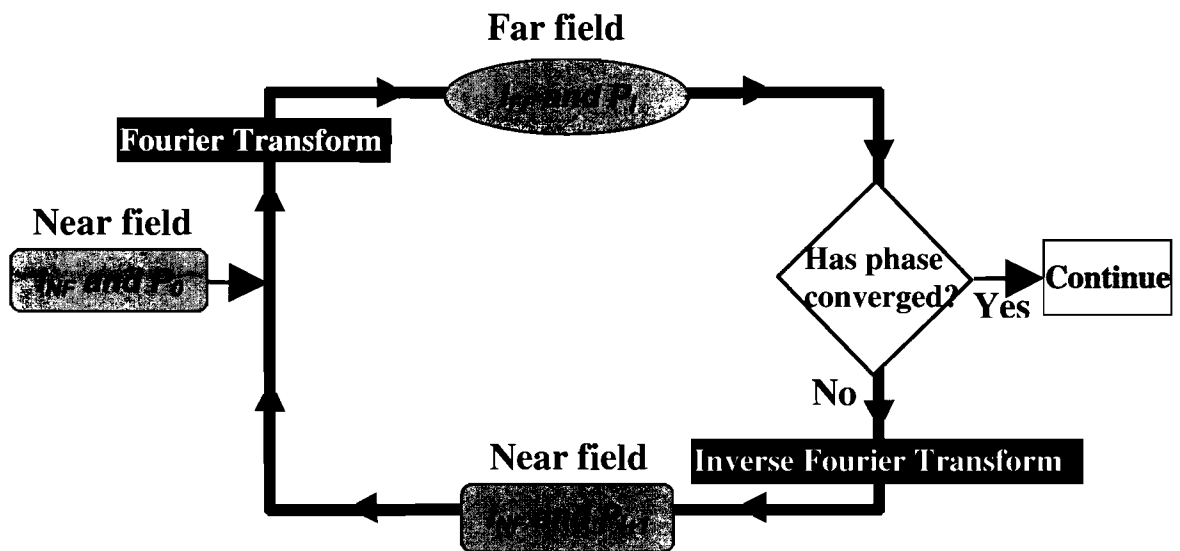


Fig. 3. The phase retrieval method is an iterative sequence used to design a DPP that will calculate a desired far-field intensity pattern.

In the near field, the calculated phase  $P_2$  is retained while the resultant intensity is discarded and replaced with the known  $I_{NF}$ . This new near field ( $P_2$  and  $I_{NF}$ ) is Fourier-transformed to calculate the new far field, and the process repeats.

Each time, the calculated phase profile  $P_i$  is retained while the calculated intensity

pattern is replaced by  $I_{NF}$  or  $I_{FF}$ . After multiple iterations, the intensity and phase profiles in the near and far field eventually converge upon a solution ( $P_i \cong P_{i+1}$ ). At this point, a near-field phase profile has been calculated that, with the specific laser beam intensity, will generate the desired far-field intensity pattern. Since a DPP serves to add phase to a uniform beam, the appropriate DPP is simply this calculated near-field phase profile.

A problem arises, however, in the actual implementation of the calculated DPP phase profile. Note that the inverse tangent function is needed to calculate the phase from the complex value obtained from the Fourier transform. Sharp  $2\pi$  discontinuities in the calculated phase arise, since a single branch of the inverse tangent function is restricted to the interval of  $[-\pi, \pi)$ . Because of manufacturing limitations, attempting to create this discontinuous DPP will result in inaccuracies in the plate. These imperfections lead to the scatter of light in the far field, which decreases the efficiency of the distributed phase plate.

Thus after the phases converge to signal the conclusion of the phase retrieval method, the calculated phase profile is unwrapped (Fig. 4) via the cosine transform

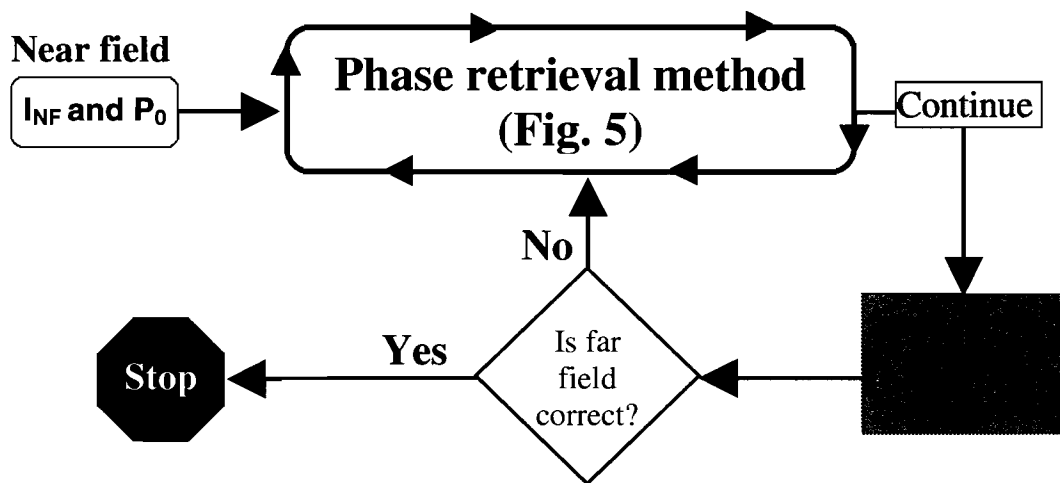


Fig. 4. Multiple iterations of the phase retrieval method and unwrapping process are performed as needed to generate the desired far-field intensity pattern.

technique to remove discontinuities. Phase data has ambiguities of  $2\pi$ , so phase unwrapping is employed to construct a smooth function that attempts to retain the phase data of a wrapped function with discontinuities of  $2\pi$ . That is, the values of the unwrapped function are ideally equal to the values of the wrapped function plus integral multiples of  $2\pi$ , so the far-field image remains unaffected.

Because the unwrapping algorithm must smooth over noise in the data, however, it can cause loss of data that changes the far field image. The unwrapped phase profile is therefore checked for accuracy (i.e. whether it produces the desired far field). If necessary, the method is repeated until a smooth, unwrapped distributed phase plate has been calculated.

#### 4. UNWRAPPING

Unwrapping is the reconstruction of a smooth function given its values on the interval of  $[-\pi, \pi)$ . The wrapped version of a continuous one-dimensional function is easily unwrapped by detecting discontinuities and adding or subtracting  $2\pi$  over selected intervals as necessary. In Fig. 5a, for example, the discontinuity at  $x=0.25$  can be eliminated by shifting up by  $2\pi$  the section of the function to the right of it. By examining all the discontinuities in the function in this fashion, a smooth curve is reconstructed. Note that this unwrapped result is not unique; the entire function can be shifted by any constant phase factor.

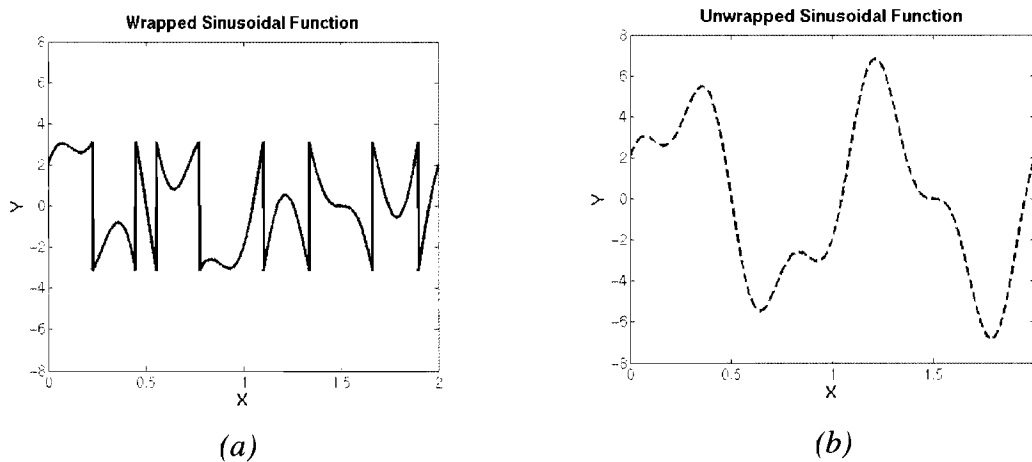


Fig. 5. A smooth, one-dimensional function of the sum of sines and cosines is reconstructed by shifting discontinuous regions in the wrapped function by multiples of  $2\pi$ .

Unwrapping a two-dimensional function is not as straightforward, however, as shifting values by  $\pm 2\pi$  in one dimension might result in discontinuities in the other direction. A single pixel of noise would become a spike in the unwrapped function, and since this happens independently in each direction, it may be impossible to generate a smooth function.

## 5. THE COSINE TRANSFORM TECHNIQUE FOR PHASE UNWRAPPING

The cosine transform technique is a method of finding a least-squares solution for the unwrapped function<sup>3</sup>. Let  $\phi$  and  $\psi$  be the unwrapped and wrapped functions, respectively, both on an  $M$  by  $N$  grid. Note that the wrapped and unwrapped functions have similar derivatives, where derivatives are estimated as the difference between neighboring points. These values will henceforth be referred to as the *finite difference* at a point. In addition to providing a straightforward method of approximating a derivative, this allows us to quantify the derivative at every point, including discontinuities.

In continuous regions in the wrapped function, the finite differences of the wrapped and unwrapped functions are equal. At discontinuities of  $2\pi$  in the wrapped function, the finite differences are unequal but differ only by  $\pm 2\pi$ . Note that while all finite differences in the (continuous) unwrapped function will be relatively small, those at discontinuities of the wrapped function will be much larger values.

For example, suppose we have the adjacent data values 3.140 and 3.240 on the unwrapped function, with an estimated difference of  $3.240 - 3.140 = 0.100$ . On the wrapped function, the first data point is unchanged while the second becomes  $3.240 - 2\pi = -3.043$ . The estimated difference for the wrapped function is therefore  $-3.043 - 3.140 = -6.183$ . Thus the two estimated differences are off, but only by an integral number of  $2\pi$ . Specifically, if we define the function *Wrap* to return a value on the interval  $[-\pi, \pi)$  by adding integral multiples of  $2\pi$ , then  $0.100 = \text{Wrap}(-6.183)$ . Moreover, the *Wrap* relationship holds true throughout continuous regions as well, since finite differences are equal (as established above).

Generalizing this concept, we see that for an ideal solution for  $\phi$ ,

$$\begin{aligned}\phi_{i+1,j} - \phi_{i,j} &= \text{Wrap}(\psi_{i+1,j} - \psi_{i,j}) \\ \phi_{i,j+1} - \phi_{i,j} &= \text{Wrap}(\psi_{i,j+1} - \psi_{i,j}),\end{aligned}\quad (2)$$

where  $0 \leq i \leq M-1$  and  $0 \leq j \leq N-1$ . That is, the finite differences of the wrapped function equal the wrapped version of the finite differences of the unwrapped function.

By extension, the best solution for  $\phi$  is that which satisfies Eq. (2) by minimizing the sum

$$\sum_{i=0}^{M-2} \sum_{j=0}^{N-1} \left[ (\phi_{i+1,j} - \phi_{i,j}) - \text{Wrap}(\psi_{i+1,j} - \psi_{i,j}) \right]^2 + \sum_{i=0}^{M-1} \sum_{j=0}^{N-2} \left[ (\phi_{i,j+1} - \phi_{i,j}) - \text{Wrap}(\psi_{i,j+1} - \psi_{i,j}) \right]^2 \quad (3)$$

This least-squares solution allows for smoothing over of noise pixels to create the best overall fit.

According to Hunt's matrix formulation<sup>4</sup>, Eq. (3) can be simplified to

$$\phi_{i+1,j} + \phi_{i-1,j} + \phi_{i,j+1} + \phi_{i,j-1} - 4\phi_{i,j} = \rho_{i,j}, \quad (4)$$

where

$$\rho_{i,j} = \text{Wrap}(\psi_{i+1,j} - \psi_{i,j}) - \text{Wrap}(\psi_{i,j} - \psi_{i-1,j}) + \text{Wrap}(\psi_{i,j+1} - \psi_{i,j}) - \text{Wrap}(\psi_{i,j} - \psi_{i,j-1}).$$

Through simple algebraic manipulation, Eq. (4) becomes

$$\begin{aligned}\rho_{i,j} &= \left[ (\phi_{i+1,j} - \phi_{i,j}) - (\phi_{i,j} - \phi_{i-1,j}) \right] + \left[ (\phi_{i,j+1} - \phi_{i,j}) - (\phi_{i,j} - \phi_{i,j-1}) \right] \\ &= (\phi_{i-1,j} - 2\phi_{i,j} + \phi_{i+1,j}) + (\phi_{i,j-1} - 2\phi_{i,j} + \phi_{i,j+1}),\end{aligned}\quad (5)$$

which is the discrete version of Poisson's equation,

$$\rho(x, y) = \frac{\partial^2}{\partial x^2} \phi(x, y) + \frac{\partial^2}{\partial y^2} \phi(x, y). \quad (6)$$

We now use the form of the forward and inverse discrete cosine transform<sup>5</sup> (DCT) below to solve Eq. (5) for  $\phi_{i,j}$ :

$$\begin{aligned}
\text{Forward : } C_{i,j} &= \sum_{i=0}^{M-1} \sum_{j=0}^{N-1} 4x_{i,j} \cos \left[ \frac{\pi}{2M} m(2i+1) \right] \cos \left[ \frac{\pi}{2N} n(2j+1) \right] \\
\text{Inverse : } x_{i,j} &= \frac{1}{MN} \sum_{i=0}^{M-1} \sum_{j=0}^{N-1} w_1(m)w_2(n)C_{i,j} \cos \left[ \frac{\pi}{2M} m(2i+1) \right] \cos \left[ \frac{\pi}{2N} n(2j+1) \right],
\end{aligned} \tag{7}$$

where

$$\begin{aligned}
w_1(m) &= 1/2, & m = 0, \\
w_1(m) &= 1, & 1 \leq m \leq M-1 \\
w_2(n) &= 1/2, & n = 0, \\
w_2(n) &= 1, & 1 \leq n \leq N-1.
\end{aligned}$$

The discrete cosine transforms of  $\phi_{i,j}$  and  $\rho_{i,j}$  ( $\hat{\phi}_{i,j}$  and  $\hat{\rho}_{m,n}$ , respectively) according to the form in Eq. (7) are substituted into Eq. (5). Solving for  $\hat{\phi}_{i,j}$  in terms of the known values  $\hat{\rho}_{m,n}$ , we obtain

$$\hat{\phi}_{i,j} = \frac{\hat{\rho}_{m,n}}{2 \left[ \cos \left( \frac{\pi m}{M} \right) + \cos \left( \frac{\pi n}{N} \right) - 2 \right]}. \tag{8}$$

The inverse DCT of  $\hat{\phi}_{i,j}$  yields the unwrapped phase  $\phi_{i,j}$ .

Thus the cosine transform technique for phase unwrapping involves three steps: finding the values of  $\hat{\rho}_{m,n}$  by performing the forward DCT on the known array  $\rho_{i,j}$ , substituting into Eq. (5) to find  $\hat{\phi}_{i,j}$ , and taking the inverse DCT of  $\hat{\phi}_{i,j}$  to calculate the values of  $\phi_{i,j}$ .

## 6. RESULTS

To test the algorithm's effectiveness, the wrapped version of a smooth DPP was unwrapped using the cosine transform technique (Fig. 6). In the reconstructed phase profile, discontinuities of  $2\pi$  were successfully removed and noise spikes eliminated, resulting in a smooth function that retains the phase data of the original DPP.

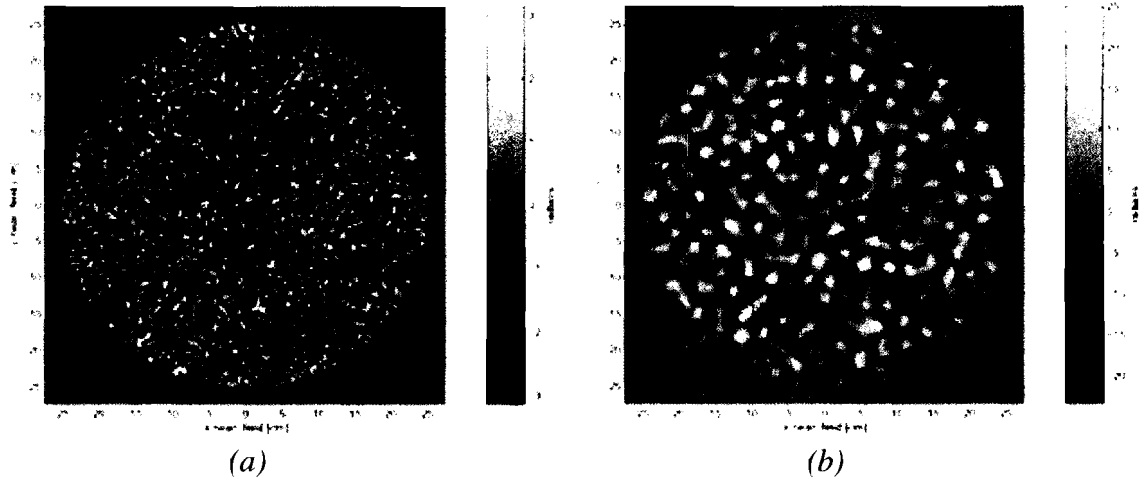


Fig. 6. The phase profile of a wrapped DPP (a) is unwrapped to recover the phase of a smooth DPP (b) using the cosine transform technique.

This algorithm fails to account for uncertainty in data, however, such as at the border of the DPP. It tries to eliminate the discontinuity between the edge of the DPP and the area of no data. Though this does not present a problem in this particular phase plate, as the errors occur only beyond the data boundary of the DPP, it may affect the plate in other instances. Implementing the weighted Picard algorithm<sup>6</sup> that factors in assigned confidence levels is expected to minimize this problem. Assigning a confidence of zero to areas of no data, for example, would prevent the rest of the data from being corrupted as the algorithm tries to reconcile the discontinuities.

## **7. CONCLUSION**

The cosine transform technique was successful in returning a distributed phase plate with a continuous surface profile that generates the desired far-field intensity pattern on target. The algorithm will be integrated into the phase retrieval method for future calculations of DPPs. The smooth DPP surface profiles generated will be more efficient, with minimal scatter of light.

Any problems encountered with uncertainty in data or noise pixels are expected to be corrected by assigning a weight to each data point via the Picard method. This will result in an even more effective DPP, thereby improving the accuracy of the far field intensity mapping as compared to the desired pattern.

## **8. ACKNOWLEDGEMENTS**

Special thanks first and foremost to my advisor, Dr. John A. Marozas, whose guidance throughout the summer and beyond was indispensable and without whom none of this would have been possible. I am grateful to Dr. R. S. Craxton, who invited me to be a part of this experience, and the other summer high school students, who were always there to provide either a fresh perspective on my research project or a much-needed break from it. Finally, to Dr. R. Epstein and the many others at LLE whom I was fortunate enough to get to know: your approachability and companionship made this opportunity an unforgettable one. Thank you.

## 9. REFERENCES

1. R. N. Bracewell, *The Fourier Transform and Its Applications*, 2<sup>nd</sup> ed., rev., McGraw-Hill Series in Electrical Engineering. Circuits and Systems (McGraw-Hill, New York, 1986).
2. J. R. Fienup, "Phase retrieval algorithms: a comparison," *Appl. Opt.* **21** (15), 2758-2769 (1982).
3. D. C. Ghiglia and L. A. Romero, "Robust two-dimensional weighted and unweighted phase unwrapping that uses fast transforms and iterative methods," *J. Opt. Soc. Am. A* **11**, 107-117 (1994).
4. B. R. Hunt, "Matrix formulation of the reconstruction of phase values from phase differences," *J. Opt. Soc. Am.* **69**, 393-99 (1979).
5. W. H. Press, B. P. Flannery, S. A. Teukolsky, and W. T. Vetterling, *Numerical Recipes: The Art of Scientific Computing* (Cambridge U. Press, Cambridge, 1986).
6. D. C. Ghiglia and M. D. Pritt, *Two-dimensional phase unwrapping: theory, algorithms, and software* (John Wiley and Sons, New York, 1998).

# Optical Characterization of GaAs with MSM Structures

Brian Ha  
Gates Chili High School

Advised by Dr. Roman Sobolewski

University of Rochester  
Laboratory for Laser Energetics  
2001 Summer High School Research Program

## 1. Abstract

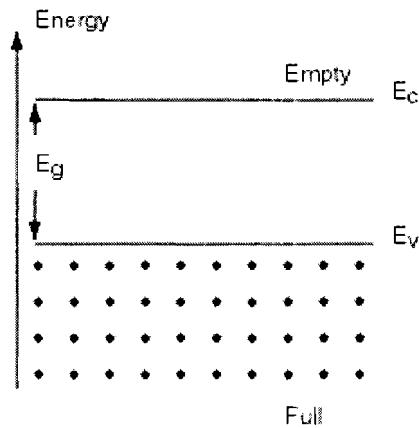
There is a great demand for the ultrafast testing of high-speed electronic/optoelectronic devices in various fields of science and engineering. Such testing can be achieved by electro-optic (EO) sampling systems that are capable of sampling picosecond voltage signals with subpicosecond time resolution. Samples of gallium arsenide (GaAs), a semiconductor, with metal-semiconductor-metal (MSM) diodes were tested on the EO sampling system. The fastest sample tested produced an electrical transient with a rise time of 330 fs and a full-width at half-maximum (FWHM) of approximately 510 fs.

## 2. Introduction to Semiconductors

Semiconductors are a group of materials that exhibit conductive properties of both metals and insulators. Their conductive properties depend on material fabrication and temperature. At low to medium temperatures, semiconductors are insulators, while at high temperatures they are good conductors. Interesting optical properties of semiconductors occur at the energy band gap edge. GaAs is the semiconductor of

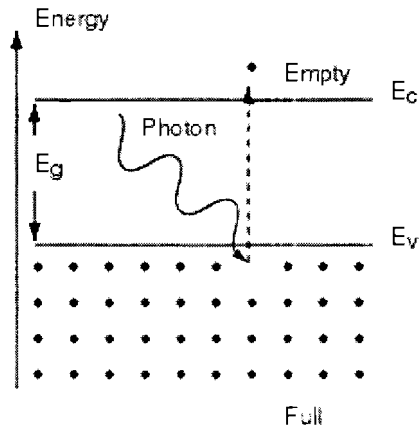
interest in this study. A standard energy-band diagram at not too high-temperatures that can be applied to this particular III-V compound is shown below (figure 2.1).

Figure 2.1- A generic energy-band diagram illustrates that the energy difference between the conduction band and the valence shell is known as the band gap energy.



The energy-band diagram shows the conduction-band edge ( $E_c$ ) above which all states are empty, the valence-band edge ( $E_v$ ) below which all states are occupied by electrons. The energy difference between ( $E_c$ ) and ( $E_v$ ) is the band gap energy ( $E_g$ ). The following diagram (figure 2.2) represents the same semiconductor exposed to light with photon energy ( $h\nu$ ) at least equal to  $E_g$ .

Figure 2.2- In order for a semiconductor to be excited into its conductive state, its electrons must absorb photons with energy ( $h\nu$ ) at least equal to the band gap energy ( $E_g$ ).

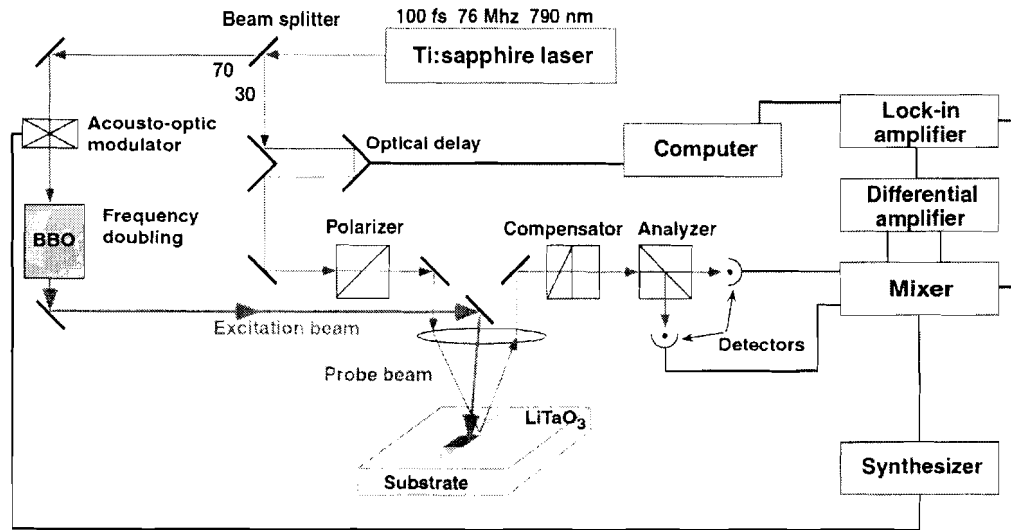


Absorption of photons with energy greater than that of the band gap results in generation of excited electrons that are now free to flow in the conduction band. These conditions allow a semiconductor to exhibit conductive properties when excited by light of the wavelength  $> E_g$ .

### 3. Introduction to Electro-Optic Sampling

The ultrafast testing of MSM structures on GaAs was conducted on an EO sampling system based on a commercial Ti:sapphire ( $\text{TiAlO}_3$ ) laser (Coherent Mira 900) pumped by an argon ion laser (Coherent Innova 420). EO sampling allows voltage waveforms of electronic/optoelectronic devices to be measured with subpicosecond resolution in a non-invasive manner. Such resolution cannot be achieved with any conventional oscilloscopes.

Figure 3.1- A schematic of the EO sampling system used.

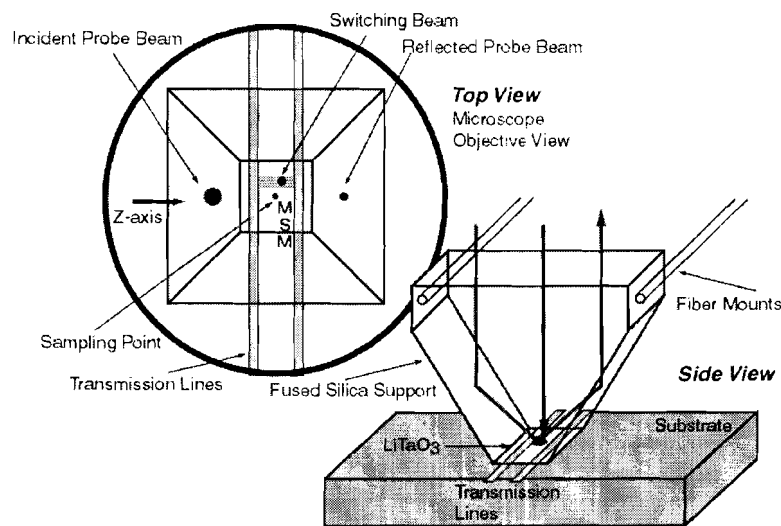


The laser beam emitted by the Ti:sapphire laser has a pulse width of  $\sim 100$  fs and a repetition rate of 76 MHz. The beam is split by a 30/70 beam splitter into an excitation beam and probe beam. Most of the power is diverted to the excitation beam to activate the photoconductive sample. A series of optics is used to direct the excitation beam to an acoustic-optic modulator to reduce noise. A  $\text{BaB}_2\text{O}_4$  crystal is then used to frequency double the beam to a wavelength of 395 nm. The conversion efficiency is dependent on the quality of the crystal and is low at best, resulting in the need for infrared filters. Each pulse of the beam is directed to the sample through a microscope and excites the photoconductive switch to generate an electrical transient along the transmission lines on the sample.

A set of optics and a computer-controlled translation stage ensure that the paths of both beams are equivalent and synchronized to begin. then the stage delays each successive pulse train of the probing beam to allow the probe beam to sample the electrical transient on the transmission lines. The probe beam is  $45^\circ$  linearly polarized

according to the optical axis of the EO crystal ( $\text{LiTaO}_3$ ). The beam is directed to the sample by the microscope through the EO crystal. As a result of the electric field on the transmission line, the refractive index of the EO crystal is altered, known as the Pockels effect. The change in refractive index modifies the polarization of the probe beam. Guided by the process of total internal reflection, the beam is returned to an analyzer, a pair of balanced photo detectors, and a series of electronic instruments that converts the change in polarization to intensity modification, then intensity modification to the strength of the voltage signal. In this manner, the amplitude of the electrical transient on the transmission line is measured.

Figure 3.2- An EO finger probe allows the characterization procedure to be non-invasive.



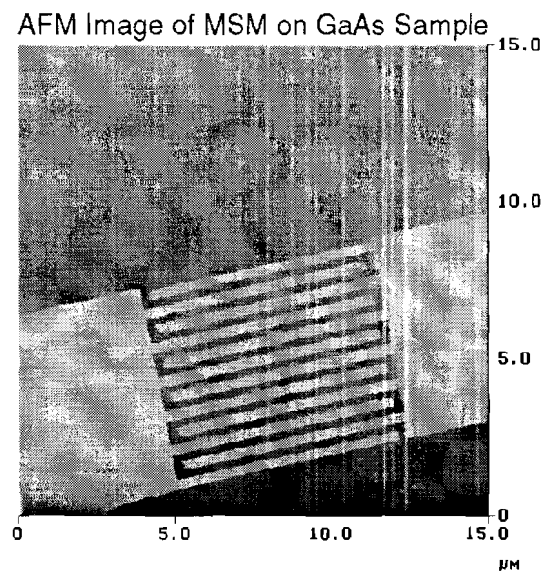
The diagram in Fig. 3.2 is a representation of the finger probe. A finger probe consists of an EO crystal with a fused silica support mounted to it in such a way that the angles of the support can provide total internal reflection for the probe beam entering the

cavity. The  $\text{LiTaO}_3$  can be mounted directly to a sample, but the use of the finger probe enables the process to be non-invasive.

#### 4. Analysis of MSM on GaAs Photoconductive Switch

A metal-semiconductor-metal (MSM) structure is a planar device, made by forming Schottky diodes on a semiconductor substrate. MSM laced switches play important roles because of their very high speeds and very sensitive responses. The following is an image of an MSM structure characterized in this study.

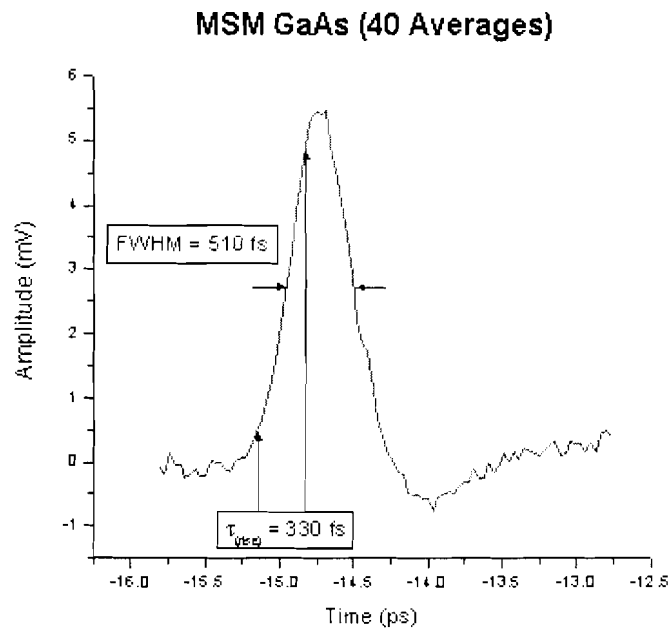
Figure 4.1- Image of one of the MSM on GaAs samples. Finger width is about 300 nm, finger spacing is about 200 nm.



MSM structures have been fabricated with finger spacing and width as small as 100 nm on low-temperature grown GaAs. The particular samples of MSM GaAs samples used in this study were of ~300 nm finger width and ~200 nm spacing.

The following is a graph generated from the data gathered from the EO sampling of the MSM GaAs sample depicted in the previous image.

Figure 4.2- A graph of the electrical transient measured. FWHM is approximately 510 fs.



Rise time is typically defined as amount of time measured from 10% of full amplitude to 90% of the full amplitude of a pulse. Full-width at half-maximum (FWHM) is the width of a pulse at 50% of the amplitude. From the data obtained, we can determine the rise time to be approximately 330 fs and the FWHM to be about 510 fs. Not only was this the fastest signal encountered during the course of this study, it was the cleanest signal as well. The data was a result of 40 averages and is relatively devoid of excess noise. The signal shown in Fig. 4.2 not only confirms that MSM diodes are one of the fastest optoelectronic devices known, but also demonstrates that the carrier generation

by light (pulse rise time) and relaxation (pulse fall time) happen at time scales well below 1 ps.

## **5. Conclusion**

High speed photoconductive switches can be characterized with subpicosecond resolution on electro-optic sampling systems. Over the last eight weeks I have been learning about EO sampling while testing various GaAs with MSM structures. Samples with pulse widths as short as 510 fs were measured with the use of an EO sampling system based on a 100 fs Ti:sapphire laser with a repetition rate of 76 MHz.

## **References**

- Chuang, Shun L., "*Physics of Optoelectronic Devices.*" pp. 1-17, 1995.
- Neaman, Donald A., "Semiconductor Physics and Devices: Basic Principles," pp. 2-3, 1997.
- Wang, Chia-Chi, "Ultrafast Testing of Electronic/Optoelectronic Devices," University of Rochester thesis proposal, 1996.

## **Acknowledgements**

I would like to thank Dr. Roman Sobolewski for guiding my progress throughout the summer. I would also like to express my gratitude to Xuemei Zheng and Brandon Jasionowski for spending so much time and effort helping me this summer. The entire group of graduate students I worked with was very friendly and extremely helpful. I wish everyone the best of luck.

# **Building and Characterizing 14GHz InGaAs Fiber Coupled Photodiodes**

Gabrielle Inglis

Advisor: Robert Boni

Laboratory for Laser Energetics  
University of Rochester

Summer High School Research Program  
2001

Abstract:

A method to actively align the 50 $\mu\text{m}$  diameter core of a multi-mode fiber to the 40 $\mu\text{m}$  diameter active area of a 14GHz InGaAs photodiode was developed. A fixture was designed to launch a  $\lambda=1.3\mu\text{m}$ , 100MHz rep-rate sub-picosecond FWHM laser pulse stream into the fiber and monitor the photodiode output while adjusting the relative alignment of the fiber, a relay lens and the photodiode active area. The bandwidth and responsivity of the detector were determined from the impulse response function. The fiber coupling technique maintained the 14GHz bandwidth capability of the photodiode and achieved a Beta (electron charge out, to photon energy in) ratio of 0.38 Coulombs per Joule. The intrinsic Beta of InGaAs, by comparison, is 0.95 Coulombs per Joule at  $\lambda=1.3\mu\text{m}$ .

## Motivation:

The bandwidth of a measurement system is limited by its slowest component. At LLE, measurements using pulsed lasers are typically made with 6GHz photodiodes and oscilloscopes. Recently, oscilloscopes with bandwidths in excess of 6GHz have become common. The 14GHz detectors will eventually replace the 6GHz detectors currently used to make most oscilloscope-based measurements. In particular, measurements made using 7GHz oscilloscopes will benefit from these faster detectors. When a 6GHz detector is used with a 7GHz oscilloscope, the combined bandwidth is lower than 7GHz. A 14GHz detector allows measurements to be made closer to the full bandwidth capability of the oscilloscope.

There is another measurement niche for the 14GHz detector. Streak cameras are used at LLE to make the highest bandwidth measurements. These streak cameras are orders of magnitude larger, heavier, and more expensive than a photodiode and an oscilloscope. Their size and weight make streak cameras less accessible to every part of the laboratory. In addition, the expense and complexity of using streak cameras limits their availability. A 14GHz detector and a fast oscilloscope are an adequate substitute for all but the most bandwidth-demanding measurements. For example, fast rise-time and temporally shaped laser pulses are adequately characterized with a 14GHz detector and a 7GHz oscilloscope when adjusting the laser that generates the shaped pulses. However, the final measurement to qualify shaped pulses for OMEGA is still made with streak cameras.

### Design Objective:

The objective was to build a palm-size, 9V battery-powered, 14GHz InGaAs detector with an FC fiber input receptacle and an SMA electrical output connector that could be coupled directly to an oscilloscope. In addition, it was desirable to image couple the fiber output to the detector active area. This would allow the flexibility of using a wide variety of fibers to deliver light to the detector. The ratio of electron charge output from the detector to photon energy launched into the fiber, called the responsivity or Beta of a detector, of 0.33 Coulombs per Joule was set as a reasonable goal.

### Primary Components Used in the Design:

Figure 1 is an exploded view of the primary components of the 14GHz detector. The enclosure has been omitted for clarity. The 14GHz photodiode is supplied mounted to the backside of an electrical SMA connector with a bias resistor and terminals for applying a bias voltage. The photodiode was covered with a 200 $\mu$ m thick transparent epoxy layer to protect the 40 $\mu$ m diameter active area. An FC style receptacle was selected to take advantage of the FC standard which supports both multi-mode and single fibers along with angle-polished and polarization-maintaining fibers. A molded glass aspheric lens was chosen to image relay, with a magnification of less than one, the 50 $\mu$ m diameter fiber output to the 40 $\mu$ m diameter photodiode active area.

### The Detector Design and Assembly:

A fixture was designed and built to hold the photodiode stationary while the FC receptacle and the imaging lens could be moved together, in three dimensions, using

micrometer-driven stages. By launching a pulsed laser into the fiber and monitoring the photodiode output with an oscilloscope, the micrometer stages could be moved until the best signal was obtained. The photodiode mount and the FC receptacle were soldered to either side of a brass mounting bracket making the FC mount, the relay lens and the photodiode mount a single rigid detector assembly (Figure 2). The detector assembly was mounted in a custom-designed enclosure that contained the bias battery and safeguarded the detector from being damaged when handled. The combination of fixtures and real-time alignment was an effective method to accurately align the image of the fiber output to the active area of the photodiode.

#### Detector Performance: Data Acquisition

The sub-picosecond laser pulse stream used to actively align the detector assembly also provided the excitation source needed to measure the detector's impulse response. Since the Fourier spectrum of a sub-picosecond pulse has equal energy frequency components well past 14GHz, the detector's response to this pulse contains the information needed to determine the detector's gain as a function of frequency. This is a very detailed method to measure bandwidth. By measuring the average energy of each laser pulse and the charge that flowed through the detector, the Beta of the detector was also calculated. The instrumentation setup used to capture the impulse response of the detector, to measure the average energy of each laser pulse and to determine the charge that flowed through the detector is shown in Figure 3.

## Detector Performance: Data Analysis

A software program was developed to analyze the impulse response function of the 14GHz detector to determine its bandwidth. The analysis technique is based on the principle of superposition, which states that an arbitrary signal can be constructed from a summation of sinusoidal signals of the proper amplitude and frequency. The Fourier transform of a time varying signal is exactly this set of frequencies and amplitudes. Since a sub-picosecond laser pulse excites the detector, with equal energy, at all frequencies well above 14GHz, the amplitude of each Fourier frequency is a relative measure of the detector's gain at that frequency. Bandwidth is defined, by convention, to be the frequency at which the gain of a detector is 3dB below its gain at zero Hertz, also called the D.C. response. Figure 4 shows the time domain impulse response of the detector and its Fourier transform, called the frequency response of the detector, with a vertical line drawn at the frequency of the -3dB amplitude point.

## Detector Performance: Bandwidth

Characterizing the response of a detector with a single parameter, in this case bandwidth, is useful when the objective is to simply sort detectors based on speed. When using a detector to accurately measure the bandwidth of another system, or device, it is necessary to know the full frequency response of the detector. If left uncorrected, the variation of gain, with frequency, of the 14GHz detector, as seen in Figure 4, would bias the results from measurements using this detector. This variation of gain with frequency can be removed from the measured response of a system under test by the additional application of Fourier techniques.

## Detector Performance: Responsivity (Beta)

The responsivity of the detector was calculated as the ratio of electron charge conducted by the detector per pulse to photon energy per pulse launched in the fiber. The electron charge per pulse was calculated by integrating the impulse response function and dividing by the  $50\Omega$  load resistance of the oscilloscope. The average energy per laser pulse was calculated by dividing the average laser power by the laser pulse rate. The 14GHz detector assembly has a Beta (Coulombs/Joule) of 0.38. The intrinsic Beta of InGaAs photodiodes is 0.95 Coulombs/Joule. The reduced responsivity was probably caused by the image of the  $50\mu\text{m}$  fiber overfilling the  $40\mu\text{m}$  active area of the photodiode. The fixture did not allow for adjustment of the relay lens relative to the fiber output. This could result in the  $50\mu\text{m}$  fiber being imaged with a magnification greater than one onto the  $40\mu\text{m}$  photodiode active area. This would overfill the active area and reduce the responsivity. In addition, the protective, transparent, epoxy lump covering the active area of the photodiode was of poor imaging quality and probably prevented the fiber image from coming to a sharp focus, further reducing the optical coupling efficiency.

## Conclusion:

All of the design objectives of the project were achieved. The 14GHz inherent bandwidth of the photodiode was preserved with the alignment, assembly and packaging approached used. The fiber input to the detector was through an FC type fiber coupler and was image relayed onto the  $40\mu\text{m}$  active area of the photodiode. The responsivity of

the detector, calculated as the ratio of electron charge conducted through the detector to photon energy injected into the fiber, of .38 exceeded the .33 design requirement.

#### Acknowledgments:

The successful completion of my summer research project would not have been possible without the help of Mr. Robert Boni, my advisor. Mr. Boni's guidance and encouragement kept me moving forward along the correct path. I appreciated the opportunity he gave me to struggle on my own to solve problems, yet he managed to drop in just when I was truly stuck and not making any progress. I would also like to extend my gratitude to Mr. Joseph Henderson, the machinist in the student machine shop, for instructing me on the safe operation of the shop equipment. I have a new appreciation, even from the small scale of my project, for what it takes to design, build and test scientific instruments. Finally, I would like to thank Dr. Craxton for organizing the summer research program.

Figures:

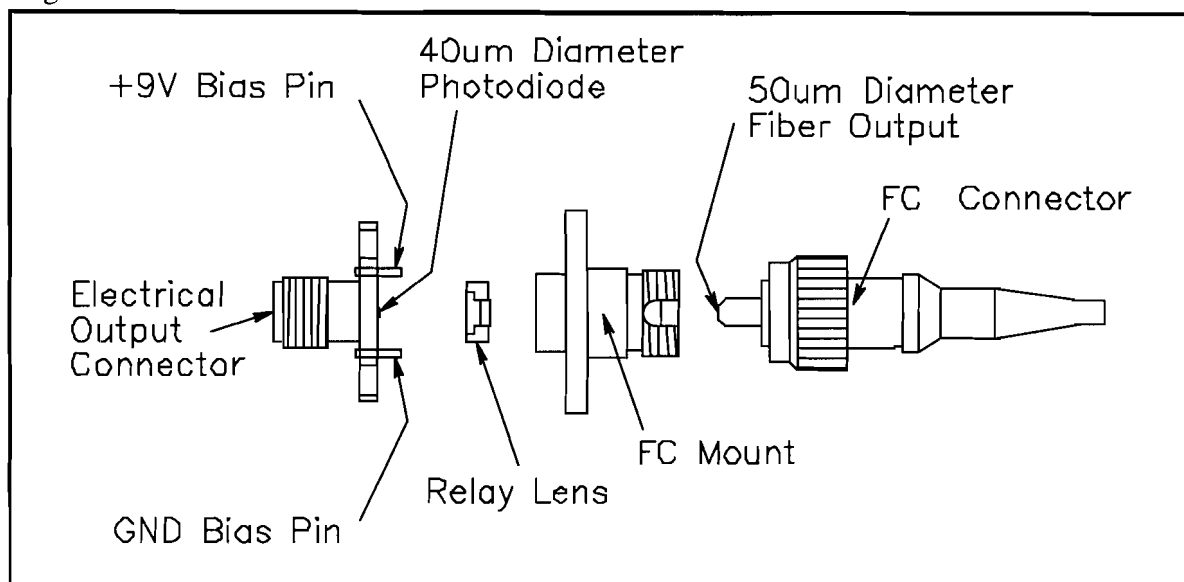


Figure 1.

An exploded view of the primary components of the 14GHz detector is shown. Laser light is delivered by a fiber optic terminated by the FC connector. Once assembled and aligned, laser light emitted from the 50 $\mu$ m diameter fiber is imaged by the relay lens onto the 40 $\mu$ m active area of the photodiode. The electrical output connector is attached to an oscilloscope to read out the signal.

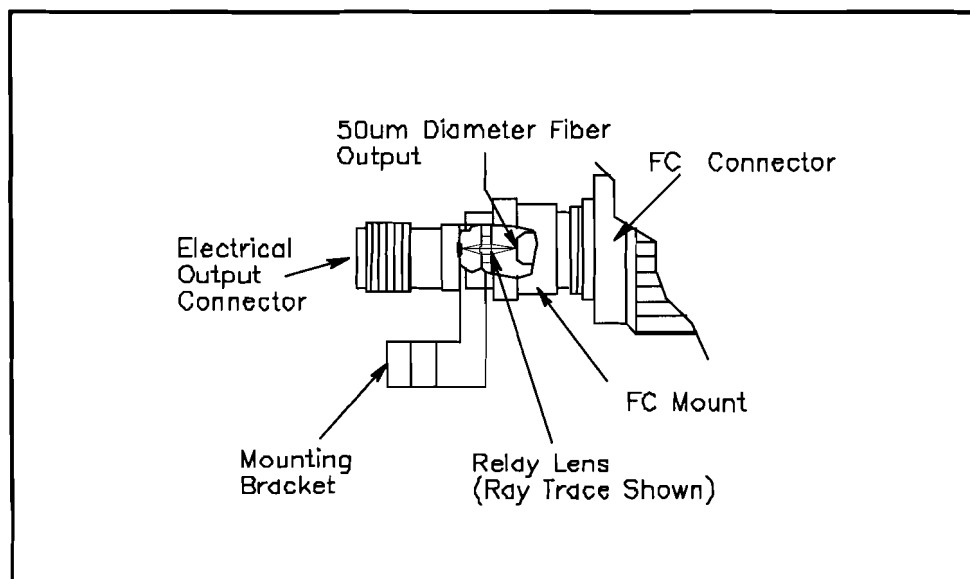


Figure 2.

A cutaway view of the assembled detector is shown. The mounting bracket is the mechanical "bridge" between the electrical output connector, which holds the photodiode, and the FC mount, which holds the relay lens. When the FC mount and electrical connector are aligned to produce the best signal, the FC mount, the mounting bracket, and the electrical connector are soldered together creating a rigid monolithic detector assembly.

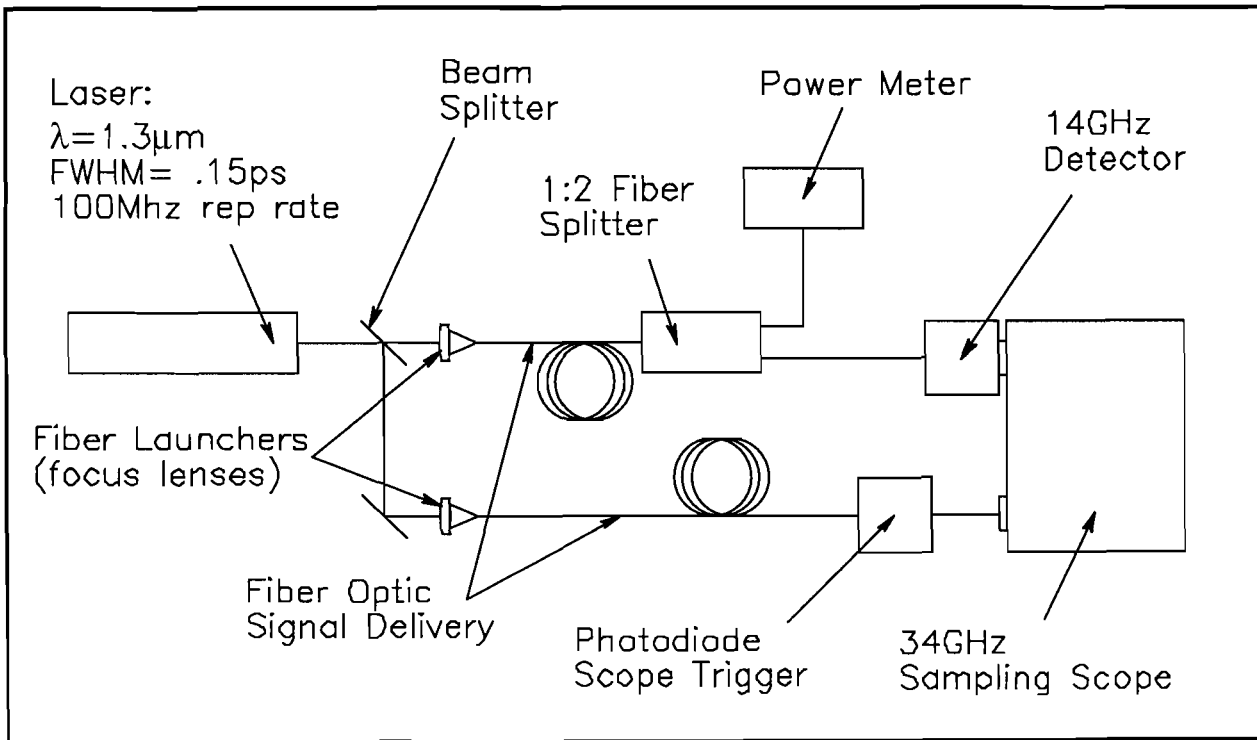
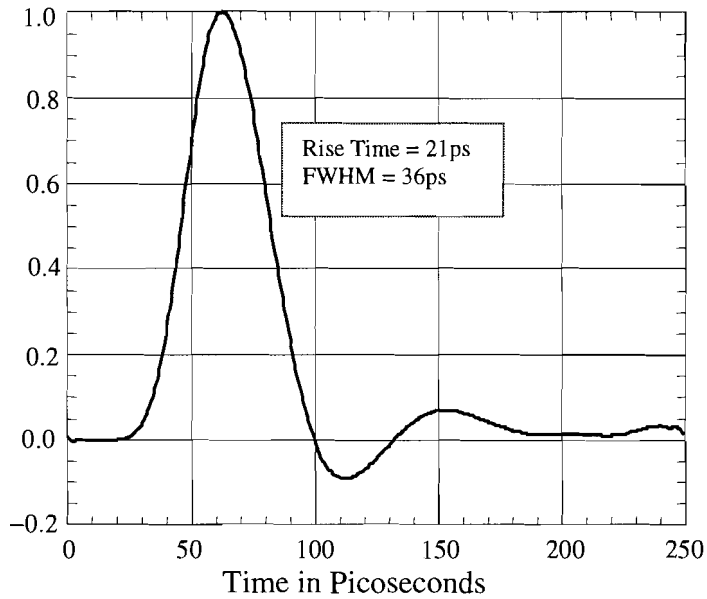


Figure 3.

The experimental setup used to capture the impulse response of the 14GHz detector and determine the average energy per laser pulse. A 100MHz rep-rate laser is split into two beams and launched into separate fibers. The first fiber is split into two branches. One branch measures the average power of the laser, the other branch delivers the pulse stream to the 14GHz detector. The second fiber goes directly to a photodiode used to trigger the 34GHz sampling scope.

Normalized Impulse Response of the 14GHz  
Detector -vs- Time in Picoseconds



Gain in Decibels of the 14GHz  
Detector -vs- Frequency in GHz

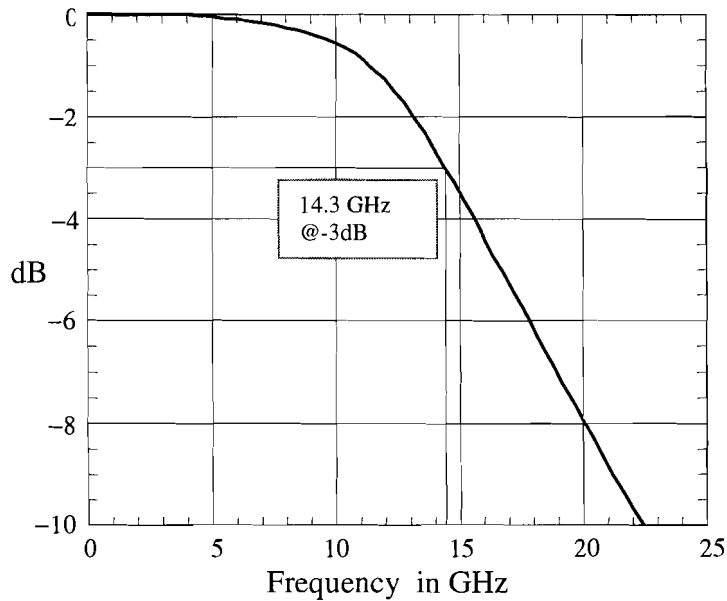


Figure 4.

The normalized response of the detector to a sub-picosecond pulse is shown in the top figure. The 21ps, 10% to 90%, rise time is consistent with the 14GHz expected bandwidth. The lower figure is the frequency response obtained from the Fourier transform of the impulse response. A frequency of 14.3GHz is indicated at the -3dB gain point. This frequency, by convention, is called the bandwidth of a detector.

**Guest- Host Dye Systems for Liquid Crystal**

**Electro- Optical Device Applications**

Jennifer Jung

Advisor: Kenneth L. Marshall

Victor Central School

**Laboratory for Laser Energetics**

University of Rochester

High School Research Program

2001

Nematic liquid crystals are desirable for the liquid crystal point diffraction interferometer (LCPDI) because they respond readily to electric and magnetic stimuli. Liquid crystals are used in the LCPDI to produce phase shifting, which is achieved by applying a voltage. The LCPDI device is desirable as a diagnostic tool both for testing aberrations in the optics of the OMEGA laser and for NASA experiments in microgravity fluid physics. As drive voltages for the LCPDI increase, the contrast of fringes begins to fade. In order to match the output intensities of the object beam front and reference wave front, a mixture of negative and positive dichroic dyes (the “guests”) are needed to blend with the nematic liquid crystal Merck E7 (the “host”).

## **Project goal**

The LCPDI requires a dye with a consistently high optical density (O.D.) at 543.5 nm. Previous research has shown that negative dichroic dyes are desirable because their optical density increases with increasing voltage. However, negative dichroic dyes are not commonly available, and have to be synthesized. These dyes are needed at relatively high percentages, which creates some complications in the guest-host dye system. An ideal dye candidate for blending with Merck E7 would have (1) good solubility at high concentrations; (2) a high “order parameter” (S) in the E7 “host” (the maximum attainable value of S is 1); (3) a high dichroic ratio to maximize contrast; and (4) a high optical density at 543.5 nm.

A series of negative dichroic anthraquinone dyes were synthesized and purified for this project. These dyes were added to Merck E7 nematic liquid crystal at different percentages to determine the solubility limit. Once the solubility limit was obtained, these mixtures were used to fabricate cells for finding the order parameter and dichroic ratio of the dye. The Lambda 900 spectrophotometer was used to determine both the dye maximum wavelength ( $\lambda_{\max}$ ) in E7 and the O. D. at different applied voltages.

The ultimate goal of this project was to create a balanced mixture of negative and positive dichroic dyes in Merck E7 for the LCPDI device that would maintain an O.D. of 2 independent of applied voltage.

## **Structure and Properties of Liquid Crystals**

Mesogens are the molecular components that make up a liquid crystalline phase. These molecules are rigid/ rod shaped, and align along a common axis called the director.

Liquid crystals (LC) exist in a “mesophase,” an intermediate phase between a solid and isotropic liquid state, thus having a unique double melting point. A perfect crystal has an order parameter of one, while an isotropic liquid has an order parameter of zero. The order parameter  $S$  of a liquid crystalline material usually ranges from 0.3 to 0.9. Due to a common alignment direction and the unique shape of the molecules, mesogens exhibit anisotropic properties (properties that vary due to the direction of measurement). In terms of optical properties, liquid crystals exhibit multiple refractive indices (ordinary and extraordinary,  $n_o$  and  $n_e$ ), which results in birefringence (defined as  $\Delta n = n_e - n_o$ ). The observed magnitude of the LC birefringence depends on the direction of its optical axis with respect to the incident light.

Liquid crystals can be separated into three categories, depending on their degree of order. Nematic liquid crystals are the least ordered. The long axes of these mesogens align parallel to each other. Nematic liquid crystals are desirable for the LCPDI because they readily respond to electric and magnetic stimuli. Cholesteric liquid crystals align similar to nematics, but protruding side groups cause the long axes of the mesogens to stack on top of each other in a helical fashion. These structures have a high optical activity and readily rotate plane polarized light. Smectic liquid crystals are the most highly ordered. The molecules align parallel to each other, but can organize into rows, and in some cases, rows and columns that are free to slide past each other.

When pure nematic liquid crystals are placed into a cell, in the absence of external forces or effects they tend to align parallel to the substrates. If the nematic liquid crystal molecules have large dipoles parallel to the molecular axis, they will align with an electric field applied perpendicular to the glass substrates. The liquid crystal mixture

Merck E7 used in these experiments is composed of cyanobiphenyl and cyanoterphenyl compounds, as shown below in Fig. 1. The cyano (CN) group has a large dipole moment.

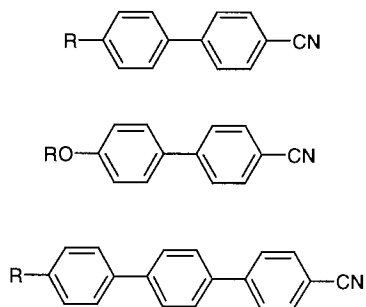


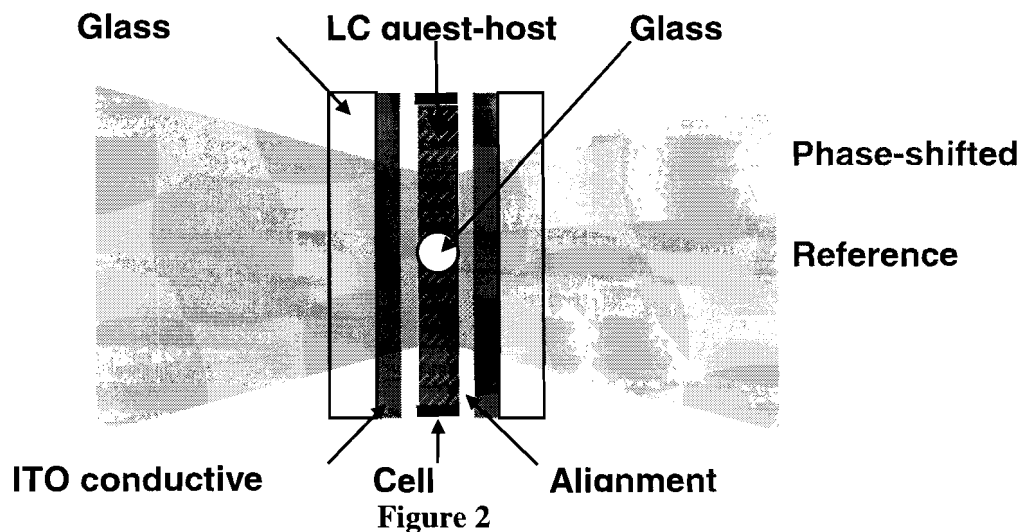
**Figure 1**

### **The LCPDI**

To optimize the performance of the OMEGA laser, the hundreds of lenses and optical parts in the system must be tested for aberrations. The LCPDI is a better tool than a commercial interferometer for testing both OMEGA optics and for NASA experiments in microgravity fluid physics because it is small and compact (about the size of a quarter), insensitive to environmental factors such as air currents and vibrations, and is substantially less expensive. Figure 2 shows the configuration of the LCPDI. The main structure of the LCPDI consists of two pieces of glass that each contain an electrically conductive coating of mixed indium- and tin oxides (ITO). This coating allows voltage to go through the cell. The substrates were cleaned and spin coated with nylon polymer dissolved in formic acid. The nylon acts as an alignment layer to insure that all of the LC molecules are pointing in the same direction. After drying on a hot plate, the substrates were buffed. Buffing is essential to the fabrication of a cell. This process produces microscopic scratches in the nylon coating of the substrate. These scratches allow the LC material to align in the cell with all of the LC molecules pointing in a common direction. The cell gap was created using glass beads with a 22-micron diameter mixed in an UV –

curing epoxy mixture. The beads were placed at each of the four corners of the cell, which sets the cell gap/ path length of the cell at 22 microns. Using a microscope, a polystyrene divinyl benzene microsphere having a diameter ranging from 22- 42 microns is placed in the middle of the cell. Because the plastic microsphere in the middle of the cell is larger in diameter than the cell gap, it is compressed into a more cylindrical shape when the glass plates are bonded together. The cell is then filled with the LC fluid and sealed with epoxy to prevent fluid leakage. Wires are applied to the outside of the cell.

The LCPDI device uses a green helium neon laser. As the beam enters the cell, the plastic microsphere splits the beam into two, producing a reference wave front (the portion of the beam that went through the plastic microsphere), and an object beam front (the portion of the beam that passed through the LC matrix)\*.




---

\*C. Mercer and K. Creath, "Liquid- Crystal Point- Diffraction Interferometer for Wave- Front Measurements", Appl. Opt. 35, (10), 1996.



**Figure 3**

Figure 3 above compares interference fringes from an actual LCPDI device (left) to those generated by a computer simulation (right). The simulation shows the effect when there is an aberration in the object beam.

### Dichroic dyes

Because the cross-sectional area of the portion of the laser beam passing through the glass reference bead in the LCPDI is substantially smaller than that passing through the LC fluid, the intensity of the two beams is mismatched and the fringe contrast is poor. To solve this problem, a “guest” dye is added to the LC “host” to equalize the intensity in the two beams. Currently, the LCPDI utilizes Oil Red O (Fig. 4), an oil-soluble dye with an elongated molecular structure that has *positive absorption dichroism* (absorbance decreases with applied electric field).

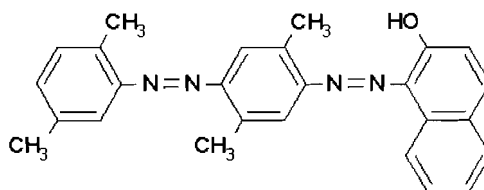


**Figure 4**

This effect is observed because the  $\pi$ -electron cloud responsible for the absorption in these molecules is distributed *along* the molecular axis. Positive dichroic dyes have been used up to now because of they are readily available and highly soluble in the liquid crystal host. However, this voltage-induced change in fringe contrast is very undesirable and limits the capabilities of the LCPDI device. One way to solve this problem that has been demonstrated in previous research is to add dyes with *negative absorption*

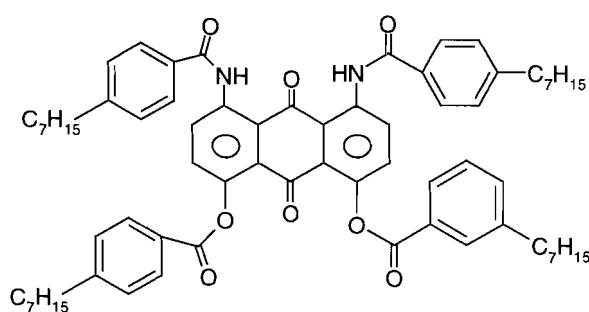


**Figure 5**

*dichroism*, (e.g., anthraquinone dyes, Fig.5 ) in which the optical density *increases* with increasing voltage, to guest-host mixtures containing positive dichroism dyes to reduce or eliminate the voltage dependence of the contrast. Unlike positive dichroic dyes, negative dichroic dyes such as anthraquinones have a  $\pi$  electron distribution cloud that extend *out and away* from the long molecular axis.

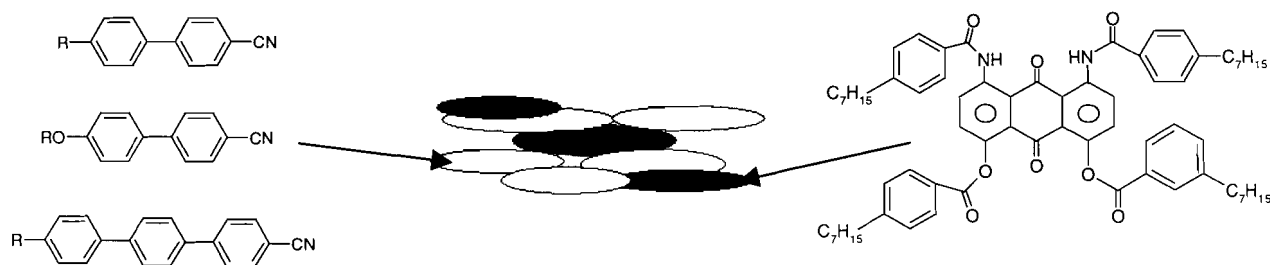


**Figure 6**

Guest- host dye systems are composed of mixtures of dye molecules, the “guest,” introduced into a nematic liquid crystal “host” (Figure 6). In the experiments reported

here, negative dichroic dyes based on anthraquinone were used as the “guest” and the host was Merck E7. The magnitude of absorption depends strongly on molecular structure. These anthraquinone based dichroic dyes are fairly easy to synthesize, however, purification of these dyes is very difficult.

The anthraquinone dyes used in this work were synthesized at LLE and contained either two or four reactive sites. As an end product, mixtures of mono- and multiple-substitution products were generally obtained (Fig. 7). Complexities arose in creating higher concentrations of dye in the guest- host dye systems that would maintain solubility

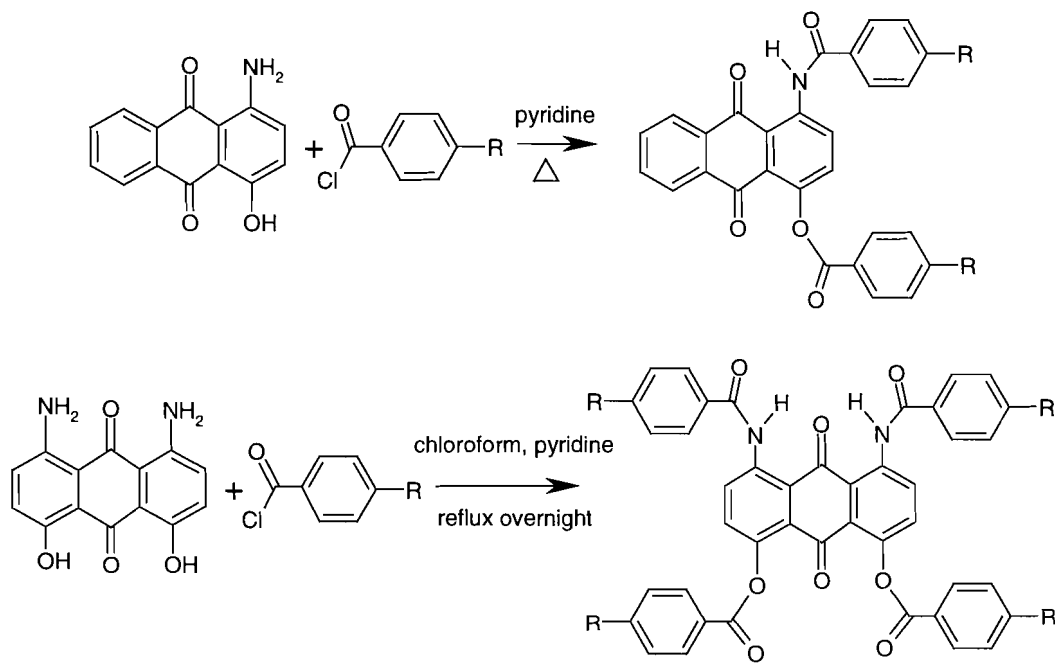


**Figure 7**

in Merck E7. Before inserting the guest- host mixture into a cell, the solubility limit was obtained. Dye solubility limits in the LC host were determined using a simple “sedimentation” experiment\*. Samples of each dye were weighed and added to 1 gram of

\*Irene Lippa, “Synthesis of Nickel Dithiolene Dyes and Analysis of Solubilities in a Nematic Liquid Crystal Host”, LLE Summer High School Research Program, 1998

Merck E7. Concentrations of dye ranged from 0.1% - 5%. The mixture was stirred and heated to 80° C (well above the liquid crystal clearing point of 65° C) for two hours. After the mixtures cooled, they were filtered through a 0.45-micron Teflon membrane filter. Slides were then prepared, and were observed every 24 hours both visually and by microscopic inspection for signs of precipitation, as shown in Fig. 8 for a 0.5 wt% mixture of 9 heptylbenzoyl dye in E7.



**Figure 8**

After the solubility limit had been found, the guest- host dye mixture was injected into a cell. The Lambda 900 spectrophotometer was used to find the absorbance of the dyes at different voltages. Voltages applied to the cell ranged from 0.1- 10 V at 1 kHz sine wave. After collecting data on the absorbance of each cell, the dichroic ratio and order parameter were determined. The dichroic (contrast) ratio is the absorbance of the dye molecule in the perpendicular orientation divided by the absorbance of the dye molecule in the parallel orientation. Ideally, the dichroic ratio should be as high as possible.

Of all the negative dichroic dyes tested, the tetrasubstituted 1,8-bis-(heptylbenzoylamino)-4,5-bis-(heptylbenzoyloxy)anthraquinone (Fig 9) at 1 wt % in E7 was found to be the most promising for the LCPDI. Unfortunately, higher percentages of

this dye are needed, but cannot currently be achieved due to solubility issues. Overall, this tetra- substituted heptyl derivative had the best combination of solubility, order parameter, and dichroic ratio. The  $\lambda_{\max}$  in chloroform was 526 nm, but in E7 the  $\lambda_{\max}$  underwent a bathochromic (red) shift to 537nm.

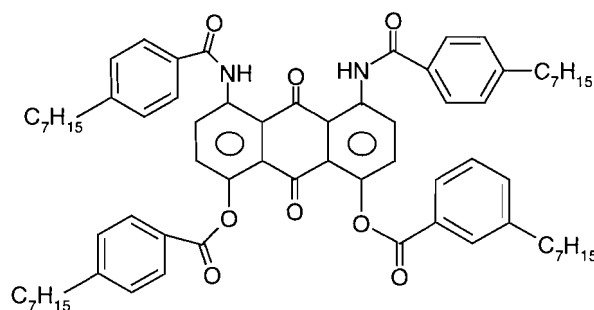
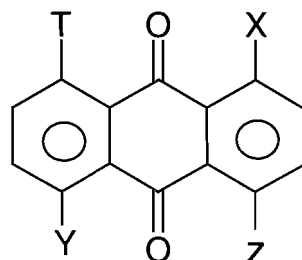


**Figure 9**

The same shift was also observed in “heptylbenzoyl”, which also contained heptyl groups substituted at the positions T and X (Fig 10). Heptylbenzoyl (a purple dye), had a



Functional Group:				Solubility limit	$\lambda_{\max}$ (CHCl <sub>3</sub> )	$\lambda_{\max}$ (E7)	D (543nm)	S
T	X	Y	Z					
H <sub>15</sub> C <sub>7</sub> PhC=ONH	H <sub>15</sub> C <sub>7</sub> PhC=ONH	H <sub>15</sub> C <sub>7</sub> PhC=OO	H <sub>15</sub> C <sub>7</sub> PhC=OO	1%	526 nm	537 nm	4.3	0.435
H <sub>9</sub> C <sub>4</sub> PhC=ONH	H <sub>15</sub> C <sub>7</sub> PhC=ONH	H <sub>9</sub> C <sub>4</sub> PhC=OO	H <sub>9</sub> C <sub>4</sub> PhC=OO	<0.1%	521 nm	-	-	-
H	H <sub>15</sub> C <sub>7</sub> PhC=ONH	H	H <sub>15</sub> C <sub>7</sub> PhC=OO	>3%	427 nm	410 nm	1.4	0.223
H	H <sub>17</sub> C <sub>8</sub> PhC=ONH	H	H <sub>17</sub> C <sub>8</sub> PhC=OO	>5%	427 nm	403 nm	1.6	0.274
H <sub>15</sub> C <sub>7</sub> PhC=ONH*	H <sub>15</sub> C <sub>7</sub> PhC=ONH	OH	OH	0.125%	550 nm	552 nm	12.8	0.480

**Figure 10**

dichroic ratio of 12.8:1. A hypsochromic (blue) shift on changing the host from chloroform to E7 was observed in heptylbenzoylamino and octylbenzoyl, which both had groups substituted at positions X and Y. Both of these dyes also exhibited high solubility in E7, (octylbenzoyl at >5%, and heptylbenzoylamino at >3%). From the data collected, it can be determined that the  $\lambda_{\max}$  depended on both the host composition and dye structure.

An initial test cell containing 0.8206g of 1 wt % tetraheptylbenzoyl in Merck E7 and 0.0106g of 2 wt. % Oil Red O in E7 was assembled and evaluated (Fig 11). This guest- host dye mixture was prepared by blending two stock mixtures of positive and negative dichroic dyes. No miscibility or conductivity problems were observed. At 543.5 nm, the O.D. was 3 over a range of 0 -1 volts, but the O.D. dropped at higher voltages (Fig. 12). From this analysis, it was concluded that larger concentrations of negative dichroic dyes will be needed to produce voltage- independent contrast.

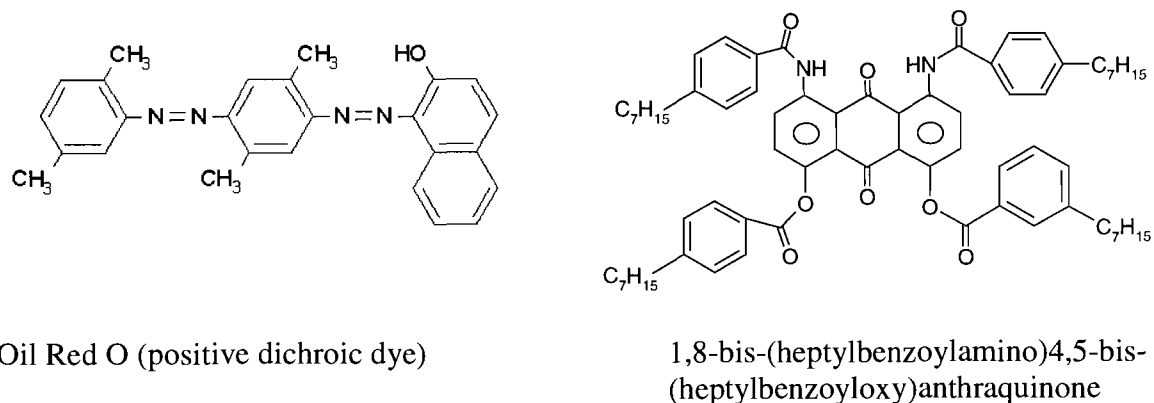


**Figure 11**

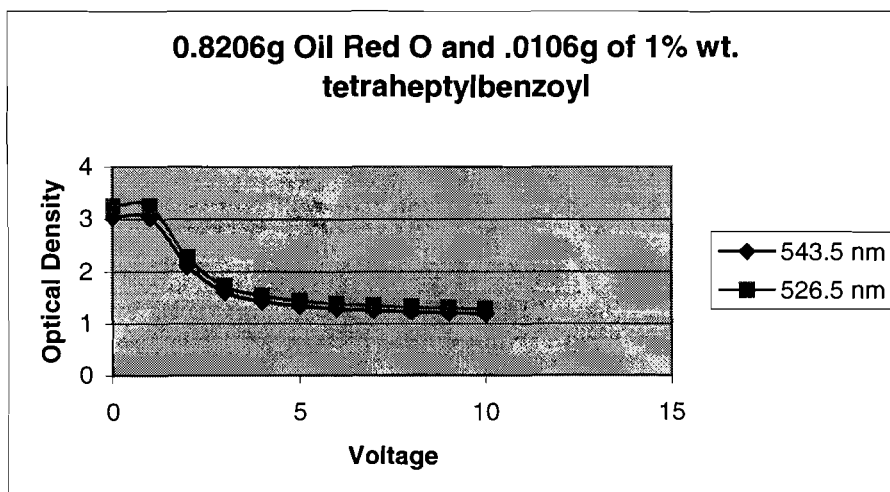


**Figure 12**

### Summary

Negative dichroic dyes are expected to enhance the performance of the liquid crystal point diffraction interferometer. The LCPDI is desirable as a diagnostic tool for testing aberrations in the lenses of the OMEGA laser and for NASA experiments in microgravity fluid physics. Due to the unique structure and properties of negative dichroic dyes, the optical density increases with an increase in voltage. The  $\lambda_{\max}$  of anthraquinone-based negative dichroic dyes shift either to longer or shorter wavelengths (depending on molecular structure) when dissolved in a nematic LC host. Select anthraquinone dyes displayed outstanding solubility characteristics in nematic LC. In the future, mixtures of Oil Red O and negative dichroic dyes are expected to improve the contrast of fringes in current LCPDI devices.

## **Acknowledgments:**

I gratefully acknowledge the following individuals and organizations:

- My project advisor, Kenneth L. Marshall, for the opportunity to work with him and all the assistance that I was given.
- NASA Glenn Research Center (Cleveland, OH.)
- Laboratory for Laser Energetics, University of Rochester
- Program Supervisor: Dr. R. Stephen Craxton
- Materials Lab Staff and Students:
  - Benjamin Schudel
  - Aaron Flanders
  - Brett Klehn
  - Gloria Olivier
  - Sarah Mitchell
  - Bryan Watson
  - Irene Lippa
  - Nick Turner
  - Jalil Shojaie

# Numerical Modeling of Optical Parametric Chirped Pulse Amplification to Design a Petawatt Laser Front End

by Josh Keegan

LLE Advisor: Mark Guardalben

## Abstract

A numerical model of optical parametric chirped pulse amplification (OPCPA) was developed and used to investigate two designs for the front end of a proposed petawatt laser, which is a very high intensity laser. A petawatt laser is required for fast ignition, a new technique that has the potential to greatly benefit the study of Inertial Confinement Fusion (ICF) and is being investigated at various laboratories around the world. The first design, which is for a proof-of-principle experiment, was one which attempts to preserve the spectral characteristics of the input pulse in order to obtain a short temporal pulse width upon recompression. The second design, which is for the actual petawatt laser system, was one which modifies the spectral characteristics of the input pulse in a way that is desirable for injection into the glass amplifier chain. In both cases the number of crystal stages required and the approximate crystal lengths were determined using the model. The proof-of-principle design requires four crystals of BBO while the actual front end system design requires three longer BBO crystals.

## 1. Introduction

Inertial Confinement Fusion (ICF) is of interest as a possible energy source, and studies

of ICF are in progress in several laboratories around the world, including the University of Rochester Laboratory for Laser Energetics (LLE) and the Lawrence Livermore National Laboratory in the U.S., and Rutherford Appleton Laboratory in the U.K. In ICF, a target filled with deuterium and tritium is illuminated with a high-intensity laser pulse, causing a fusion reaction of the deuterium and tritium atoms that produces helium atoms and high-energy neutrons as by-products. This process is initiated by ablation of the target shell, which according to Newton's Third Law produces an opposite and equal reactive force that implodes the fuel at the center of the target, compressing it to higher density. Uniformity of the incident laser beams and the target surface are necessary to produce the central ignition hot spot. <sup>(1)</sup>

Fast ignition is a new technique that has the potential to increase overall efficiency while decreasing the requirements for uniformity of illumination and the target surface <sup>(1)</sup>. Studies of fast ignition are now in progress in various countries around the world, including Japan, Germany, England, and France <sup>(2)</sup>. In the fast-ignition concept, a laser having a long pulse width ( $\sim 10^{-8}$  s) compresses the target while a petawatt ( $10^{15}$  W) laser having a short pulse width ( $\sim 10^{-12}$  s) is used to heat the target at the point of maximum target compression. The amplification stages of a petawatt laser system are shown in Fig. 1: a seed pulse having low energy is produced by a laser oscillator and injected into a front end amplification stage. A glass amplifier chain further amplifies the laser pulse until sufficient energy is achieved, at which point the pulse is delivered to the target.

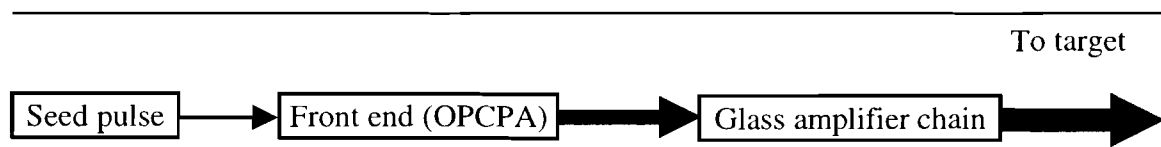


Fig. 1. Petawatt laser amplification stages. A low-energy pulse produced by an oscillator is amplified by the front end, which in this case will use OPCPA. The front end output pulse is injected into a Nd:glass amplifier chain for further amplification and eventual delivery to the target.

---

Optical parametric chirped pulse amplification (OPCPA) is currently under consideration as a possible front end amplification technique. In OPCPA a short pulse (~100 fs) is temporally stretched using diffraction grating pairs (to ~5 ns), lowering the power of the input pulse while preserving the pulse's total energy\*, thereby allowing higher pulse energy after amplification without damage to the gain medium. The stretched pulse is amplified by propagation through several stages of nonlinear optical crystals and a glass amplifier chain, after which it is recompressed with another diffraction grating pair and delivered to the target. OPCPA is proposed as the front end amplification technique because preservation of bandwidth is essential to obtain good recompression, and OPCPA is a broadband amplification technique (meaning that there is little loss of bandwidth). The gain bandwidth of Nd:glass amplifiers is too small to be used as a front end amplifier.

A model of OPCPA which solves the coupled wave equations by numerical integration was created and used to investigate two designs for the front end of a petawatt laser system which is being proposed for integration into the OMEGA laser at the University of Rochester Laboratory for Laser Energetics. In each case various design parameters were determined, including the number and approximate length of crystal stages required for various output pulse energies and spectra. In the first design for a proof-of-principle experiment to demonstrate the OPCPA technique, four BBO crystals were used for a total crystal length of 32.7 mm, while in the front end design for the actual system three BBO crystals with a total length of 39 mm were used. In both cases a 1 nJ pulse was amplified to 300 mJ. Both designs were optimized for efficiency. The proof-of-principle design uses 2.61 J of pump energy while the actual system design uses 1.90 J of pump energy.

---

\* There is a slight energy loss on the grating; some gratings have efficiencies ~ 96%

## 2. Theoretical Description of OPCPA

The amplification and subsequent recompression of chirped optical pulses was first demonstrated by Strickland and Mourou at LLE in 1985.<sup>(3)</sup> The current implementation of chirped pulse amplification (CPA) uses paired diffraction gratings to temporally stretch the pulse and an additional set of gratings in a different configuration to recompress the pulse after amplification (see Fig. 2).

---

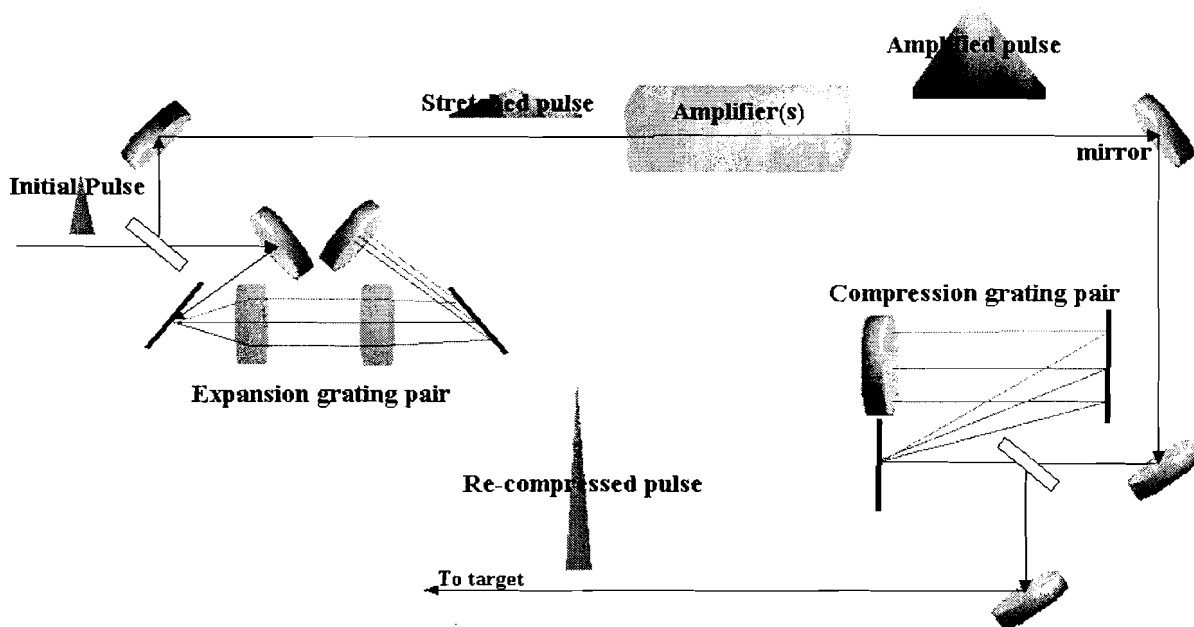


Fig. 2. Overview of CPA. A short, low-energy pulse is temporally stretched using paired diffraction gratings, amplified, and then recompressed, again using diffraction gratings. This technique leads to a very high-power recompressed pulse without damage to the gain medium or other optics.

---

Shorter temporal laser pulses must necessarily contain a broader spectrum due to the Fourier relationship between time and frequency. The expansion grating pair is configured such that the shorter wavelengths of the pulse spectrum travel a longer distance, causing the pulse to be stretched in time and lowering the pulse peak intensity, thus reducing the potential for damage to the gain medium. This means that the longer wavelengths are at the front of the pulse while the shorter wavelengths are at the end. The process used in the compression grating pair is

similar to that used in the expansion grating pair although a different configuration causes the longer wavelengths of the pulse spectrum to travel longer distances, essentially canceling the effect of the expansion grating pair. However, amplification of the pulse prior to recompression results in a recompressed pulse of very high peak intensity.

The amplification process in OPCPA is difference–frequency generation in a nonlinear optical crystal (see Fig. 3).

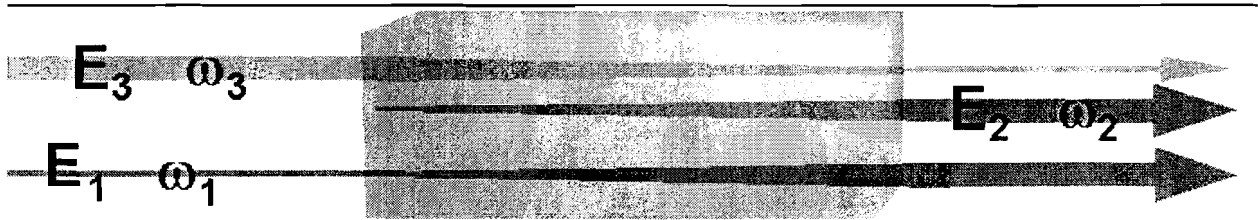


Fig. 3. Difference–frequency generation in a nonlinear optical crystal. Throughout the process, pump beam ( $E_3$ ) weakens, signal beam ( $E_1$ ) gains energy, and idler beam ( $E_2$ ) is generated.

In difference–frequency generation the signal beam gains energy from the pump beam during propagation through the crystal through a nonlinear optical process whereby one photon of the pump beam is converted into one photon of the signal beam and one photon of the idler beam. Following the law of energy conservation, the idler beam that is generated by the process has a frequency given by  $\omega_2 = \omega_3 - \omega_1$  where  $\omega_2$  is the frequency of the idler,  $\omega_3$  is the frequency of the pump, and  $\omega_1$  is the frequency of the signal.

A type I process was modeled, meaning that the pump was an e–wave and the signal and idler were o–waves. An e–wave has an electric field component along the crystal’s optic axis while an o–wave does not. The coupled wave equations that describe the transfer of energy in the crystal are given as <sup>(4)</sup>:

$$\frac{dE_1'}{dz} = -\frac{1}{2} \gamma_1 E_1' - iK E_3' E_2'^* \cdot e^{-i\Delta k z} \quad (1)$$

$$\frac{dE_2'}{dz} = -\frac{1}{2} \gamma_2 E_2' - i(\omega_2/\omega_1) K E_3' E_1'^* \cdot e^{-i\Delta k z} \quad (2)$$

$$\frac{dE_3'}{dz} = -\frac{1}{2} \gamma_3 E_3' - i(\omega_3/\omega_1) K E_1' E_2' \cdot e^{i\Delta k z} \quad (3)$$

$$\text{where } \Delta k = \frac{\omega_3 n_3 - \omega_2 n_2 - \omega_1 n_1}{c} \quad (4)$$

and  $K$  is the nonlinear coupling coefficient. Here  $E_j' = \sqrt{n_j} E_j$ , the  $n_j$  are refractive indices, the  $\gamma_j$  are absorption coefficients for  $j=1-3$ , and the electric fields are given by the real parts of  $E_j e^{(i\omega_j t - ik_j z)}$ , with the  $E_j$  slowly varying functions of  $z$ .  $c$  is the speed of light in meters per second. For the wavelengths used (1054 nm signal and 532 nm pump),  $K=8.38793 \times 10^{-7} \text{ V}^{-1}$  for KDP<sup>(4)</sup> and  $K=6.11270 \times 10^{-6} \text{ V}^{-1}$  for BBO<sup>(5)</sup>.

The refractive indices can be calculated with the use of appropriate Sellmeier equations, which describe the principle refractive indices for e- and o-waves as functions of wavelength ( $n_e$  and  $n_o$ , respectively). The refractive indices for the signal and idler beams ( $n_1$  and  $n_2$ ) are simply the principle refractive indices for o-waves of the appropriate wavelengths. The refractive index of the pump is given as  $n_3 = n_e n_o \cdot (n_e^2 \cos^2 \vartheta + n_o^2 \sin^2 \vartheta)^{-1/2}$  where  $\vartheta$  is the angle between the wave vector of the pump and the optic axis of the crystal. The phase-matching angle  $\vartheta_m$  is by definition the angle at which the phase mismatch  $\Delta k$ , given by Eq. 4, is zero. For BBO the phase-matching angle is calculated as  $\vartheta_m = 22.7856^\circ$ , while for KDP  $\vartheta_m = 41.2097^\circ$ . Energy transfer is most efficient when  $\Delta k = 0$ , so the crystals must be cut at the phase-matching angle.

The coupled wave equations (Eqs. 1-4) were solved numerically using the halfstep-

wholestep process. The program was tested by comparison with the analytical solutions of the coupled wave equations, which assume a constant pump and no absorption:

$$E_1'(z) = E_1'(0) \cosh(gz) \quad (5)$$

$$E_2'(z) = -i \sqrt{\frac{\omega_2}{\omega_1}} \frac{E_3'}{|E_3'|} E_1'(0)^* \sinh(gz) \quad (6)$$

$$g = \sqrt{\frac{\omega_2}{\omega_1}} K |E_3'| \quad (7)$$

### 3. Numerical Model of OPCPA

The numerical model was used to investigate parametric amplification in crystals of KDP and BBO for use in a petawatt laser system. However, the model is very flexible and can easily accommodate any crystal type given appropriate Sellmeier equations and nonlinear coupling constants, which can be found in Ref. 5. Any wavelengths of incident light for which the Sellmeier equations remain valid can be modeled, but typically a 532 nm pump and a signal with a central wavelength of 1054 nm were used. Currently, pumps with flat-top and Gaussian temporal shapes have been modeled; however, the pump's temporal shape can easily be modified given the equation of a theoretical shape or data on an experimentally measured shape. Any number of crystal stages can be modeled by adding length and crystal type specifications for additional stages (it is assumed that the aperture is large enough to accommodate the beam spot size). The beam spot size is also taken into account when determining the intensity (and therefore electric field values) of the pump and signal, although the beams are assumed to have a flat-top spatial profile. The phase-matching angle,  $\vartheta_m$ , can be calculated for any crystal type and wavelength.

To model the temporal stretching of the pulse, the Fourier transform of the input pulse was taken, and a stretched pulse was created by assigning a temporal delay  $\Delta \tau$  to each spectral mode  $\Delta \omega$  using <sup>(6)</sup>:

$$\Delta \tau = \frac{-1}{\mu} \Delta \omega \quad . \quad (8)$$

Here  $\mu = \frac{\omega_0^3 d^2 \{1 - [(2\pi c / \omega_0 d) - \sin \gamma]^2\}}{4\pi^2 c b}$  where  $\omega_0$  is the central frequency of the incident light,  $d$  is the distance between adjacent grooves of the gratings (675 nm),  $\gamma$  is the angle between the incident beam and the normal of the grating (48°), and  $b$  is the distance between the two gratings (13 m). Values for  $\gamma$ ,  $b$ , and  $d$  were chosen to lead to a stretched pulse width which meets the design requirement of approximately 5 ns. The inclusion of imaging lenses between the expansion gratings produces a virtual image of the first grating, causing the effective distance between the gratings ( $b$ ) to be negative in the expansion grating pair. This gives  $\mu^{-1} = \pm 1.77 \times 10^{-22} s^2$ , depending on which grating pair is under consideration.

This allowed each spectral mode of the transformed pulse to be uniquely mapped to one temporal point of the pump beam through the scaling factor  $-\mu^{-1}$ . The electric field values of the transformed pulse were then multiplied by a normalization factor such that the spectral pulse contained the correct energy. A graph of stretched (chirped) pulse intensity and frequency vs. time can be found in Fig. 4.

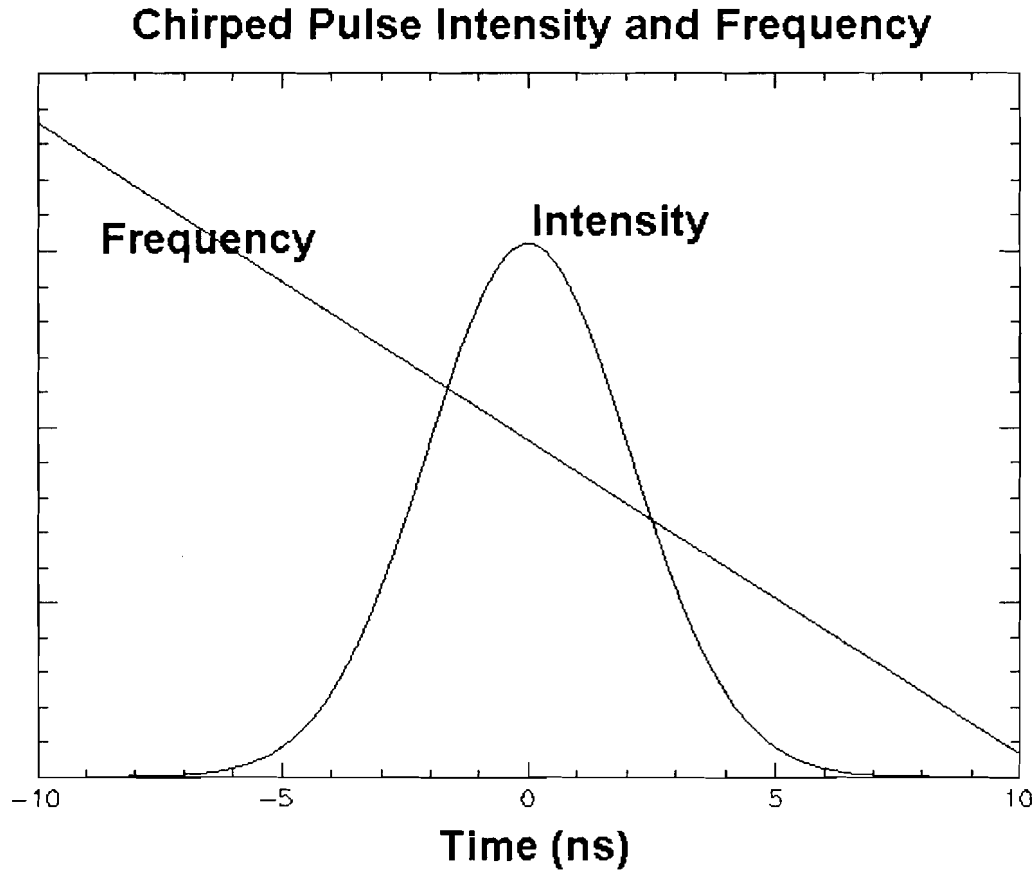


Fig. 4. Graph of intensity and frequency vs. time for a temporally stretched (chirped) pulse. The plot of intensity as a function of time is a perfect Gaussian while the frequency varies linearly with time.

---

The pulse was then propagated through the crystal stages, using (Eq. 8) to determine which frequencies of the signal should interact with various temporal points of the pump. After propagation through the crystal stages the inverse transform was taken, resulting in a recompressed pulse with a short temporal width.

The results obtained from the numerical model matched the results obtained from the analytical solutions (Eqs. 5–7) of the coupled wave equations in the small–signal regime, after which the models diverged due to pump depletion (see Fig. 5). Therefore the numerical model is needed to design a system which does not operate in the small–signal regime.

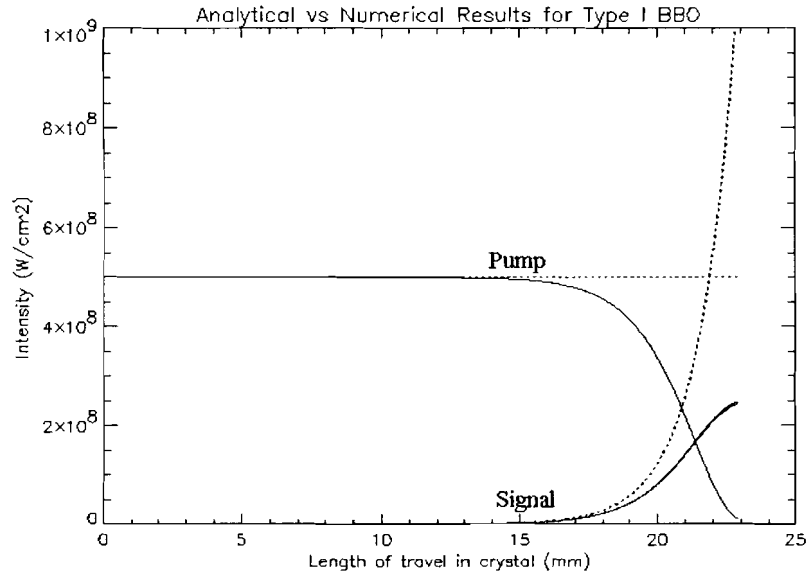


Fig. 5. Plot of intensity vs. length of travel in BBO crystal for analytical results (dotted line) and numerical results (solid line) shows that the models agree in the small-signal regime, after which they diverge due to pump depletion.

---

## 4. Design for proof-of-principle experiment

The numerical model was used to investigate designs for a petawatt laser front end leading to a high-quality (i.e., short) recompressed front end output pulse. This design was for proof-of-principle, and an experiment is planned to compress the OPCPA output without injecting it into the glass amplifier chain to determine if the system behaves as predicted and to see if a short recompressed pulse can be obtained.

The goals of the design were to amplify a 100 fs pulse with 1 nJ of energy to at least 250 mJ using 3 J or less of pump energy per crystal stage, with a relatively short recompressed pulse and a pulse contrast of about  $10^5$  or  $10^6$ . High pulse contrast is desirable for target illumination – lower pulse contrast means a higher prepulse level, which may perturb the target prior to arrival of the main pulse and detrimentally affect the fusion process. To obtain a short recompressed

pulse with a high pulse contrast level, a spectral shape which is very close to a Gaussian is required, and since the input pulse is a Gaussian in time (and therefore frequency) the required amplification must be performed with as little modification to the spectrum as possible.

A single-crystal example can be used to illustrate the basic design considerations. A flat-top pump, which can be approximated by a Gaussian pump of a large width (a 32 ns pump was used in the first two stages), is required to preserve the spectrum in the small-signal regime\*. A flat-top pump preserves the signal spectrum in the small-signal regime because the analytical solutions (Eqs. 5–7) remain valid, and if the intensity of the pump does not vary with time then there will be an equal multiplication of all temporal points of the signal electric field, leading to a flat signal gain profile. However, due to the fact that energy is transferred more quickly from the pump to the signal at the center of the pulse, pump depletion affects the pump to a greater extent in the center than in the temporal wings. This causes distortions to the spectrum of the signal to be present if significant depletion occurs, which leads to lower pulse contrast after recompression (see Fig 6). The goal of the design is to extract the greatest amount of pump energy possible without compromising the recompressed pulse contrast – for the pump and signal energies used to generate Fig. 6, a 22 mm crystal results in high gain with moderate distortions to pulse shape, while a 25 mm crystal results in even higher gain, but at the cost of large distortions to the spectrum and therefore the recompressed pulse shape.

The trade-off between recompressed pulse contrast and efficiency was the primary consideration in the design of the proof-of-principle system. Using the model, a four-stage system was designed (relevant design parameters may be found in Table 1).

---

\* Slight distortions of the spectrum occur due to phase mismatch even with a flat-top pump

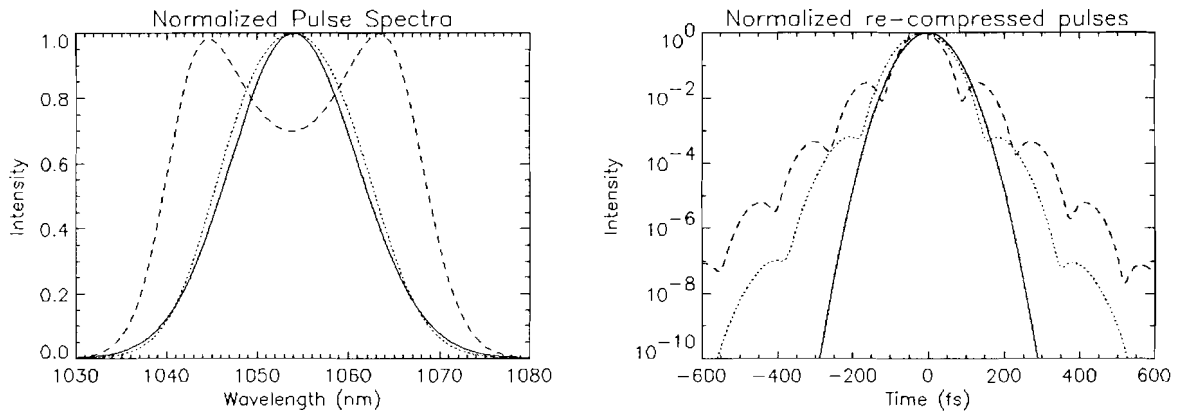


Fig. 6. Normalized pulse spectra (left) and recompressed pulse intensity (right) show how spectral shape affects recompression. Shown are an initial pulse (solid line), a pulse after 22mm of BBO crystal (dotted line), and a pulse after 25mm of BBO crystal (dashed line). Pump depletion modifies the spectral characteristics of the pulse cumulatively, resulting in an increasingly poor recompressed signal with increasing pump depletion.

Table 1. Values used in the different crystal stages for the proof-of-principle design

	Stage 1	Stage 2	Stage 3	Stage 4
Crystal (BBO)	4x4x14.5mm	5x5x9.5mm	7x7x4.5mm	10x10x4.2mm
Sig/Pump Spot Size	0.4mm/1.2mm	2.8mm/3.3mm	5.6mm/5.9mm	8.0mm/8.2mm
Pump	115mJ, 32ns	780mJ, 32ns	888mJ, 8ns	829mJ, 4.5ns
Pump max Intensity	237 MW/cm <sup>2</sup>	213 MW/cm <sup>2</sup>	314 MW/cm <sup>2</sup>	264 MW/cm <sup>2</sup>
Input / Output	1nJ / 22.4μJ	22.4μJ / 6.50mJ	6.50mJ / 70.7mJ	70.7mJ, 300mJ
Gain	22400	290.2	10.9	4.4
Efficiency	0.02%	0.83%	7.22%	27.63%

This system uses a total of 2.61 J of pump energy to amplify a 1 nJ, 100 fs pulse to 300 mJ. The design goal of 250 mJ was intentionally exceeded to compensate for secondary gain-reducing effects which are not yet taken into account. All four stages were modeled using BBO as a gain medium due to its large nonlinear coupling constant. The maximum pump intensity in any crystal stage was 314 MW/cm<sup>2</sup>, thus the damage threshold of BBO for 532 nm light (500–1000 MW/cm<sup>2</sup> <sup>(7)</sup>) was not exceeded. The final recompressed pulse had a pulse width of 203 fs

and a pulse contrast of  $\sim 10^5$ . The pulse spectra throughout the crystal stages and the final recompressed pulse are shown in Fig. 7.

---

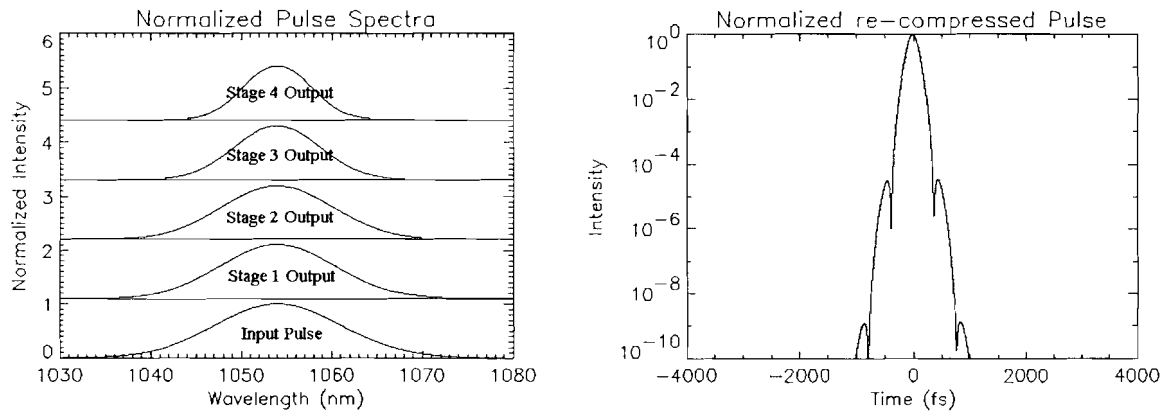


Fig. 7. Normalized pulse spectra (left) and recompressed pulse intensity (right) for proof-of-principle design. Recompressed pulse width is 203 fs, energy is 300 mJ.

---

It was determined that four stages were needed for this design, as it was possible to meet the output energy requirement using three stages, but only at the cost of recompressed pulse contrast. After approximate crystal lengths and pump energies were determined, each stage was optimized individually, beginning with the first stage. In optimizing the system, stages were added one at a time so that their effect on the recompressed pulse could be easily seen. In the first two stages the spectral pulse shape was preserved to the greatest extent possible by operating far from pump depletion, which led to an almost perfect recompressed pulse at the output of the first two stages. A very wide pump (32 ns) was used for both of these stages to preserve signal bandwidth to the greatest extent possible, which, combined with operating far from depletion, led to very low efficiency. In the final stages much shorter pump pulses were used both to increase efficiency (since less energy is wasted in the wings where there is almost no signal to amplify) and to help maintain the Gaussian shape of the spectrum. Much shorter crystals were used in these stages because the higher initial signal intensities led to a much more rapid transfer of energy. Depletion in these stages led to distortions of the pulse spectrum and therefore higher

levels of prepulse. All pump spot sizes are larger than the signal spot sizes to compensate for walk-off, which will be discussed later. The pump and signal beam spot sizes are increased between crystal stages to lower intensity and therefore potential for damage to the gain medium.

## 5. Design for petawatt system

For the petawatt system, a design was needed to produce a flat-top spectrum output pulse for injection into the Nd:glass amplifier chain. This is desirable because gain narrowing in the amplifier chain can reduce the pulse pedestal, increasing pulse contrast<sup>(8)</sup>. The glass amplifiers were modeled with a transfer function which assumes a small-signal gain of about 2200\*. The transfer function used was a Gaussian centered at 1052.57 nm with a FWHM of 5.2 nm. Using this design, a front end output of 300 mJ was obtained in three crystal stages using a total pump energy of 1.90 J. See Table 2 for relevant design parameters.

Table 2. Values used in different stages for the petawatt system design

	Stage 1	Stage 2	Stage 3
Crystal	4x4x16 mm BBO	5x5x15 mm BBO	10x10x8 mm BBO
Sig/Pump Spot Size	0.4 mm / 1.3 mm	2.8 mm / 3.6 mm	8 mm / 8.4 mm
Pump	49.0 mJ, 16 ns	333 mJ, 16 ns	1.52 J, 16 ns
Pump Max Intensity	203 MW/cm <sup>2</sup>	152 MW/cm <sup>2</sup>	128 MW/cm <sup>2</sup>
Input / Output	1 nJ / 23.1 μJ	23.1 μJ / 30.6 mJ	30.6 mJ, 300 mJ
Gain	23100	1324.7	9.8
Efficiency	0.05%	9.19%	17.77%

The final recompressed pulse width after the glass amplifier chain was 798 fs. This is much greater than the 203 fs obtained from the proof-of-principle design, but still well within the design goal of 1 ps. The recompressed pulse is much longer due to gain narrowing in the glass amplifier chain. Flat-spectrum pulses are more easily obtained at the output of OPA than

---

\* Pulse shape was modeled using the transfer function, but energy was normalized, producing a gain of 1

are Gaussian-spectrum pulses because pump depletion lowers gain in the center of the pulse before lowering gain in the wings, essentially flattening out the spectrum. The pulse spectra throughout the crystal stages and the final recompressed pulse are shown in Fig. 8. The recompressed pulse contrast was higher than  $10^{10}$  at  $\pm 2$  ps.

---

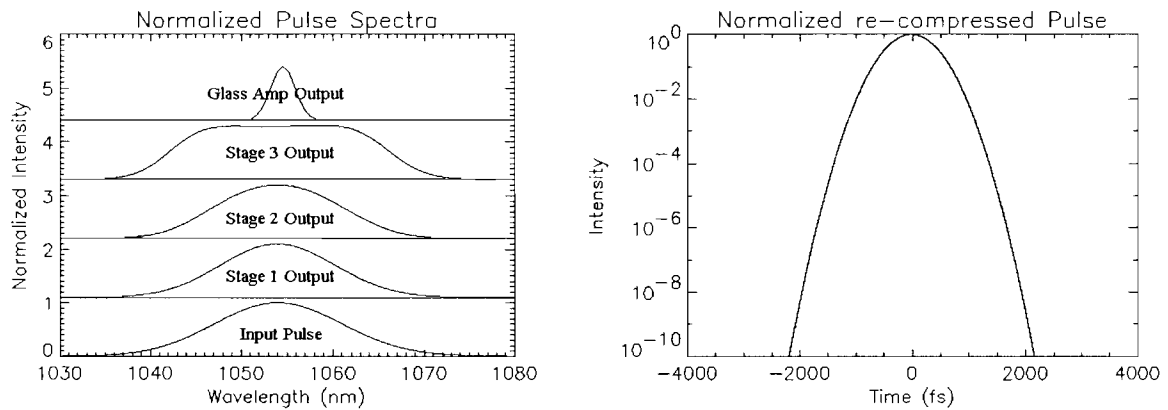


Fig. 8. Normalized pulse spectra (left) and recompressed pulse intensity (right) for actual system design. Recompressed pulse width is 798 fs, well within the design goal of 1 ps. Final output energy is 300 mJ.

---

Table 3 contains a comparison of the two designs. In the actual system design three crystal stages were required instead of four because the pumps can be run farther into depletion (the effects associated with pump depletion in the proof-of-principle design are now actually desirable for this design). This requires longer crystals but less pump energy, allowing for higher overall efficiency (defined as the total increase in signal energy over the total pump energy used). Preservation of bandwidth was a secondary concern in the actual system design because injection into the Nd:glass amplifiers will reduce bandwidth anyway. As in the proof-of-principle design, stages were added and optimized individually, and the signal and pump beam spot sizes are expanded between crystal stages.

Table 3. Comparison of proof-of-principle and actual system designs

	Proof-of-principal design	Actual system design
Number of rystals	4	3
Total crystal length	32.7 mm	39 mm
Pulse width (Input / Output)	100 fs / 202 fs	100 fs / 798fs
Pump width	32–4.5 ns	16 ns
Total pump energy used	2.61 J	1.90 J
Signal energy (Input / Output)	1 nJ / 300 mJ	1 nJ / 300 mJ*
Overall efficiency	11.50%	15.79%

\* Energy of output pulse before glass amplifier chain

The capability to run the actual system design farther into depletion led to increased efficiency due to the fact that much less pump energy had to be used since more of it was extracted. The output pulse width is much larger for the actual system design due to loss of bandwidth in the Nd:glass amplifier chain, but the design goal of less than a picosecond was still met.

## 6. Future work

In the future the model will be improved to include several other capabilities. The ability to model the spatial shapes of the beams will be added, as well as the walk-off (lateral displacement) of the pump. Walk-off in an anisotropic crystal occurs because the Poynting vector of the e-wave (direction of energy flow) is not the same as the k-vector (the vector normal to the wavefront). This affects only the pump and not the signal and idler because only the pump is an e-wave (the signal and idler beams are o-waves). The walk-off angle in BBO is ~3 degrees, which has been taken into account in only a limited way in that the pump spot sizes are larger than the beam spot sizes to maintain overlap throughout the crystal. However, this effect is more prevalent in the first stage because the spot size is smaller and walk-off is greater due to the longer path through the crystal.

The capability to model a non-collinear angle between the pump and signal beams will be included. Reasons for using a non-collinear angle include being able to separate the signal and idler beams after propagation through the crystal, compensating for walk-off, and larger gain bandwidth <sup>(9)</sup>.

The B-Integral, which refers to the accumulated nonlinear phase (self-phase modulation) and is defined as

$$B = \frac{2\pi}{\lambda} \int n_2 I dl$$

will also be taken into account. Here  $n_2$  is the nonlinear refractive index,  $I$  is the intensity of the beam, and  $dl$  is the incremental crystal length. The phase of the incoming light is not changed equally across the whole beam, but changes in part as a function of intensity. This effect can occur across both time and space because intensity varies across both time and space.

Therefore the temporal effects of the B-Integral could be included in the current model without considering spatial dependence. Nonuniform phase accumulation across the beam can cause a self-focusing effect which produces areas of differing intensity, possibly leading to damaged optics. The effect of accumulated nonlinear phase is expected to be small, however, due to the short path through the gain medium. In work done by Jovanovic <sup>(10)</sup> using similar crystal lengths, intensities, and signal energy as the two designs reported here, nonlinear phase accumulation was 0.04 radians and had a negligible effect.

The effect of group velocity difference between the three beams (caused by their different wavelengths and polarizations) may also eventually be considered. However, its effect is expected to be small.

The numerical model will also be used to investigate the stability of the system (to determine the range of of output pulse energy fluctuations for a given range of pump energy

fluctuations) and the sensitivity of the system to angular detuning (to establish the tuning tolerance).

## 7. Conclusions

A numerical model of OPCPA was developed and used to design two petawatt laser front ends, one which leads to a short recompressed pulse for a proof-of-principle experiment and one which leads to spectral characteristics desirable for injection into the main Nd:glass amplifier chain of the petawatt laser being designed at the University of Rochester LLE. Both designs amplified the pulse to 300 mJ, exceeding the design goal of 250 mJ. The width of the recompressed pulse from the glass amplifier chain (798 fs) was well within the design goal (1 ps). Optimized versions of these designs including secondary effects such as walk-off and non-collinear propagation will be used for the design of the petawatt laser system which will be incorporated into the OMEGA laser system as an implementation of the fast-ignitor concept. A fast ignitor has the potential to increase the efficiency of ICF, bringing nuclear fusion a step closer to use as an effective energy source.

## Acknowledgments

I would like to thank Dr. Stephen Craxton for giving me the opportunity to participate in the High School Summer Research program at the University of Rochester Laboratory for Laser Energetics, and for all the work he spent making the program so successful. I would also like to thank my advisor, Mark Guardalben, who spent many hours teaching me the concepts behind OPCPA; his assistance has been invaluable in completing this project and without it this project would not have been possible.

## References

- (1) – Michael H. Key, "Fast Track to Fusion Energy," *Nature* **412**, 775–776 (2001).
- (2) – L. Waxer and J. Kelly, "Conceptual Fast–Ignitor System Design", presentation given at LLE April 4, 2001.
- (3) – D. Strickland and G. Mourou, *Opt. Comm.*, 56 (1985) 219.
- (4) – R. S. Craxton, "High Efficiency Frequency Tripling Schemes for Higher–Power Nd:Glass Lasers," *IEEE Journal of Quantum Electronics* **QE–17 No. 9**, 1771–1782 (1981).
- (5) – V. G. Dmitriev, G. G. Gurzadyan, and D. N. Nikogosyan. Handbook of Nonlinear Optical Crystals. Berlin Heidelberg, Germany: Springer–Verlag, 1991, 1997, 1999.
- (6) – Edmond B. Treacy, "Optical Pulse Compression with Diffraction Gratings," *IEEE Journal of Quantum Electronics* **QE–5 No. 9**, 454–458 (1969).
- (7) – Igor Jovanovic, Brian J. Comaskey, Chris A. Ebbers, Randal A. Bonner, Deanna M. Pennington, Edward C. Morse, "Optical Parametric Chirped Pulse Amplifier as an Alternative to Ti:sapphire Regenerative Amplifiers," to be published.
- (8) – M.D. Perry, F.G. Patterson, and J Weston, "Spectral shaping in chirped–pulse amplification," *Opt. Lett.* 15, 381 (1990).
- (9) – Pavel Matousek, Bedrich Rus, and Ian N. Ross, "Design of a Multi–Petawatt Optical Parametric Chirped Pulse Amplifier for the Iodine Laser ASTERIX IV," *IEEE Journal of Quantum Electronics* Vol 32 No 2, 158–162 (2000).
- (10) –I Jovanovic, B J Comaskey, C A Ebbers, R A Bonner, D M Pennington, "Replacing Ti:sapphire regenerative amplifiers with an optical parametric chirped pulse amplifier," CPD8–1, CLEO 2001 Post–deadline conference, May 6–11, 2001, Baltimore Convention Center.

# **Computational Modeling of Physical Properties in Liquid Crystalline Polymer Systems**

Kevin D. Monajati

Advisor: Kenneth Marshall

Summer High School Research Program 2001

Laboratory for Laser Energetics

University of Rochester

## **Abstract:**

New software is available to aid in the modeling of liquid crystalline polymer systems. Oligomers with nine repeat units can be modeled successfully using MOPAC 2000. Programs have been written to aid in solving for the birefringence and dielectric anisotropy of the molecule, thus allowing all numerical analysis to take place on the UNIX platform. This numerical analysis will allow for a reduction in laboratory investigations with polymer synthesis.

## 1. Introduction

Between solid and liquid, there is a state of matter known as a liquid crystal. The properties exhibited by the molecules are very different from either solids or liquids. Because of the rod-like shape of these molecules, the values of their dielectric constants and refractive indices depends on their orientation to an electromagnetic field or light source, respectively (Fig. 1) . The maximum and minimum values of these two properties are found to be parallel and perpendicular to the molecular axis. The dielectric anisotropy is the difference between the maximum and minimum dielectric constants for the molecule, and the birefringence is the difference between the maximum and minimum refractive indices. These properties provide for many applications of liquid crystals in optical devices.

Liquid crystalline systems can be either main chain polymers or side chain polymers. Main chain polymers result when the mesogens are aligned head to tail in the polymer backbone, with spacers between each molecule normally made up of several alkyl groups. Side chain polymers are polymers attached to a backbone of made up of combinations of carbon, silicon and oxygen atoms or other repeating groups. Spacer groups, made up of chains of carbon atoms, are at the head of each mesogen, which attaches to the side of the backbone. Due to their structure, polymeric liquid crystals have advantages over single mesogens (Fig. 2). They are much more robust, and able to form freestanding films. However, because of the protrusion of the mesogens from the backbone, polymeric systems are much more viscous and thus have slower electro-optic response times.

The measurement of the properties of liquid crystals in the laboratory environment can be time-consuming and often inaccurate. Computer modeling has come to the forefront of the scientific world recently because (1) of its remarkable predictive ability, and (2) graphically

assembling molecules and evaluating their structure/property relationships computationally is much easier and less time-consuming than synthesizing compounds with every possible structural permutation and combination in the lab. With the advent of modern, high-speed, multi-processor machines and advanced software, calculations that previously took months can now be done in only a few hours. When compared to the time it may take to synthesize, purify and characterize a single sample of a new liquid crystal, the advantage is obvious.

## 2. Method

Candidate mesogens were first constructed graphically using Wavefunction, Inc.'s Spartan v.5.1.3, a computational chemistry software package running on a DEC Alpha Server under the UNIX operating system (Fig. 3). Merck energy minimization was performed before optimizing the geometry at 0° K using the AM1 semiempirical method and parameter set. Mesogenic groups were constructed and duplicated, and then attached to a carbon-carbon polymer backbone structure. The output file generated by Spartan was graphically viewed using the XMO visualizer (Fujitsu Ltd, Fig. 4), the polymer was checked for any possible errors, and any of these errors were corrected using Spartan if required. The corrected output file was imported into MOPAC 2000 (Schroedinger, Inc) for the polarizability calculations after viewing with XMO, and the resulting data was input into a C++ program that was used to calculate the dielectric anisotropy and birefringence of the candidate polymer.

### 2.1. Using MOPAC 2000 and XMO

MOPAC 2000 is designed to efficiently compute and analyze macromolecular structures in a short period of time. However, the program is entirely text-based and requires the use of external data files that cannot be edited from within the program. Hence the XMO viewer is

used to view the polymers and check for overall structural correctness before importing into MOPAC. XMO uses MOPAC 2000's algorithm for detecting bonding sites, but displays the molecule graphically, making it easy for the user to do error-checking. In order for MOPAC 2000 to understand what the user is requesting, a line of keywords is used at the beginning of a text file.

## 2.2. Using *deltaEdeltaN.cpp*

DeltaEdeltaN is a new C++ program developed during this project (K. Monajati) that allows the user to take data directly from either Spartan or MOPAC output files and enter it into the program. The C++ code does all of the calculations for the user, returning the values for the dielectric anisotropy and birefringence of the molecule. A sample output screen from the program can be found in Fig. 5.

### 2.3.1 Calculation of $\Delta\epsilon$

The dielectric anisotropy is calculated using the Maier – Meier theory, given by<sup>1</sup>

$$\Delta\epsilon = \frac{NFh}{\epsilon_0} \left( \Delta\alpha - \frac{F\mu^2}{3k_bT} (1 - 3\cos\beta) \right)$$

where

$$F = \frac{1}{(1 - f\alpha)}$$

$$f = \frac{\epsilon - 1}{2\pi\epsilon_0 a^3 (2\epsilon + 1)}$$

$$h = \frac{3\epsilon}{2\epsilon + 1}$$

and  $\epsilon_0$  is the permittivity of a vacuum,  $k_b$  is Boltzmann's constant, N is the molecular density, T is the absolute temperature,  $a$  is the radius of the spherical cavity surrounding the molecule,  $\mu$  is the magnitude of the dipole moment., and  $\beta$  is the angle made between the

director and the dipole moment. The values of N, and T, were taken to be 1000 kg/m<sup>3</sup> and 293° K, respectively. The static permittivity,  $\epsilon$ , is derived algebraically from the Onsager theorem<sup>1</sup>,

$$\epsilon - 1 = \frac{NFh}{\epsilon_0} \left( \alpha + \frac{F\mu^2}{3k_bT} \right)$$

where  $\alpha$  is the mean polarizability.

### 2.3.2 Calculation of $\Delta n$

The birefringence,  $\Delta n = n_e - n_o$ , was calculated from values from the Vuks equations<sup>1</sup>

$$\frac{n_e^2 - 1}{n^2 + 2} = \frac{N}{3\epsilon_0} \left( \alpha + \frac{2\Delta\alpha S}{3} \right)$$

$$\frac{n_o^2 - 1}{n^2 + 2} = \frac{N}{3\epsilon_0} \left( \alpha - \frac{\Delta\alpha S}{3} \right)$$

where S is the order parameter of the liquid crystal compounds (a value of 0.7 was assumed for all calculations). The Lorentz – Lorenz equation

$$\alpha = \frac{3\epsilon_0(\epsilon - 1)}{N(2\epsilon + 1)}$$

gives values for  $\epsilon$  at optical frequencies, where  $\epsilon = n^2$  as above.<sup>2</sup>

## 3. Modeling of Polymeric Systems

A total of 24 side-chain polymers were modeled to determine the properties of polymer mesogens with high  $\Delta\epsilon$ . However, only 20 models were successful, because MOPAC 2000 was unable to recognize the electronic configuration of nitrogen atom in the carbazole group (Fig 6) due to its aromatic structure. Other molecules that were modeled were made of three carbon spacers followed by either a benzene, naphthalene, or anthracene structure, followed by an ether group, and then another cyclic structure. This system allowed for a small  $\beta$ , giving the molecule a larger dipole. Although all of the 20 systems have been computationally modeled by

MOPAC 2000, data analysis and final calculations of  $\Delta\epsilon$  and  $\Delta n$  for these systems using deltaEdeltaN.cpp remains to be completed.

#### **4. Summary**

The use of computational modeling for prediction and analysis of polymeric systems is a valid method that can reduce laboratory time and increase accuracy. Experimental systems analyzed showed interesting trends, although final analysis still needs to be completed.

Although MOPAC 2000 shows great potential for prediction of structure/property relationships in macromolecules, great care must be taken to insure that the structures created represent valid compounds. The availability of XMO to visually error-check structures prior to processing in MOPAC 2000 is a significant improvement, and will be a great tool in the further investigation of larger liquid crystalline systems.

#### **5. Acknowledgements**

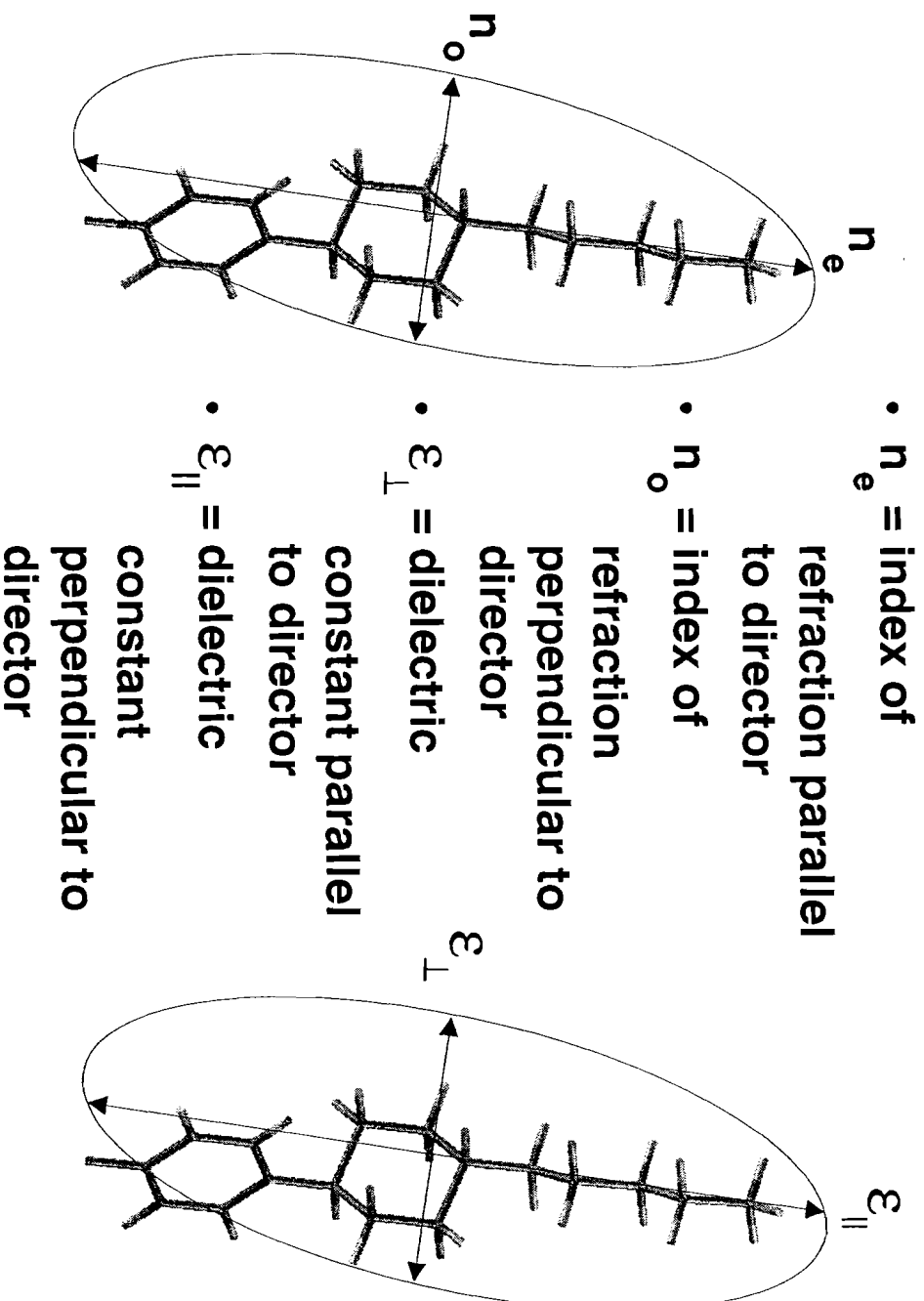
I would like to extend my sincerest thanks to Dr. R. Stephen Craxton for providing my fellow students and I the opportunity to conduct research over the summer. I would also like to thank my project advisor, Mr. Kenneth Marshall, for his help and guidance throughout my time at LLE. My thanks also go out to M. Gao, C. Piro, M. Fiedler, and other students who worked in the IAL with me. Finally, I would like to acknowledge L. Stein for his helpfulness in working me through the intricacies of the UNIX system.

References:

- 
1. M. Klasen, et al., "Calculation of Optical and Dielectric Anisotropy of Nematic Liquid Crystals." *Jpn. J. Appl. Phys.*, 37, 945 (1998).
  2. J. VanLare, "Predicting the Optical and Dielectric Anisotropy of Liquid Crystalline Systems," 1999 Summer Research Program for High School Juniors at the University of Rochester's Laboratory for Laser Energetics, Laboratory for Laser Energetics Report No. 311, NTIS document No. DOE/SF/19460-338 (1999).

Figure 1

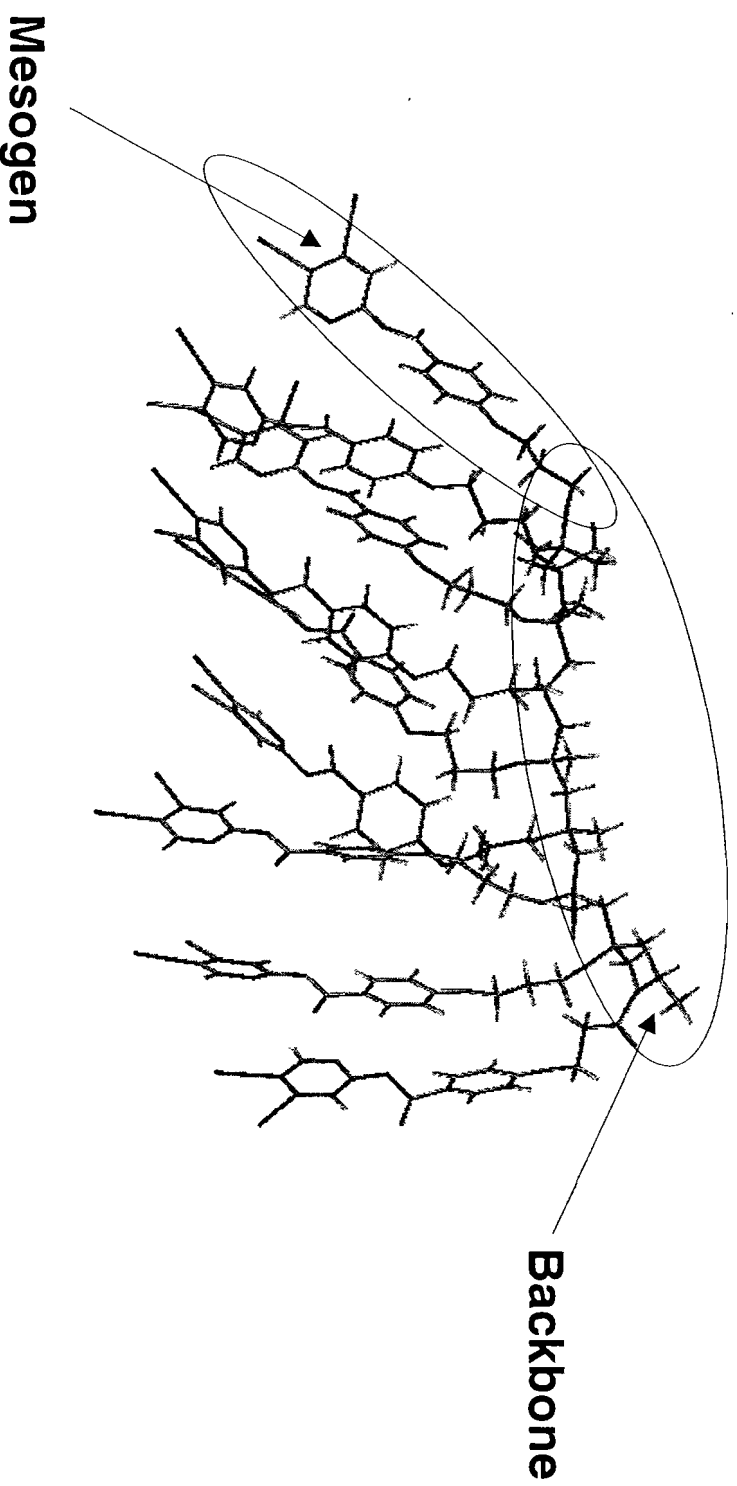
# LC mesogens have two dielectric constants and two indices of refraction



- Maximizing  $\Delta n$  and  $\Delta \epsilon$  is the aim of modeling LC polymers

Figure 2

## Liquid crystal (LC) polymers have basic structural similarities



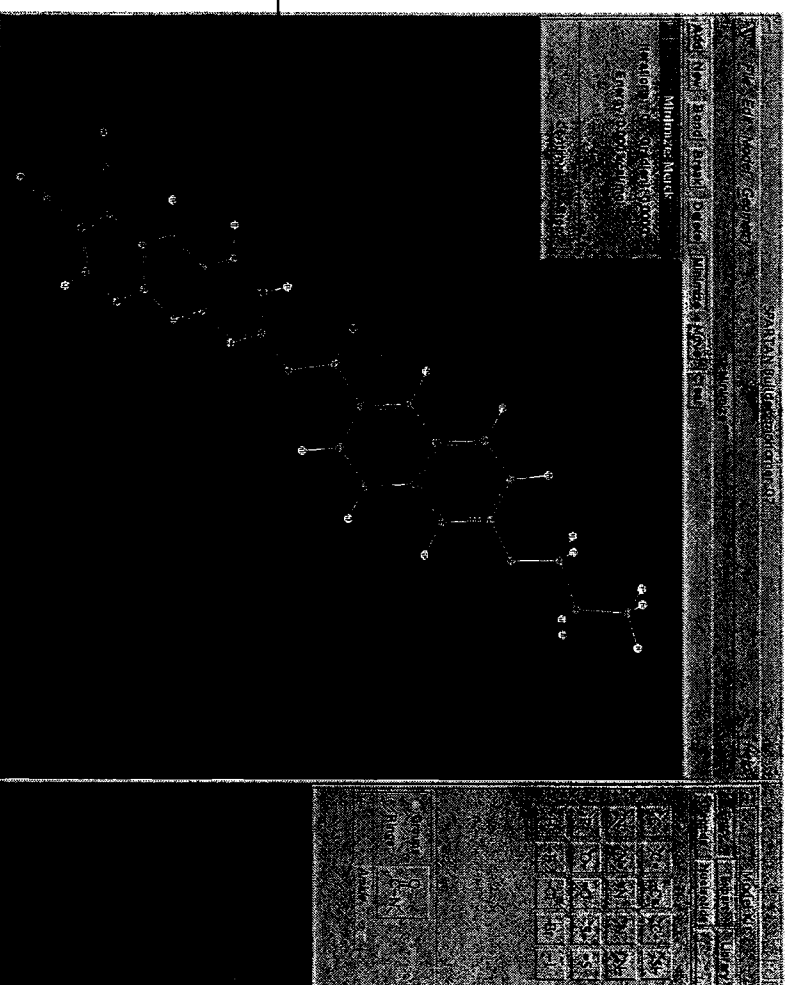
- Liquid crystal polymers are more environmentally robust than mesogens
- Larger molecules are more viscous, making alignment harder

Figure 3

# Spartan v.5.1.3<sup>1</sup> is used to graphically build initial mesogens



- A mesogen is constructed using Spartan's graphical interface
- Energy is optimized using Merck MMFF94 force field minimization
- Mesogens are repeated, and bonded to a common backbone structure
- The oligomer is then minimized again to prevent misplacement of atoms
- The file is exported and formatted



<sup>1</sup> Spartan. v.5.1.3.  
Wavefunction, Incorporated:  
Irvine, CA. 1993.

Figure 4

**XMO<sup>1</sup> is used to visually check the oligomer before being sent to MOPAC 2000<sup>2</sup>**



- Polymer is checked for mistakes in data file, including misbonded, incorrect, or missing atoms
- Once file is inspected, it is read by MOPAC 2000, and a data file is created by the program using the AM1 semiempirical method
- From this file, values are gathered to be used for determination of the physical properties of the molecule

---

<sup>1</sup> XMO. v.4.0. Fujitsu, Limited: Nakase, Japan. 2000.

<sup>2</sup> MOPAC 2000. Schrödinger, Incorporated: Nakase, Japan. 2000.

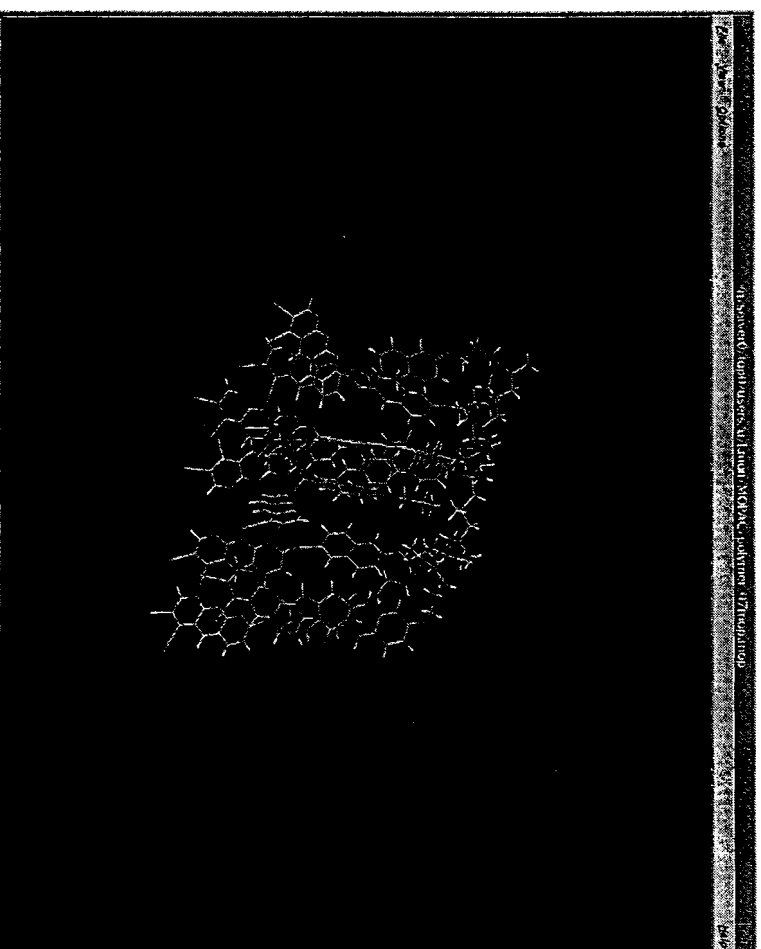


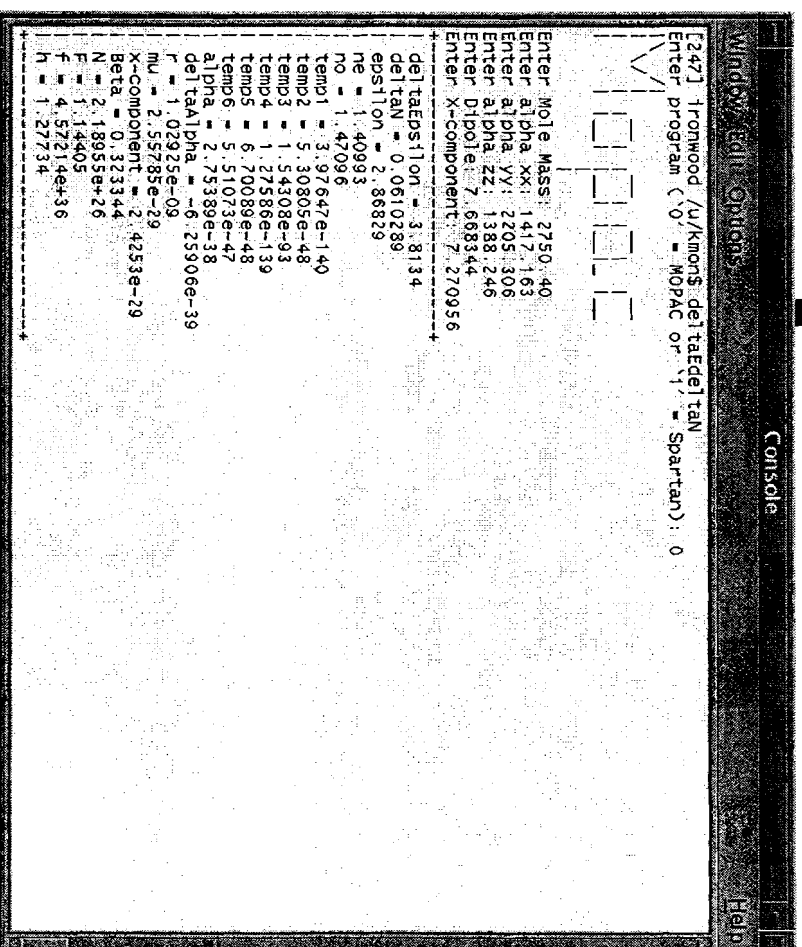
Figure 5

"deltaE/deltaN" is used to calculate the dielectric anisotropy and birefringence of the oligomer

- Using data such as molecular mass, dipole moment, and anisotropy of molecular polarizability, deltaE/deltaN analytically solves for the following values using the Maier-Meier theory:

$$\left[ \Delta \epsilon = \frac{NF^2h}{\epsilon_0} \left( \Delta \alpha - \frac{F\mu^2}{2k_b T} (1 - \cos^2 \beta) \right) S \right]$$

- $\Delta \epsilon$
- $n_e$
- $n_o$
- $\Delta n$
- $\epsilon$  – the static permittivity of the molecule
- $\beta$  – the angle between the director and the dipole



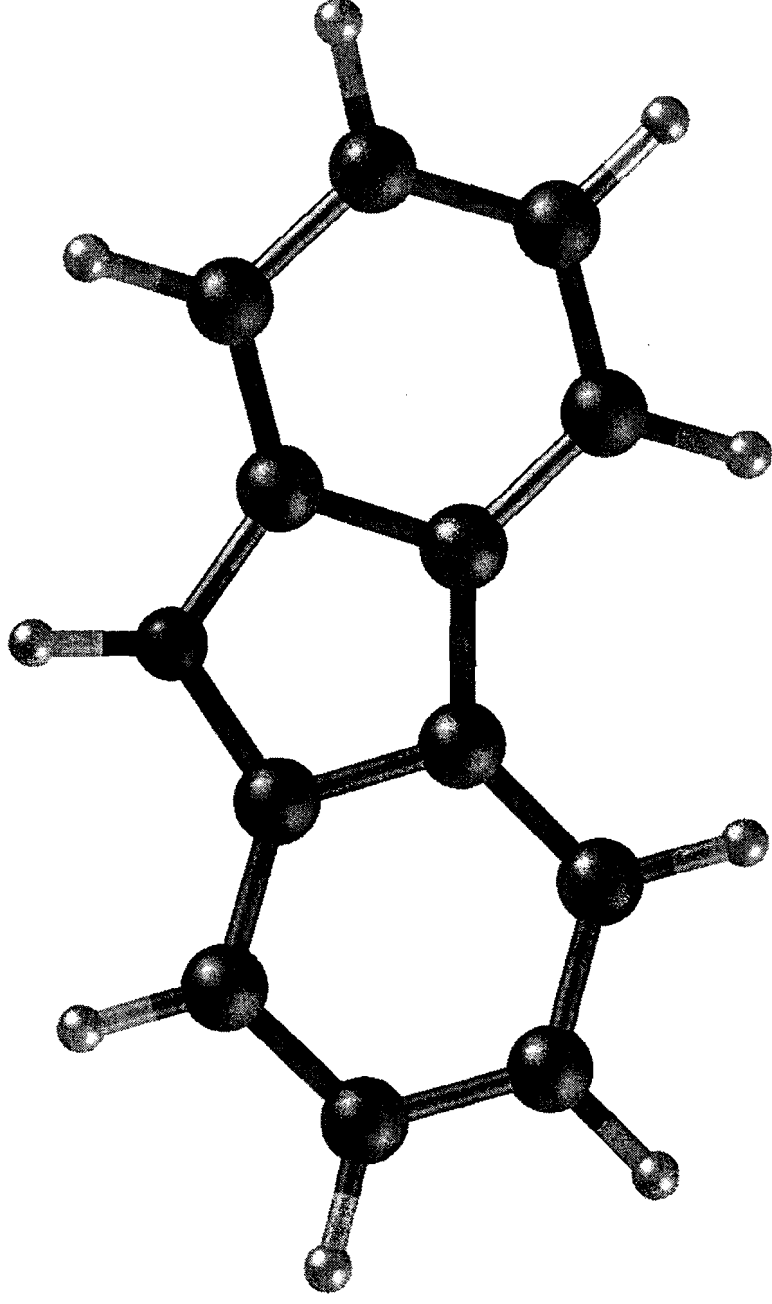
```

[247] Ironwood (/u/Kromos/deltaE/deltaN)
Enter program ('0' = MOPAC or '1' = Spartan): 0
Enter Mole Mass: 2750.40
Enter alpha xx: 1417.163
Enter alpha yy: 2205.306
Enter alpha zz: 1388.246
Enter Dipole: 7.668344
Enter X-component: 7.270956
-----
deltaEpsilon = 3.8134
deltaTan = 0.0610289
eps11on = 2.86829
no = 1.42096
temp1 = 3.97647e-140
temp2 = 5.30805e-48
temp3 = 1.54308e-93
temp4 = 1.27586e-139
temp5 = 6.70089e-48
temp6 = 5.51073e-47
alpha = 2.75389e-38
deltaAlpha = -6.25906e-39
mu = 1.02925e-09
mu = 2.55785e-29
X-component = 2.4253e-29
Beta = 0.323344
N = 2.18955e+26
F = 3.144405
h = 4.57214e+36
h = 1.27734
  
```

Figure 6

## Carbazole heterocyclic functional group was unable to be recognized by MOPAC2000

- Due to aromatic heterocyclic ring structure, MOPAC was consistently unable to analyze the configuration of the nitrogen atom



# Modeling the LCPDI with Refraction and Diffraction

**Christopher J. Piro**

Advisor: Dr. R. S. Craxton

**Summer High School Research Program 2001**

Laboratory for Laser Energetics  
University of Rochester

## **Abstract**

A liquid crystal point diffraction interferometer (LCPDI) computer model was extended to calculate spreading due to diffraction as well as refraction. The software can also model cells with elliptical beads. This more general software allows the rapid investigation of LCPDIs without fabrication, which presently is neither quick, accurate, nor easy. By isolating the parameters and materials needed to make a useful device, it is hoped to develop an optimal interferometer to replace larger and more expensive commercial interferometers.

# 1 Introduction

Inertial confinement fusion (ICF) is a technology with the potential to power the world in the years to come. Fusion is desirable for powering electrical generators because fusion fuel is derived from hydrogen, one of the most abundant elements. Energy is liberated in fusion by joining two light atoms or nuclei into a single, heavier nucleus. The resultant nucleus is lighter than its components. The “missing mass” is converted to energy – explosively in nuclear weapons and slowly in nuclear power plants. The goal of ICF research is obtaining usable energy from nuclear fusion.

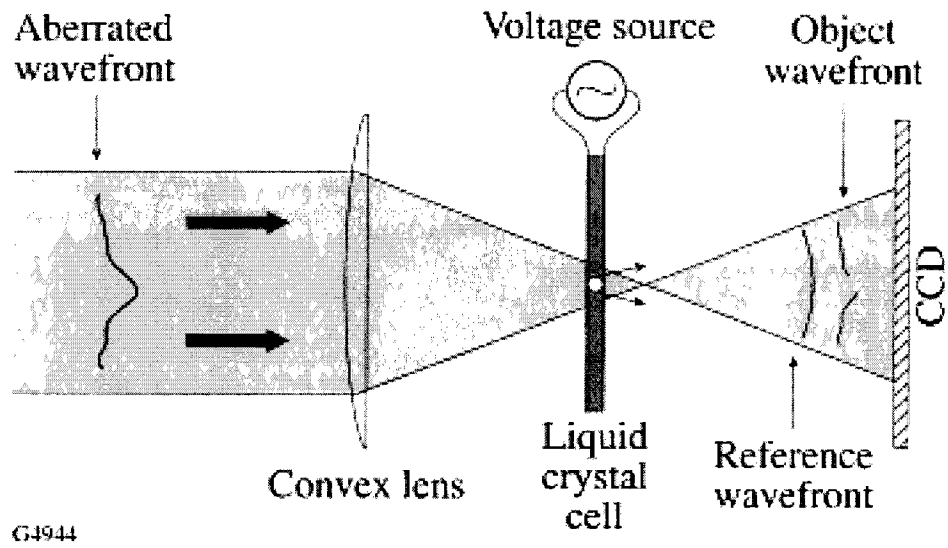
The OMEGA laser at the University of Rochester / Laboratory for Laser Energetics, the most powerful laser system of its type, researches inertial confinement fusion. OMEGA uses 60 laser beams to compress a small capsule filled with deuterium and tritium. The fuel reaches extreme density and temperature, allowing nuclear fusion to occur. Although new technologies, including smoothing by spectral dispersion (SSD) and cryogenics, have been applied to OMEGA to increase its performance, the system has yet to produce usable energy from fusion. The OMEGA laser and other ICF systems today are not advanced enough to produce more electrical energy than consumed. Even OMEGA’s successor, the National Ignition Facility (NIF, currently under construction), will not “break-even” in terms of energy return. The NIF is a large step in the right direction and hopefully in the future ICF can provide the world with cheap electricity [1].

The sixty laser beams used in OMEGA are reflected by mirrors and passed through lenses many times before they reach their target. By splitting and recombining a laser beam it can be characterized by interferometry. A device

called an interferometer can generate images called interferograms that are useful in finding flaws in laser beams and the optics they have encountered.

Many interferometers have been available commercially for some time. These interferometers, however, tend to be expensive, bulky, and complicated. Research is underway on a new type of interferometer, the Liquid Crystal Point Diffraction Interferometer (LCPDI) [2, 3]. The heart of an LCPDI is made from relatively inexpensive materials, fits in the palm of your hand, and has a phase-shifting ability inherent in its design. Because the liquid crystal center of an LCPDI can change refractive index with voltage, the LCPDI can easily examine a laser beam using a full range of phases. Commercial phase-shifting interferometers employ sophisticated mechanisms to the same end [4].

The LCPDI itself consists of a layer of liquid crystal sandwiched between two panes of glass. These glass windows are about 1 mm in thickness while the LC layer is less than 50  $\mu\text{m}$  thick. Between the windows and in the LC are several plastic beads. These beads can be spherical, ellipsoidal, or squished to the thickness of the gap. The LC is mixed with a dye that greatly attenuates any light not passing through one of these beads.



G4944

Figure 1: Schematic diagram of the LCPDI

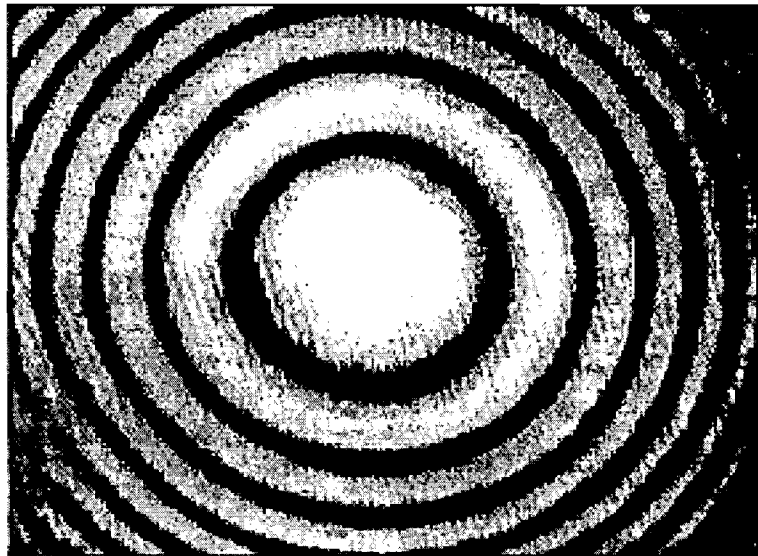


Figure 2: An interferogram, the result of the interference of the object and reference beams

To produce an interferogram (similar to Fig. 2), a laser beam is focused several microns past the center of one of these beads. A small portion of this laser energy strikes the bead and spreads out. The rest continues straight through the LCPDI cell, greatly attenuated by the dye dissolved in the LC. The small portion of spread light is assumed free of aberrations and is called the reference beam. The rest is called the object beam. The two beams, cast onto the same area of CCD camera, interfere to form a pattern of fringes called an interferogram.

Liquid crystals exhibit birefringence; their index of refraction in one direction is different from their index of refraction in the other. LCs also exhibit dielectric anisotropy; a voltage applied to the crystals causes them to rotate. By increasing the index of refraction of the LC, the object beam's optical path (number of cycles it has traveled before reaching the camera) can be adjusted and all of the phases of the object beam can be scanned.

## 2 Modeling the LCPDI

### 2.1 The Basic Model

Amy Turner, a student of the Summer High School Research Program, developed a computer model of the LCPDI [5]. This computer program tracked rays from their entry into the LCPDI to the points on which they interfered on the camera. For every ray  $\vec{x}_0$  headed in the direction  $\hat{c}_0$ , the program

calculated the point(s) it struck the spherical bead, if any:

$$\begin{aligned} \vec{x}_0 + s\hat{c}_0 &= \vec{x} \\ \left| \vec{f} - \vec{x} \right| &= R \end{aligned} \quad (1)$$

where  $\vec{x}$  is the intersection point,  $s$  is the distance the ray traveled before striking the sphere,  $\vec{f}$  is the center of the sphere, and  $R$  is its radius. The program used Equ. (2) for calculating  $s$ :

$$s = (\hat{c}_0 \cdot (\vec{f} - \vec{x}_0)) \pm \sqrt{R^2 + \left| \hat{c}_0 \times (\vec{f} - \vec{x}_0) \right|^2} \quad (2)$$

It also used Snell's Law to calculate the path each ray took toward the target plane:

$$\mu_0(\hat{c}_0 \times \hat{n}) = \mu_1(\hat{c}_1 \times \hat{n}) \quad (3)$$

where  $\mu_0$  and  $\mu_1$  were the indices of refraction,  $\hat{n}$  was the normal at the intersection point, and  $\hat{c}_0$  and  $\hat{c}_1$  were the directions of the ray before and after striking the interface. The optical path of each ray was also calculated. Optical path is defined as the sum of the distance traveled in each material times the corresponding index of refraction. Each optical path calculation determines the phase of the ray when it reaches the target plane. Turner's program calculated the interferogram based on the difference in path lengths between object and reference beams.

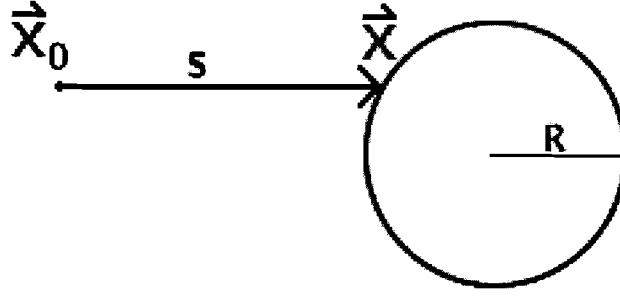


Figure 3: The ray  $\vec{x}_0$  with direction  $\hat{c}_0$  intersecting a circle

Rohit Rao, another Summer High School student, extended Turner's model to include the intensity of each ray in the calculation [6]. With Rao's extension each ray was tracked with a complex electric field. At each point in the target plane, the electric fields were summed with Eqn. (4) and the intensity was calculated with Eqn. (5):

$$E_{total} = E_{10}e^{-i\phi_1} + E_{20}e^{-i\phi_2} \quad (4)$$

$$I = \frac{1}{2\mu_0c} |E_{total}|^2 \quad (5)$$

where  $E_{10}$  and  $E_{20}$  were the complex electric fields of interfering rays,  $\phi_1$  and  $\phi_2$  were their phases (calculated from optical path length), and  $I$  was the final intensity used to plot the interferogram. Turner's program with Rao's extension created graphs comparable to experimental images.

## 2.2 Modeling the ellipsoid

Turner and Rao's program modeled the LCPDI assuming the central bead was a sphere. Often times when an LCPDI is constructed, the central bead

is “squished” and the resulting bead is shaped more like an ellipsoid. The program has been extended to account for ellipsoidal beads. The extension works similarly to the spherical code – for every ray  $\vec{x}_0$  headed in the direction  $\hat{c}_0$ , the program calculates the point(s) it strikes the ellipsoid, if any:

$$\begin{aligned}\vec{x}_0 + s\hat{c}_0 &= \vec{x} \\ a^2b^2 &= a^2|\vec{x}|^2 - (\vec{x} \cdot \vec{v})^2 \\ \vec{v} &= \langle 0, \sqrt{a^2 + b^2}, 0 \rangle\end{aligned}\quad (6)$$

where  $\vec{x}$  is the intersection point,  $s$  is the distance the ray travels before striking the ellipsoid,  $a$  is one-half the bead’s major axis, and  $b$  is one-half the bead’s minor axis (usually equal to the cell gap). For simplicity’s sake the ellipsoid’s center is assumed to be  $\langle 0, 0, 0 \rangle$ .  $\vec{v}$  is the vector from  $\langle 0, 0, 0 \rangle$  to a focus. The program uses Equ. (7) for calculating  $s$ :

$$s = -\frac{a^2c_{01}x_{01} + b^2c_{02}x_{02} \pm ab\sqrt{c_{01}^2(a^2 - x_{02}^2) + c_{02}^2(b^2 - x_{01}^2) + 2x_{01}x_{02}c_{01}c_{02}}}{a^2c_{01}^2 + b^2c_{02}^2}\quad (7)$$

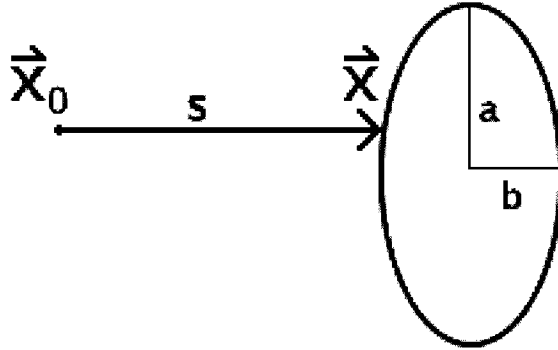


Figure 4: The ray  $\vec{x}_0$  with direction  $\hat{c}_0$  intersecting an ellipse

## 2.3 Modeling diffraction

Turner and Rao's program, even amended to include the ellipsoidal code, modeled only the effects of refraction and optical density. Diffraction, however, is a significant influence on the LCPDI and now can be modeled with the program. The intensity of each ray as it strikes the target (camera) plane is a function of every point  $(x, y)$  on the plane of the LCPDI's window. The complex electric field at a given point  $P$  on the target plane can be calculated with the Fresnel-Kirchoff diffraction integral [7, p. 380]:

$$E(P) = \frac{1}{4\pi} ik \iint_D \frac{e^{-iks}}{s} E(x, y) [\hat{c}_p \cdot \hat{n} + \hat{c}_o \cdot \hat{n}] dx dy \quad (8)$$

where  $k = \frac{2\pi}{\lambda}$ ,  $D$  is the plane of the LCPDI's window,  $s$  is the distance traveled by the ray from the window to the target,  $E(x, y)$  is the complex electric field at some point  $(x, y)$  on the window plane  $D$ ,  $\hat{c}_p$  is the direction from  $(x, y)$  to  $P$ ,  $\hat{c}_o$  is the direction of the ray at  $(x, y)$ ,  $\hat{n}$  is the normal of the window, and  $i$  is the imaginary unit.

## 2.4 Implementation

The program itself is written in PV-WAVE and is executed with a Unix-style shell script and Makefile. The program operates in two dimensions – on the  $yz$  plane with the direction of propagation being  $z$ . As input it accepts several arguments including the number of rays to be used for raytracing, resolutions of the window and target planes, wavelength of the laser being used, geometry (lengths and distances), refractive indices, and optical density of the liquid crystal. The program uses these parameters to create an array of light rays, each with an initial position, direction, and complex electric field. Typically

these rays form a spherical phase front without aberrations focused slightly past the LCPDI cell, but this can be modified. The rays propagate through air, the first glass window, the layer of liquid crystal, possibly the ellipsoidal bead in the center, and the second glass window, refracting and becoming attenuated as they go. At the interface between the second glass window and air, the rays are interpolated into an array of directions and complex electric fields. An array is also created on the target (camera) plane. The electric field of each point on the target plane is calculated discretely with the Fresnel-Kirchoff diffraction integral with the region of integration being the  $xy$  plane – the program assumes radial symmetry about  $y = 0$  to extend the window arrays into two dimensions. From the array of complex electric fields at the target plane, a graph of the interference pattern and several auxiliary graphs are produced. The interference graph simulates a lineout through the center of an actual interferogram.

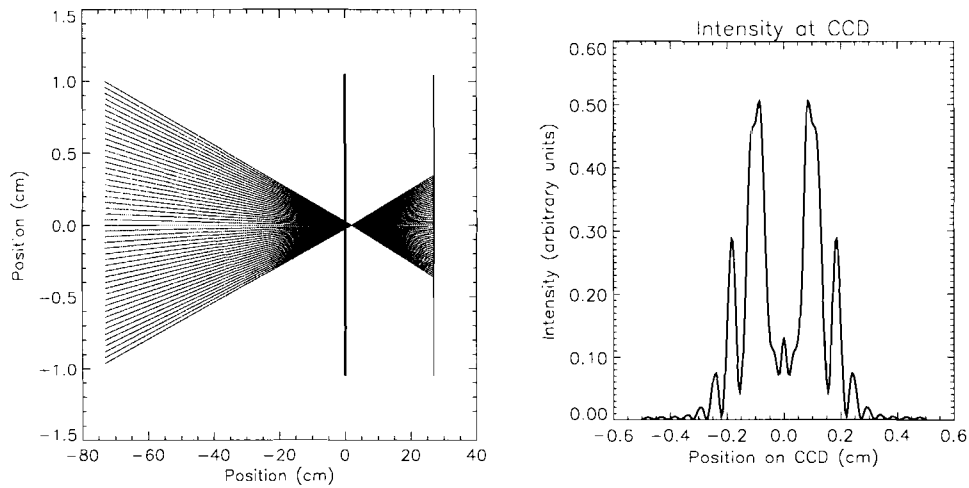


Figure 5: A schematic diagram and theoretical lineout, both output of the program

### 3 Results

The ability of the model to accept many parameters allows a variety of experimental conditions to be examined. This allows investigation of the properties of the LCPDI without fabrication, saving both time and materials. The model allows rapid investigation of the effect of each variable on the interferogram. Changing a variable in an experimental device can be difficult (focal length or laser wavelength) or impossible (cell gap or width of bead) and can often affect more than one variable – e.g. a change in the voltage over the liquid crystal may affect the dyes’ absorbance. The program can simulate devices not currently feasible to produce. The effect of darker dyes, different wavelengths, and more precise components can be studied before the devices are constructed. An interesting experimental phenomenon related to voltage increase and contrast can be explored with the help of the model. In a typical cell, when the voltage over the LC is zero, the interferogram shows good contrast – the difference between the brightest fringe and the darkest fringe is large. When the voltage is increased the LC’s refractive index changes and effects a change in the object beam’s phase. Sufficient voltage shifts the object beam’s phase by  $\pi$ . This phase shift causes a loss of contrast. When more voltage is applied and the object beam’s phase shift approaches  $2\pi$ , the contrast is restored. This phenomenon and others like it can be studied intensively out of the laboratory with this model.

## 4 Conclusions

An LCPDI computer model was extended to calculate spreading due to diffraction as well as refraction. The software can also model cells with elliptical beads. Through its flexibility, the LCPDI can be studied intensively outside the laboratory. The LCPDI is promising interferometric technology and the software model can be an aid to its development.

## 5 References

- [1] R. S. Craxton, et al., "Progress in Laser Fusion," *Scientific American*, Vol. 255, pp. 68 – 79, 1986.
- [2] C. R. Mercer and K. Creath, "Liquid-Crystal Point-Diffraction interferometer," *Opt. Lett.*, 19, p. 916, 1994.
- [3] C. R. Mercer and K. Creath, "Liquid-Crystal Point-Diffraction interferometer for Wave-Front Measurements," *Appl. Opt.*, 35, p. 1633, 1996.
- [4] "Comparison of a Liquid-Crystal Point-Diffraction Interferometer and a Commercial Phase-Shifting Interferometer," *Laboratory for Laser Energetics LLE Review*, 83, NTIS document No. DOE/SF/19460-357, p. 142, 1996.
- [5] A. C. Turner, "Ray Tracing Through the Liquid Crystal Point Diffraction Interferometer," *1998 Summer Research Program for High School Juniors at the University of Rochester's Laboratory for Laser Energetics*

*ics*, Laboratory for Laser Energetics Report No. 300, NTIS document No. DOE/SF/19460-299, 1998.

[6] R. Rao, “LCPDI Modeling,” *1999 Summer Research Program for High School Juniors at the University of Rochester’s Laboratory for Laser Energetics*, Laboratory for Laser Energetics Report No. 311, NTIS document No. DOE/SF/19460-338, 1999.

[7] M. Born and E. Wolf, *Principles of Optics*. Oxford: Pergamon, 5th ed., 1975.

## 6 Acknowledgments

One million thanks go to my project advisor and summer program coordinator, Dr. R. S. Craxton. Without his mathematical and technical explanations, help with debugging, and infinite patience, none of this study would have been possible. I thank B. Klehn, N. Turner, M. Guardalben, and K. Marshall for their experimental work and for familiarizing me with their laboratory. Another thanks goes to the IAL regulars, including M. Gao, M. Fiedler, and K. Monajati for their help and companionship. Special thanks go to L. Stein, for contributing his math and technical expertise, and R. Mukamel, for his coding wisdom and eagerness to share it. I lastly acknowledge all the scientists at the LLE, teaching us in more ways than one. You made this summer both educational and enlightening – thank you.

# **Experimental Simulation of Damage in Spatial Filter Lenses**

Abbey Rhode, Jason Taniguchi

Laboratory for Laser Energetics, University of Rochester  
*250 East River Road, Rochester, NY 14623-1299*

## **ABSTRACT**

The spatial filter lenses on the OMEGA laser system have required regular replacement due to bulk damage. When removed from the system, it was observed that many of the optics were contaminated with oil on their inner surfaces. Upon investigation, it was determined that oil from the mechanical pumps used to create a vacuum in the spatial filter tubes was the source of the contaminant. The oil is believed to have contributed to the formation of a type of damage morphology referred to as clamshell defects. The original purpose of the experiment was to recreate the clamshell morphology under controlled conditions. This proved to be harder to achieve than expected and the focus shifted to investigating how the oil contaminants affect the damage threshold of both sol-gel and hard oxide coated (HOCO) spatial filter lenses. Results showed that sol-gel coated lenses had a 15% lower damage threshold when contaminated than when clean. The difference of damage threshold between contaminated and clean HOCO lenses was negligible.

## **INTRODUCTION**

Spatial filter lenses on the OMEGA laser system require regular replacement due to bulk damage in the optics (see figure A). It is believed that this behavior is caused by oil vapor contamination of the spatial filter tubes. This vapor originates in mechanical vacuum pumps used to create a vacuum inside the tubes (see figure B). If left unchecked,

these damage sites could grow to the lenses' critical flaw depth, and implode under vacuum. This not only lowers the performance of the laser, but creates a situation dangerous to both OMEGA and the technicians that maintain it. In order to prevent such a situation, optics are regularly inspected for flaws.

Replacement due to damage is determined by the Half Critical Flaw (HCF) size of the optics. The HCF size is defined as half the depth of damage at which an optic will fail structurally. This depth is ascertained with a bending stress simulation, which combines the optics' physical characteristics (dimensions, density, Young's Modulus) with the load applied by the vacuum in the spatial filter tube, and calculates how deep of a flaw will cause the optic to crack and break. It is then assumed that the diameter of damage on the surface of the optic (measured tangential to the optic's surface) will be approximately twice the depth. A spatial filter lens will be replaced when half that diameter is reached to insure that the lens will not implode into the spatial filter tube. However, replacement of optics is undesirable due to the high expense and time wasted on realignments when new optics are brought into the system. Therefore an investigation was started into the cause of the defects found on spatial filter lenses, to make effective any strategy aimed at dealing with them.

Spatial filter lenses were first coated with a material called Sol-gel. Physically Sol-gel is a soft, extremely porous coating. The "-gel" portion of its name references its similarity to other gels, in that the slightest touch leaves a mark on the coating, ruining it for laser

applications. But while this coating is more difficult to handle than a hard oxide (HOCO) coating, it remains today as the best reflection minimizing coating available.

The mechanism thought responsible for damage formation is as follows: Spatial filter lenses with Sol-gel coatings, when on OMEGA, were able to absorb the previously alluded to oil vapor found in the spatial filter tubes due to the porous nature of the gel.

This vapor and Sol-gel combination found its way into micron-sized surface cracks in the lenses created by the grinding and polishing process. When combined, the oil and Sol-gel create a region of high refractive index, so high that upon exposure to laser light, this region gets much hotter than the surrounding oil-free area, and starts to cause cracks to the lens due to thermal effects. Upon further exposure to laser light, these cracks then grew into the observed damage sites. This mechanism is supported qualitatively by the following observations:

In the sol-gel coated lenses, a defect type known as clamshells have formed. These defects, which appear as slits on the surface, actually extend deep into the optic (see figure C). It is believed that tiny microscopic cracks in the optic (which have been observed in the past as a result of lens processing methods), when mounted on a spatial filter tube, are spread open on the vacuum surface due to bending stresses caused by the vacuum inside the tube. When the sol-gel then absorbs oil vapor, the contamination reaches into these cracks. When irradiated by laser light the oil burns and causes the clamshell defect to form. This theory is supported by a carbon residue found in the clamshell sites. A defect such as a clamshell has been shown to grow into larger damage sites when irradiated by laser light, similar to the kind found on damaged spatial filter

lenses. However, no quantitative data has been generated supporting this theory, and is what this experiment was designed to do. It should be noted that although these lenses have now been replaced with hard oxide coated (HOCO) lenses, which are not porous and therefore do not absorb the oil vapor, it is still suspected that the oil on the surface might contribute to the damage of the lenses.

This experiment used actual E-input lenses, with both HOCO and sol-gel coatings, contaminated and damaged on OMEGA, to investigate the effects of oil contamination on damage and the causes of clamshell defects.

## **APPARATUS**

In this experiment, a large area conditioning station (LAC) was used. It contains a Nd:YAG, 1064 nm, 1J laser that ran at 30 Hz pulses of 10 ns each (see figure D). To simulate OMEGA conditions, a cell was constructed that would hold E-input spatial filter mounts on both sides. This apparatus was connected to a Varian scroll vacuum pump and a gauge that would measure the pressure of the system. The lower the pressure, the better the vacuum. Three panels of filter glass and two panels of bead-blasted float glass were placed behind the cell to absorb and diffuse the laser light after it passed through the lenses. This cell setup was placed on the LAC1 Conditioning Stage (see figure E).

## **EXPERIMENT**

The E-input spatial filter lenses for the experiment had all previously been used and contaminated on the OMEGA system. This was done so that the optics used for the experiment had months of exposure to contamination, an important consideration as the

lenses require months to absorb the oil vapor. To insure the sol-gel coated optics used for the experiment were indeed contaminated with oil, a guided wave spectrophotometer scan was performed. This measured the amount of light being reflected off the surface of the optics over a range of wavelengths. The contaminated optics had a reflectance very similar to an uncoated piece of glass, meaning that the anti-reflective Sol-gel on them had failed. The sol-gel coated optics that were to be tested clean were chemically stripped of their contaminated coating and recoated with fresh Sol-gel. HOCO lenses from the system also had oil on their surfaces. After cleaning the original anti-reflective performance of the lenses returned, thus oil is believed to have not penetrated the HOCO coating.

Once clean and contaminated optics of each coating were collected, they were placed on the side of the cell that would receive the incident light. A clean sol-gel optic was used on the side of the cell where the light would exit. The vacuum was then pumped down to ~7 mTorr, a slightly lower pressure than in the Spatial Filter tubes on the OMEGA (~10 mTorr), to ensure that the bending stress would be equal to or greater than on the OMEGA. All scans were 30 mm diameter circles due to limitations of the stage diagnostics to monitor a scan. Multiple scans were made on each optic in places where there was no visible bulk damage from OMEGA. Scans were performed in both areas where there were no defects, and where there were clamshell defects. All testing was performed in an oil-free vacuum, any contamination on the optics was present prior to testing.

Contaminated HOCO and sol-gel coated optics were first scanned at increasing fluences until the damage threshold was reached. It was found that in using this method, any potential damage sites would grow rapidly into large pit morphologies, too quickly for quantitative data to be collected. This method did, however, provide the damage threshold of the optics. To try and allow for the more subtle clamshell growth, but at a more accelerated rate than on OMEGA, the contaminated optics were scanned repeatedly at fluences below their damage thresholds. No visible damage was seen after these scans. Due to time restrictions, the focus of the project was shifted to include the effect of oil vapor contamination on the damage thresholds of both HOCO and sol-gel coated lenses (see figure F).

Clean HOCO and sol-gel optics were then tested for damage threshold. The clean sol-gel coating damaged at  $\sim 19 \text{ J/cm}^2$  and at  $\sim 16 \text{ J/cm}^2$  contaminated. The clean HOCO damaged at  $\sim 16 \text{ J/cm}^2$  whereas the contaminated HOCO damaged at  $\sim 15 \text{ J/cm}^2$ . These fluence values are calculated for a 3 ns pulse length. It should be noted that while the difference in sol-gel damage thresholds is significant, the difference between the HOCO thresholds is within the error range of the measurement and therefore negligible.

## **CONCLUSION**

Results show that there is negligible difference between clean and contaminated HOCO optics' damage thresholds. Although the damage threshold of clean HOCO is the same as contaminated Sol-Gel, it does not lose its antireflective properties when exposed to oil vapor and is therefore the better optic for use in the contaminated spatial filter tubes.

Another benefit is the shorter amount of time needed to clean a dirty HOCO lens, as it does not need to be stripped of its coating, cleaned, then recoated as the Sol-Gel lenses do. HOCO coatings are durable enough that they can endure the entire cleaning process unaffected. In addition, oil filters have been placed on OMEGA to prevent further contamination. Additional study will be performed to assess the necessity of cleaning the current oil out of the spatial filter tubes on OMEGA.

Fig A.



Damage on spatial filter lens

Fig B.

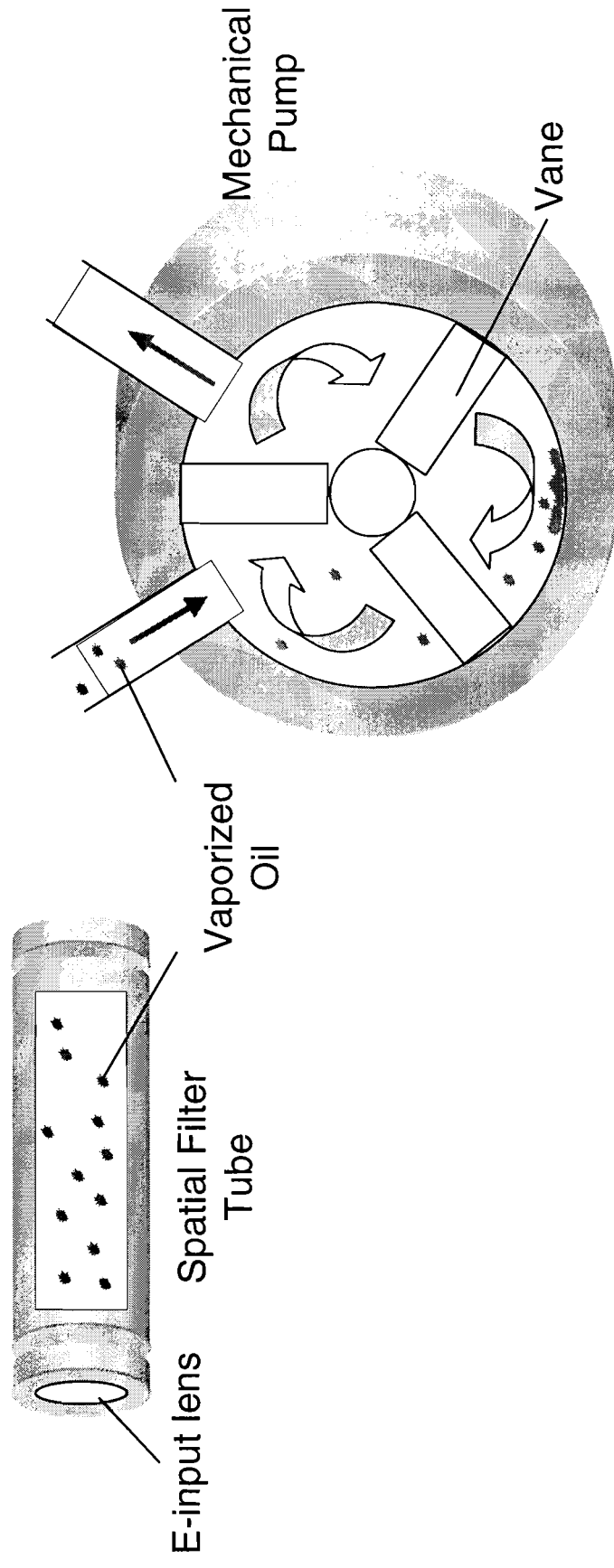
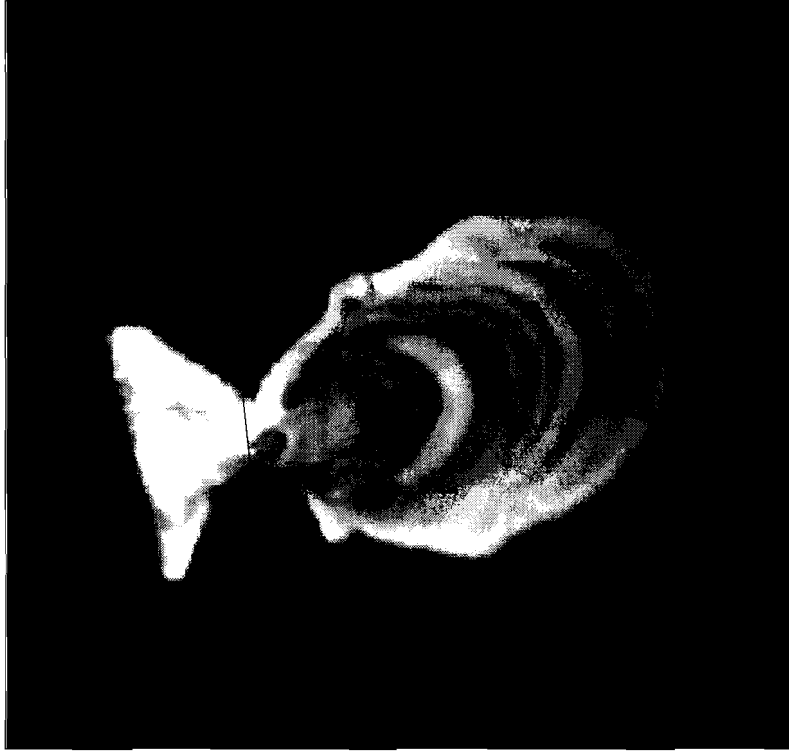


Diagram of Mechanical pump and spatial filter tube contamination

Fig C.



Clamshell defect found on Sol-Gel lens

Fig D.

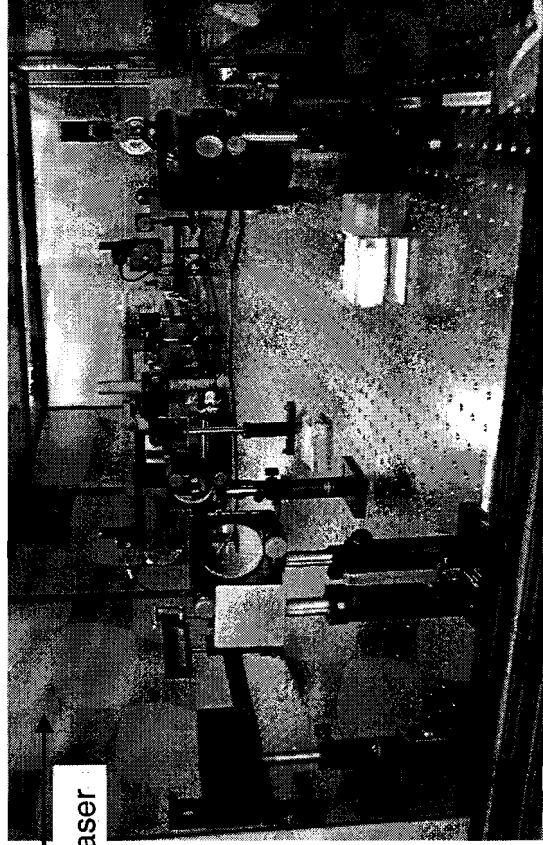
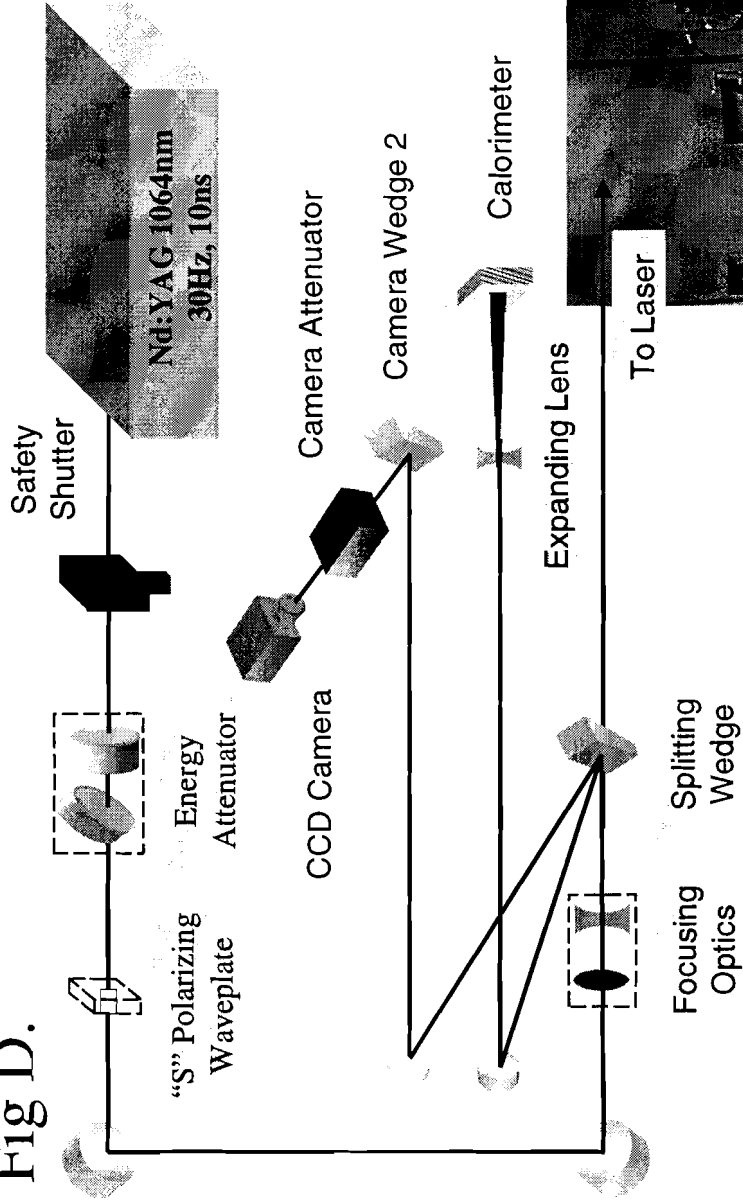


Diagram of LAC1 conditioning laser

Fig E.

LAC 1 Conditioning Stage

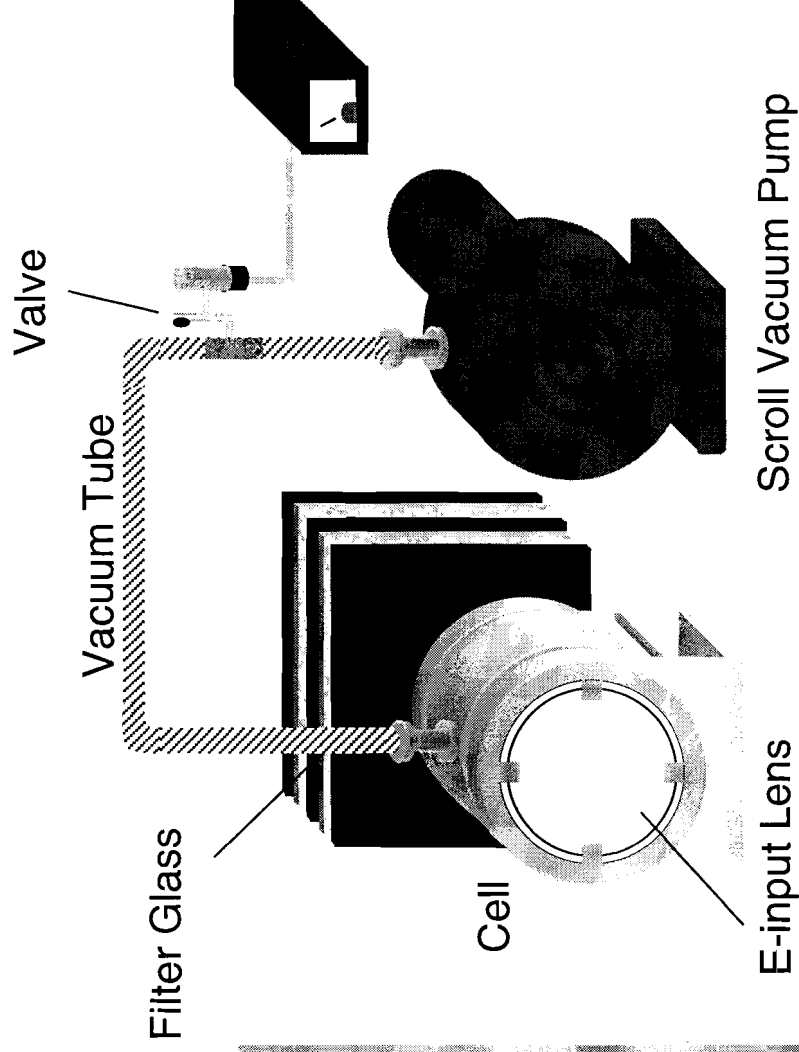
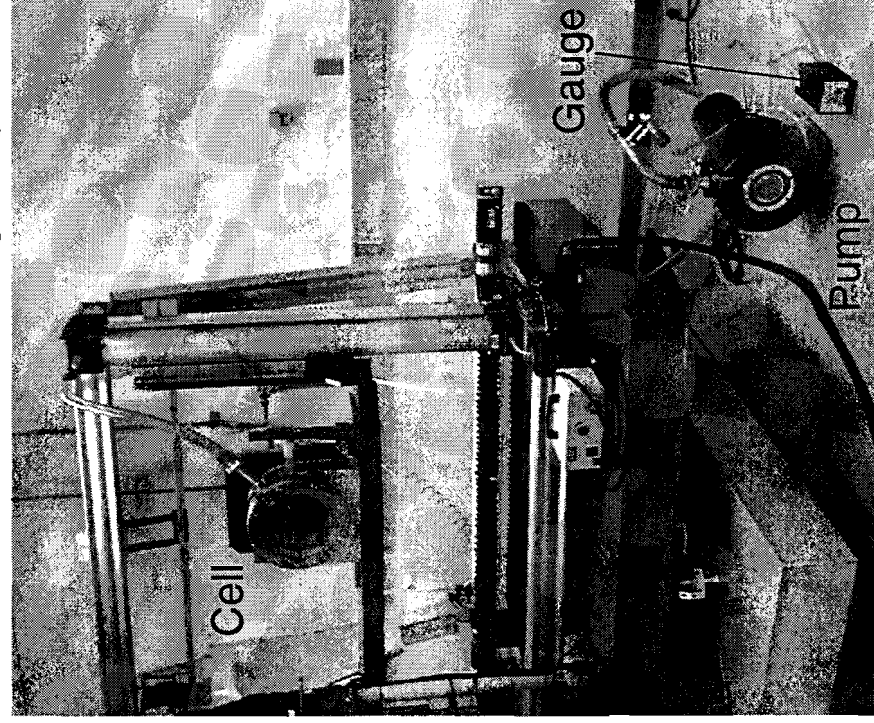
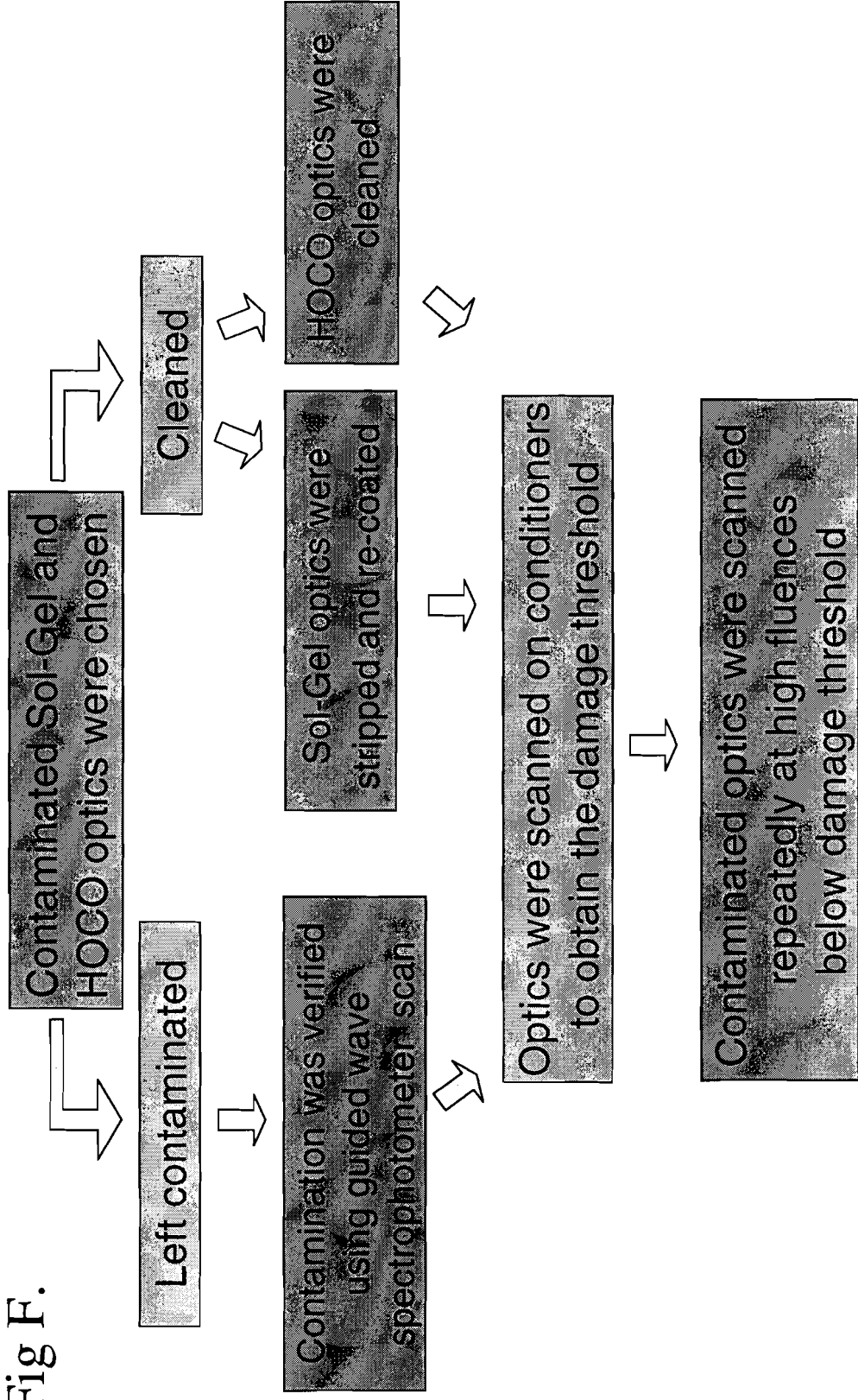


Diagram of experimental apparatus

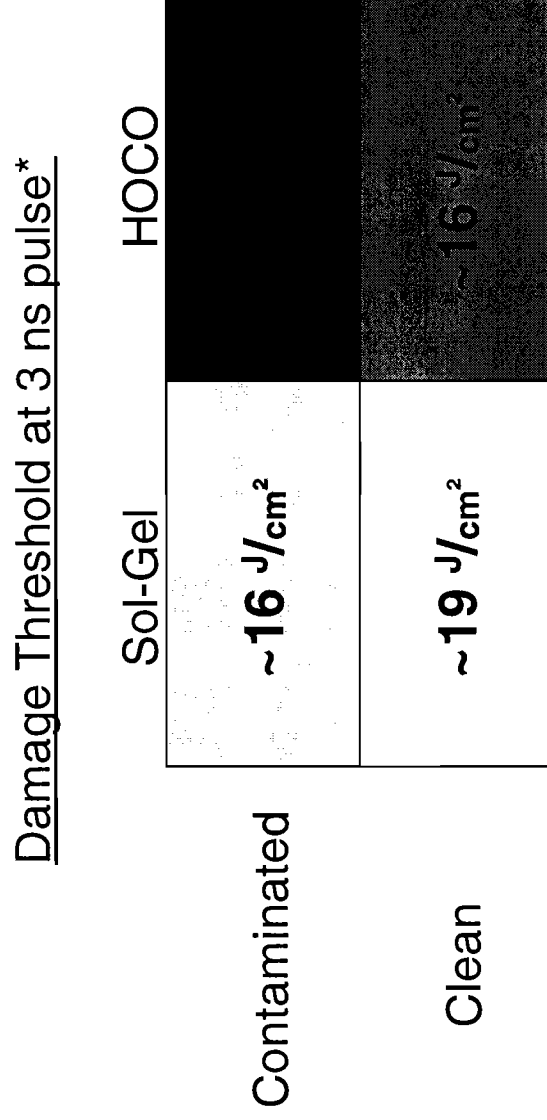
Fig F.



\*All scanning was done in 3 cm diameter circles due to restrictions of the laser

Experiment flow chart

Fig G.



**\*To convert to equivalent OMEGA fluences, multiply value by 0.68**

Results of experiment

# **Experimental Investigation of the Far Field on OMEGA with an Annular Apertured Near Field**

Uyen Tran

Advisor: Sean P. Regan

Laboratory for Laser Energetics Summer High School Research Program 2001

## **Abstract**

Far field intensity distributions of an OMEGA laser beam were measured with either an annular or a circular aperture placed in the near field. Annular and circular apertures were constructed and installed in the down-collimated beam of the OMEGA Wavefront Sensor (OWS). The annular aperture blocked the central portion of the beam with radii less than two thirds of the near field radius, while the circular aperture allowed only the central portion of the beam to propagate to the far field. One-nanosecond square laser pulses smoothed with 1 THz Smoothing by Spectral Dispersion (SSD) and polarization smoothing were studied. Power spectra of far fields measured with the UV Equivalent Target Place (UVETP) diagnostic were computed for each aperture and compared with measurements of the standard configuration on OMEGA with no near field aperture. Simulations show good agreement with the experimental data.

## **Introduction**

Laser beam smoothing is essential for direct-drive inertial confinement fusion. Nonuniformities in laser irradiation imprint target mass perturbations, which seed the ablative Rayleigh-Taylor hydrodynamic instability and degrade target performance. Single beam laser-irradiation nonuniformities are reduced using the following smoothing techniques: (1) smoothing by spectral dispersion (SSD), (2) distributed phase plates (DPPs), and (3) polarization smoothing (PS).

This investigation centered mainly upon the measurements of far field intensity distributions of an OMEGA laser beam with an annular apertured near field, a circular near field and a non-apertured near field. The non-apertured near field is the standard configuration used on OMEGA and is the control in this experiment. The apertures were constructed and installed in the down-collimated beam of the OMEGA Wavefront Sensor (OWS). One aperture was a circle with a diameter of two-thirds the diameter of the OMEGA near field and the other aperture, an annulus, was the inverse of the circular aperture. Far fields of one-nanosecond square laser pulses smoothed with 1 THz SSD and polarization smoothing (PS) were recorded with the ultraviolet equivalent target plane (UVETP) diagnostic and power spectra were calculated. Simulations are shown to be in good agreement with the experimental results.

The following sections discuss (1) the simulations of the near field, the far field, and the power spectral density of the far field intensity distribution and what they signify, (2) the construction and installation of near field apertures on the OWS and the far-field measurements with the ultraviolet equivalent target plane (UVETP) diagnostic, and (3)

the results of this investigation. The discussed results can be extrapolated to SSD smoothing of beams that irradiate only a portion of the phase plate, such as the dynamic focal spot size using a static phase plate.

### **Far Field Analysis**

Using computer codes written in the PV-WAVE language, models were made to simulate the near field of the OMEGA laser beam. The first type of near field that was modeled was the near field that corresponds to the control in this experiment. This is a near field without an aperture. The diameter of the circular near field on OMEGA is approximately 27 cm as seen in Fig. 1a. The modulus squared of the two-dimensional Fourier transform of the UV near field electric field is the far field, which is shown in Fig. 1b. Taking another Fourier transform yielded an image shown in Fig. 1c that resembled the near field. But more importantly, this image allowed the power spectrum of the far field intensity distributions to be analyzed. To obtain the power spectrum, the azimuthal sum of the square of the Fourier amplitudes was taken. The power spectrum is the intensity of the beam at various wave numbers  $k$ . The power spectral density (PSD) in Fig. 1d can be used to quantify the smoothness of the laser beam intensity profile. For example, one may compare the PSD of one model to another, or one experiment to another, or even a model to an experiment. Smoothing can also be compared by calculating the single beam irradiation nonuniformity  $\sigma_{\text{rms}}$ , which is defined as the square root of the ratio of the power in the high frequencies ( $k > 0.04 \mu\text{m}^{-1}$ ) to the power in the low frequencies ( $k < 0.04 \mu\text{m}^{-1}$ ). The  $\sigma_{\text{rms}}$  of the beam modeled in Fig.1 without SSD and PS is 100%. Laser beam smoothing reduces the  $\sigma_{\text{rms}}$ .

Secondly, a model of a near field with a circular aperture in place was created using PV-WAVE. The circular aperture made the near field a circle with a diameter of approximately 18 cm, or two thirds of the diameter of the non-apertured near field. This may be viewed in Fig. 2a. A far field image was obtained, shown in Fig. 2b, and it was noted that the speckle pattern produced contained speckles that were larger than those of the far field produced by a Fourier transform of a near field without an aperture. The power spectrum for the far field produced by this type of near field was calculated (Fig. 2c) and analyzed. The power spectrum shown in Fig. 2d resembled the one produced by the non-apertured near field, but a notable difference was that this graph, Fig. 2d, had a lower cutoff wavenumber than the graph associated with the near field without an aperture. This can be explained when one compares Fig. 1c with Fig. 2c. Both of the images are circular, but Fig 1c has more power at larger radii. The equation used to calculate the cut-off wave number is given as  $2\pi D/\lambda F$  where  $D=27$  cm is the diameter of the OMEGA beam,  $\lambda=0.351$   $\mu\text{m}$  is the laser wavelength, and  $F=180$  cm is the focal length of the OMEGA lens. When the circular aperture was placed in the near field, it caused the near field to have a smaller diameter. Nothing was changed in this equation except for  $D$ , which is directly proportional to  $k$ . Therefore if  $D$  gets smaller so does  $k$ .

A third near field with an annular aperture was modeled. This aperture made the near field a ring with a maximum diameter of 27 cm and a minimum diameter of 18 cm as shown in Fig. 3a. The far field here was also calculated. The result is in Fig. 3b. It was observed that the speckles produced were notably smaller than those of the far field created by the control. So the trend thus far is that the larger the near field the smaller the

speckle in the far field. Next, the power spectrum of this far field was obtained. The power spectrum is shown in Fig. 3d. It was compared to that of the non apertured near field in Fig. 1d and it was found that the graph of the PSD for the annulus had a different shape than that of the non-apertured near field, but the cutoff wavenumber was the same. Figures 1, 2, and 3 show how the near field irradiance affects the power spectrum of the far field intensity distributions.

### **Near Field Apertures**

Before any data could be taken, the apertures had to be fabricated and installed in the near field. The beam used in this experiment was down-collimated with the OWS to 63 mm which is equivalent to 30 cm in the OMEGA near field and allows for the use of smaller apertures and easy modification of the near field. The circular aperture was fabricated to allow only a small amount of the beam in the shape of a 1.637 in. diameter circle to pass from the near field to the far field. The annular aperture was made in the same way but in lieu of a circle, a ring with an outer diameter of 2.48 in. and an inner diameter of 1.637 in. blocked the central portion of the beam and allowed the outer portion of the beam to pass from the near field to the far field. The diameter of the circular aperture and the inner diameter of the annulus are equivalent to the two-thirds the diameter of the near field on OMEGA. These apertures are shown in Fig. 4. They were fabricated in the LLE machine shop.

Installation of the near field apertures on the OWS required more hardware to be made. The translator that the apertures were to be mounted on couldn't hold the apertures as they were. Rods and brackets were fabricated to allow the apertures to be compatible

with the translator, and to place the apertures at the height of the beamline of the OWS. This height was approximately 10 in. The rods were able to move vertically which allowed for precision alignment in that direction. The brackets had to allow the desired amount and shape of the beam to pass, which was kept in mind as the brackets were designed. As shown in Fig. 4, the bracket for the circular aperture was made with two tapped holes to fasten the aperture to the bracket and one through hole to connect the bracket to the rod. The bracket for the annular aperture was made in a similar fashion; however, it had to have a cut out between the two tapped holes (see Fig. 4). This was because without the cut out, a part of the beam would have been obstructed. An obstruction such as the one that would have been produced by the bracket would have been unfavorable due to the fact that it would have altered the near field in a way that was unwanted.

### **Experimental Results**

The investigation was conducted on the OWS. This is where 4% of the energy from an OMEGA beam is delivered for sampling. In this investigation, the beam propagates through a distributed phase plate (DPP) and an OMEGA lens. Next, the beam is down-collimated to a diameter of approximately 6 cm. The near field aperture positioned in the down-collimated beam of the OWS is shown in Fig. 5.

The aperture was mounted on a translator and then aligned to the center of the beam on the OWS. Steps were taken to record the exact positions that would allow the apertures to be centered properly. The rods had mechanical locks that kept the height properly aligned with the optic axis of the OWS, and the translator was marked to record

the horizontal location that would keep the aperture aligned to the center of the beam. During an OMEGA laser shot the far field of one of the apertures was recorded on a charged coupled device (CCD) of the UVETP diagnostic. When the data acquisition was completed, the aperture that was in the near field was replaced with another one and the procedure was again performed.

The Fourier transforms of the far fields were calculated using PV-WAVE and the PSD's of each of the near field apertured beams were compared to their respective models. Laser beam smoothing simulations of the 1 ns square laser pulse smoothed with 1 THz SSD and PS were performed by Dr. John Marozas for the three apertured near fields. Laser beam smoothing was not simulated in the models presented in figures 1-3. The laser beam smoothing effects of 1 THz SSD and PS are obvious after viewing the simulated power spectra shown in Fig. 6. Fig. 6a shows the power spectrum of the far field with an annular near field aperture and no laser beam smoothing, and Fig. 6b shows the power spectrum of the far field with an annular aperture and 1 THz SSD and PS. Simulations to account for 1 THz SSD and PS were run on the far fields that were recorded on OMEGA for the three apertures and the power spectra of the far field intensity distributions were calculated. The SSD smoothing technique involved temporal integration. The power spectra recorded for each aperture at the initial time looked similar to those presented in figures 1-3, except they had a lower  $\sigma_{rms}$  because of the PS. The power spectra of the time integrated far fields simulated with 1 THz SSD and PS were found to be in good agreement with the experimental data for all the near field apertures that were studied. Fig. 7 contains the results for the annular near field aperture.

The power spectrum at the beginning of the laser pulse is also shown for reference. Notice how it (thin curve) has higher intensity modulations than the curves with the laser beam smoothing of 1 THz SSD and PS. The simulation (the thicker solid line) is plotted over the measured power spectrum (the dotted line) and they appear to be in good agreement. Fig. 8 has the results for the circular near field aperture. Once again the thin black line is the power spectrum without SSD, and the simulated data shows good agreement with the measured results. Fig. 9 shows the simulated and experimental power spectra for the standard configuration on OMEGA. Again, the thin curve is the model without SSD and the thicker line is the model with smoothing which shows good agreement with the measured power spectrum (the dotted line). The general shapes of the lines in Fig. 8 look similar to these, but the cut-off wave number for Fig. 8 is less. The cut-off wave number for Fig. 7 is the same as this one, but the shapes of the power spectra differ because of the different near field aperture shapes.

## **Conclusion**

Far field intensity distributions of an OMEGA laser beam were measured with either an annular or a circular aperture placed in the near field. Models were created with PV-WAVE to understand the relationship between the near field irradiance and the power spectrum of the far field intensity distributions. Hardware was fabricated to install annular and circular apertures in the down-collimated beam of the OWS. One-nanosecond square laser pulses smoothed with 1 THz SSD and polarization smoothing were studied. Power spectra of far fields measured with the UVETP diagnostic were computed for each aperture and compared with measurements of the standard

configuration on OMEGA with no near field aperture. Laser beam smoothing simulations show good agreement with the experimental data. Results from this investigation can be extrapolated to SSD smoothing of beams that irradiate only a portion of the phase plate, such as the dynamic focal spot size using a static phase plate.

### **Acknowledgments**

Thank you to Dr. Craxton for allowing me to participate in this program. Few high school students have the opportunity to work with the OMEGA laser system or the scientists who work on OMEGA. I am truly fortunate. Thank you also to Dr. Marozas for the simulations. Without the simulations, I would have nothing to compare the experimental data with. I give special thanks to my advisor Dr. Regan. He was patient with me when explaining concepts and helped me to complete this study. He taught me how scientists conduct experiments each step of the way. Thank you.

## Figure Captions

Figure 1. The models for the standard configuration used on OMEGA created using PV-Wave are shown here. The near field intensity is shown in (a), the modulus squared of the 2-D Fourier transform of the UV near field electric field is the far field shown in (b) and the Fourier transform of (b) is used to evaluate the power spectrum in (c), notice how it resembles the near field. Power spectral density is shown in (d) which is the azimuthal sum of the square of the Fourier amplitudes.

Figure 2. These are models for the circular aperture. The image (a) is the near field intensity, (b) is the far field intensity, notice how the speckles are larger here than for Fig. 1b. (c) is the Fourier transform of (b) and (d) is the power spectrum. Notice that the cut-off wave number for this power spectrum is less than the one for Fig. 1d. This is because the diameter of the circular near field is smaller, so the cut-off wave number has to be smaller.

Figure 3. These are models for the annular aperture. The image (a) is the near field intensity, which now looks like a ring because the aperture is blocking the central portion. (b) is the far field intensity, notice that speckles are smaller here than for Fig. 1b. (c) is the Fourier transform of the (b) and (d) is the power spectrum. The cut-off wave number is the same as in Fig. 1d because the diameters are the same, but the shape is different due to the annular near field aperture.

Figure 4. These are the near field apertures. The diameter of the circle and the inner diameter of the annulus are equal to 1.637 in. The apertures can be this small when the beam is 30 cm because the beam was down-collimated to 63 mm on the OWS. So the diameter of the apertures above is really just a little less than two-thirds of the near field diameter on OMEGA.

Figure 5. This is the experimental setup. The table is the OWS in the OMEGA target bay. A sample beam with 4% of the laser light energy is passed through a DPP and an OMEGA lens. The beam is then down-collimated, passed through an aperture, and brought to a focus on a CCD camera to measure the far field.

Figure 6. These are power spectra for the annulus. The graph of (a) is the one modeled with PV-Wave. It didn't take into account SSD so the  $\sigma_{rms}$  was high. Graph (b) is the power spectrum of the far field of a 1 ns square laser pulse smoothed with 1 THz SSD and PS, so the intensity modulations were much lower.

Figure 7. This graph shows the power spectra for the annulus. Notice how the thin curve has a higher intensity than the curves with the laser beam smoothing of 1 THz SSD and PS. The simulation (the thicker solid line) is plotted over the measured power spectrum (the dotted line) and they appear to be in good agreement.

Figure 8. The power spectra for the circular aperture are shown here. Once again the

thin black line is the power spectrum without SSD. The dotted line is the measured spectrum with 1 THz SSD and PS. The thicker solid curve represents the simulated data with 1 THz SSD and PS and shows good agreement with the experimental result.

Figure 9. These are the power spectra for the standard configuration on OMEGA. Again, the thin curve is the model without SSD and the thicker line is the model with smoothing which shows good agreement with the measured power spectra (the dotted line). The general curve of the lines in Fig. 8 look similar to these, but the cut-off wave number for Fig. 8 is less. The cut-off wave number for Fig. 7 is the same as this one, but the shapes differ.

Fig.1

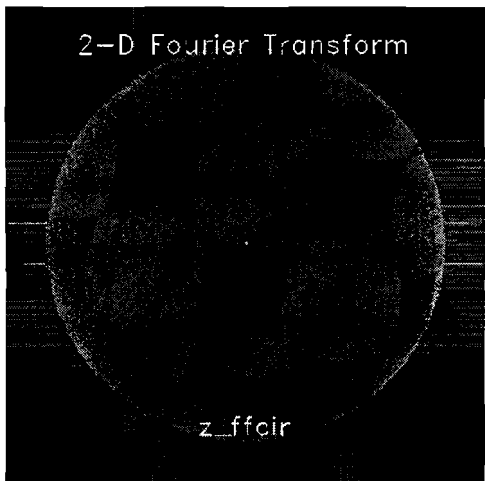
(a)



(b)



(c)



(d)

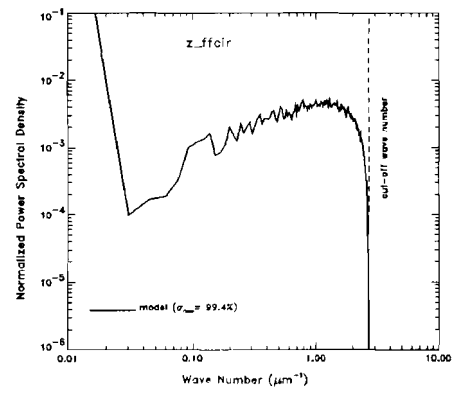
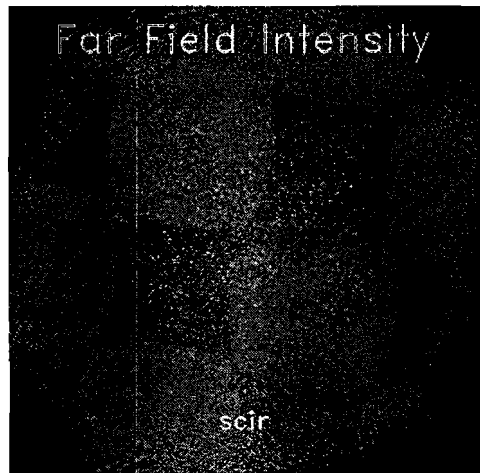


Fig. 2

(a)



(b)



(c)



(d)

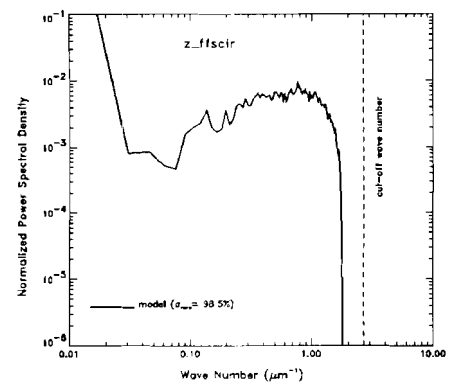
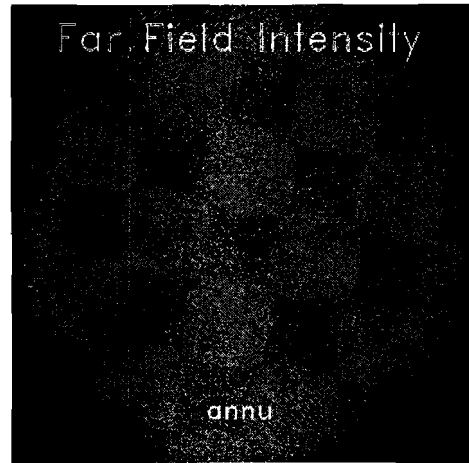


Fig. 3

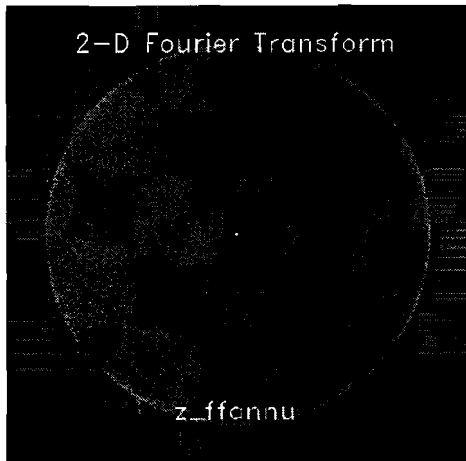
(a)



(b)



(c)



(d)

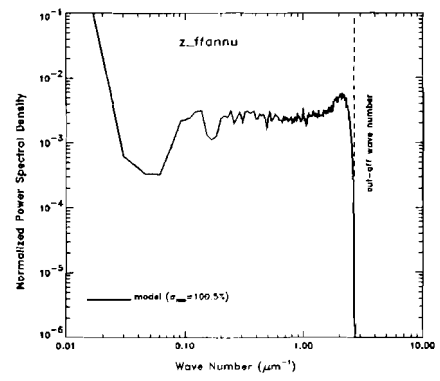


Fig. 4

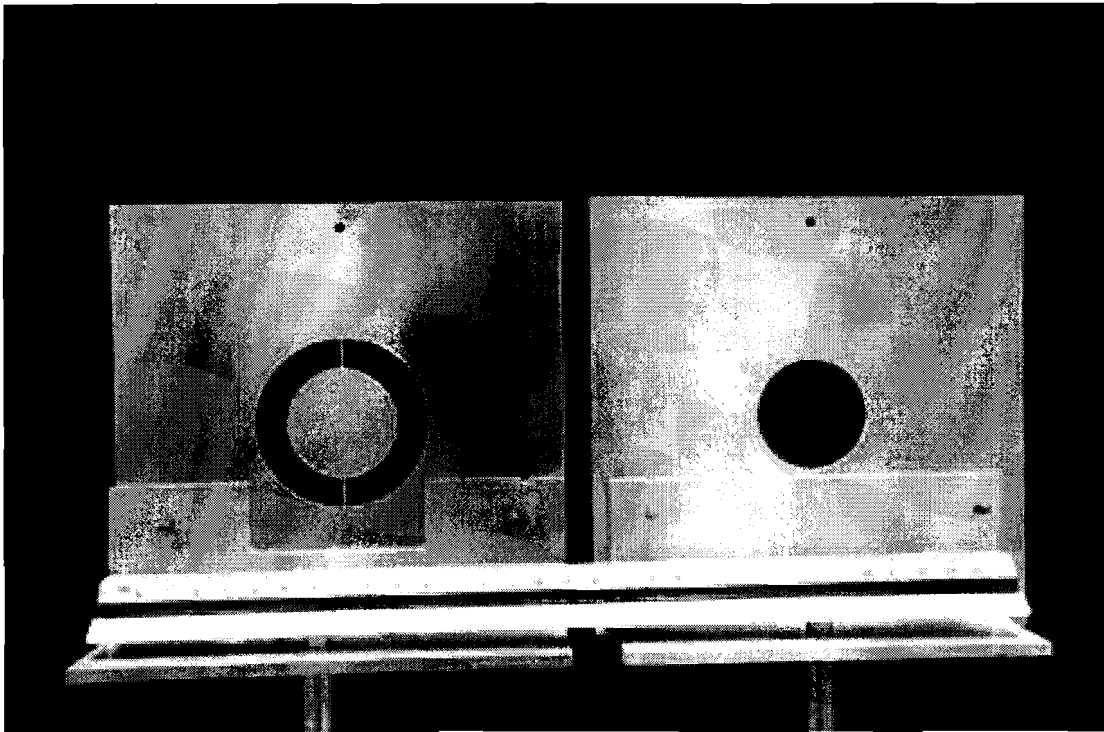


Fig. 5

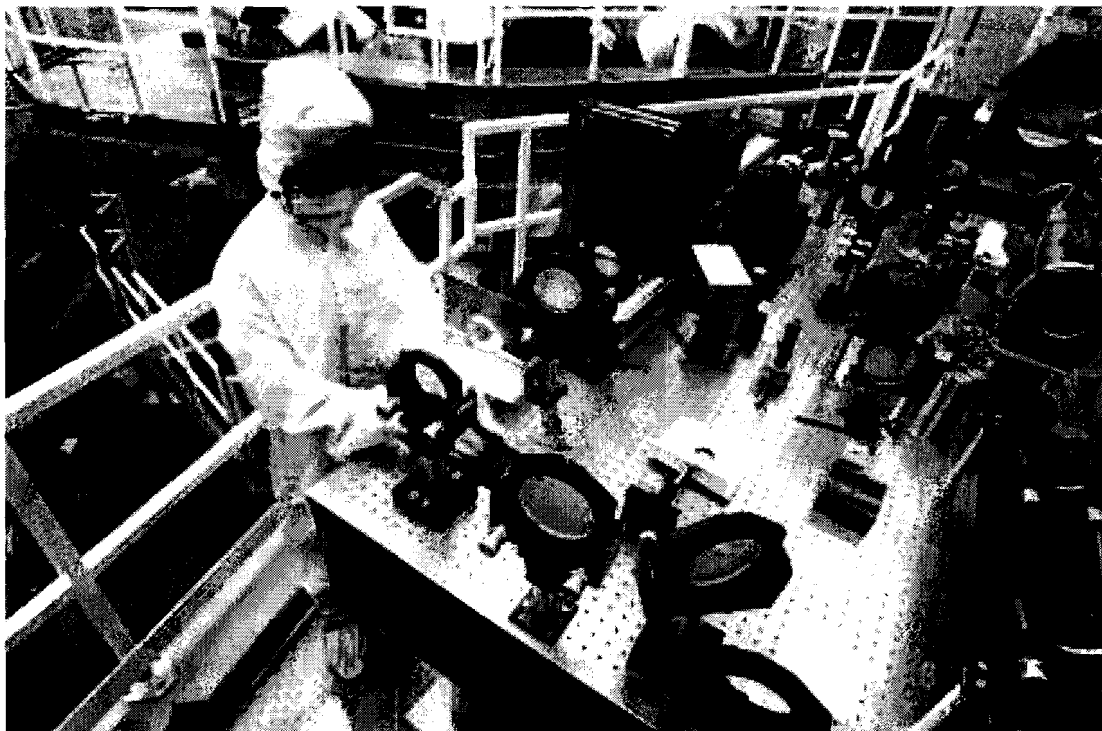
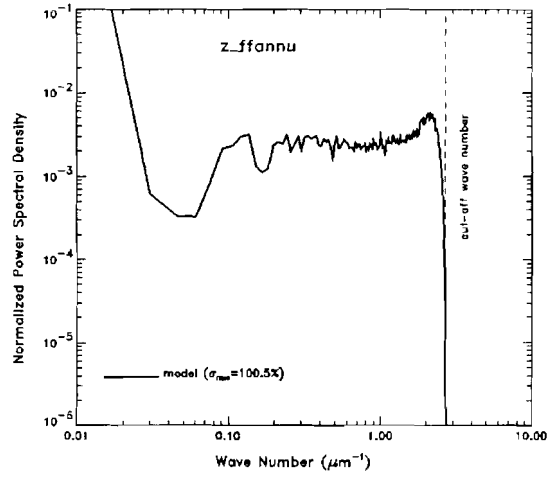


Fig. 6

(a)



(b)

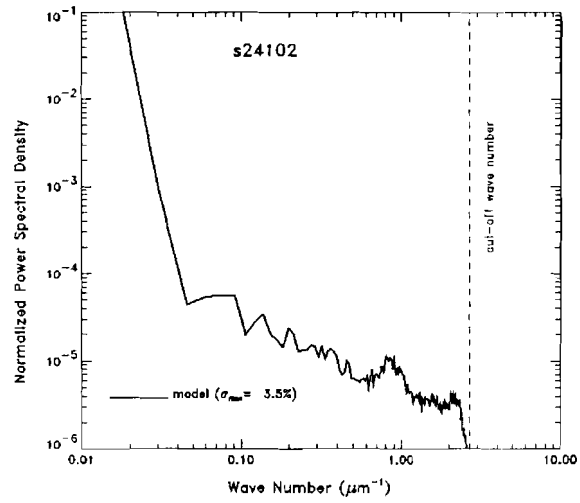


Fig. 7

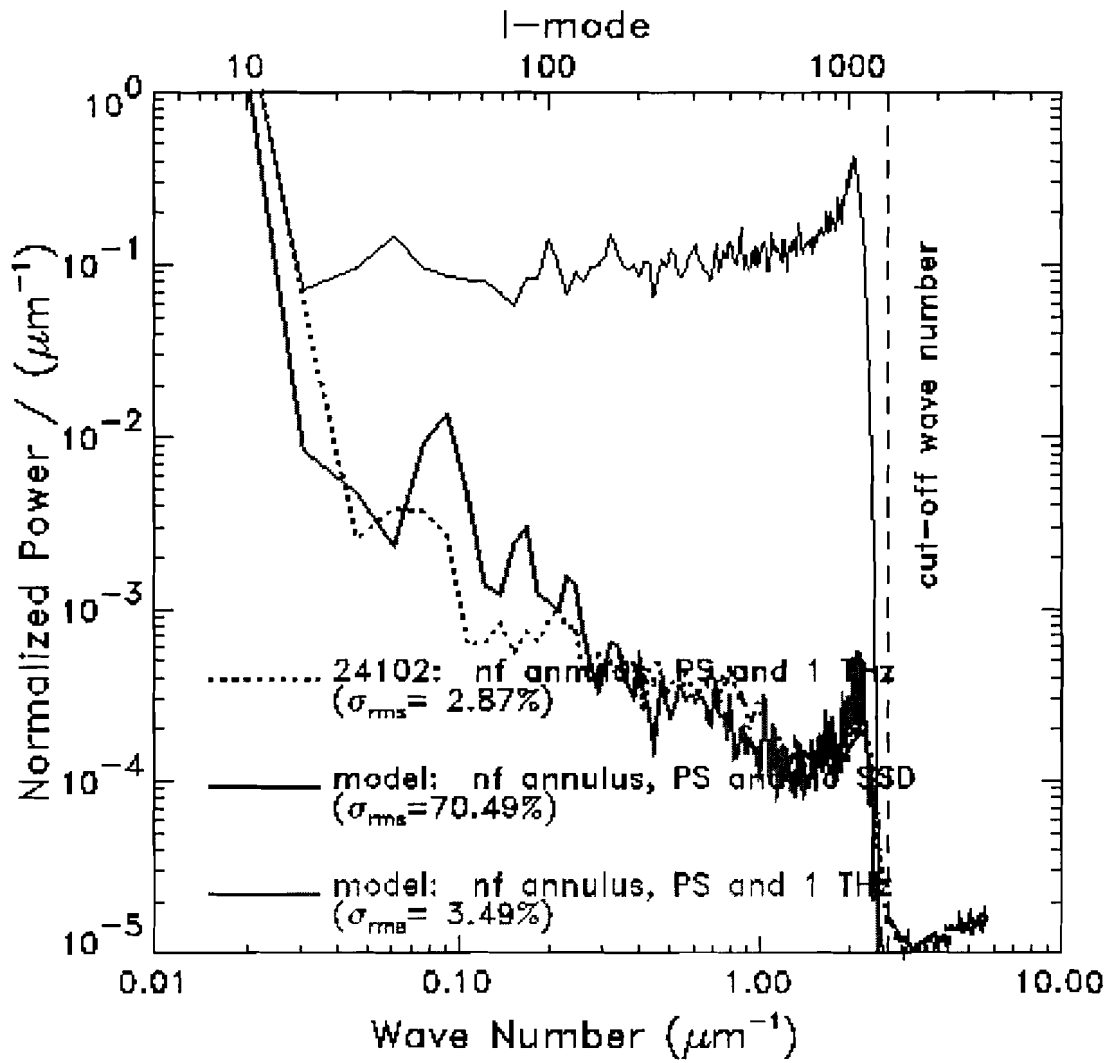


Fig. 8

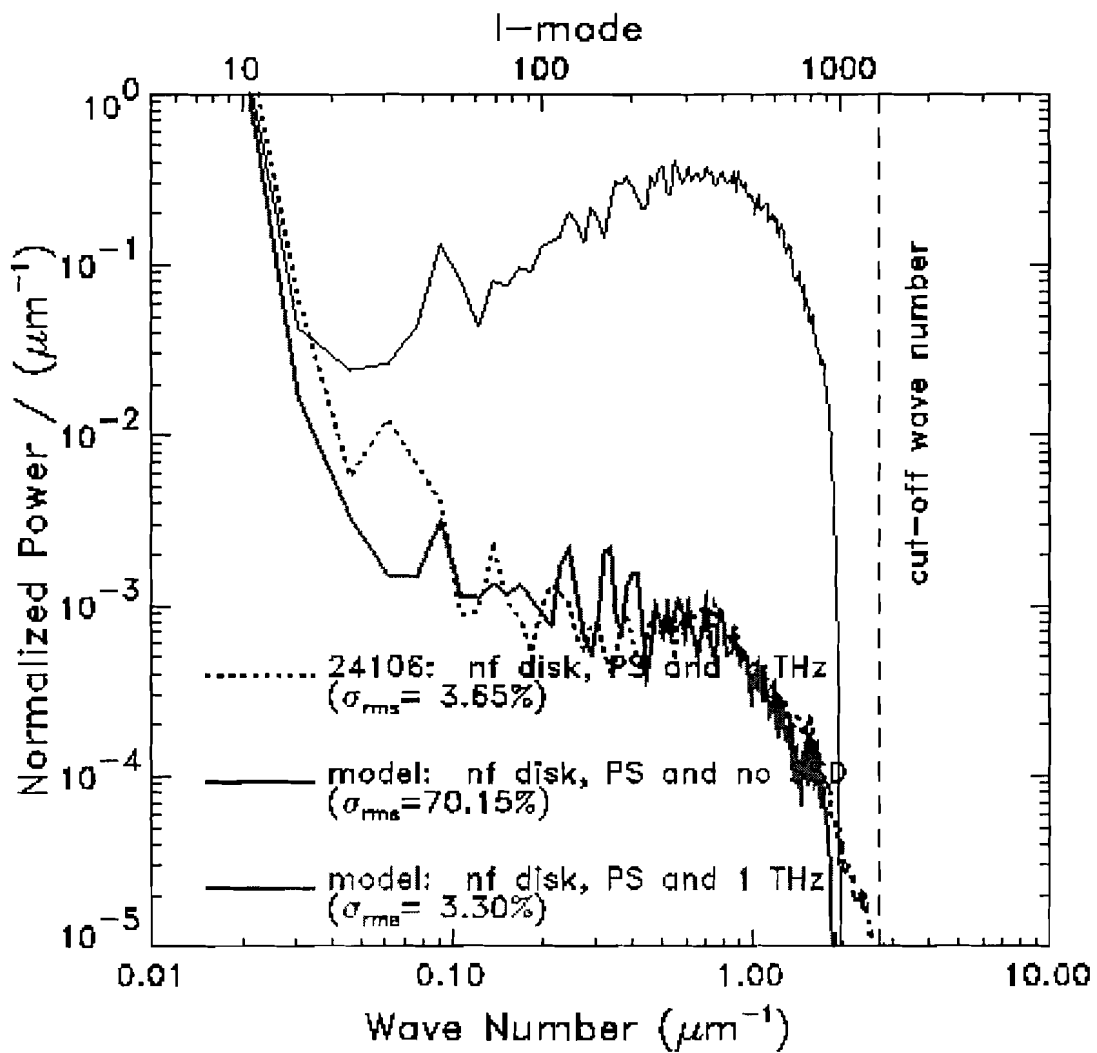
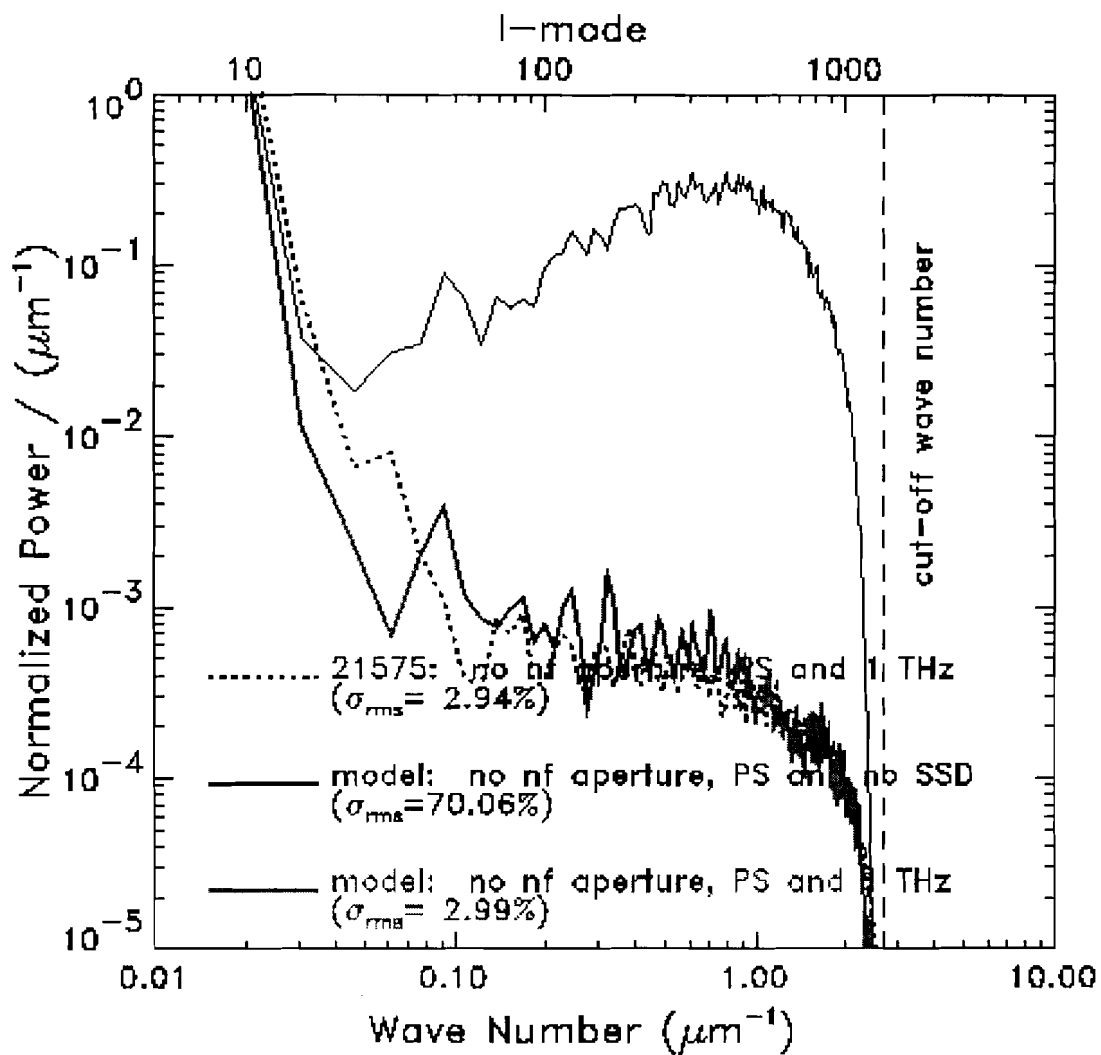


Fig. 9



# **Cryogenic Permeability of Polyimide Shells**

*James Wang*  
McQuaid Jesuit High School  
Rochester, NY

2001 Summer Research Program for High School Juniors  
Advisor: Dr. David Harding

LABORATORY FOR LASER ENERGETICS  
University of Rochester  
250 East River Road  
Rochester, NY 14623-1299

**Polyimide shells are used as targets in Inertial Confinement Fusion (ICF) experiments. These shells are filled with DT gas, then cooled to low temperatures for cryogenic laser shots. During target preparation, shells require careful pressure and temperature control due to their sensitivity. The pressure is governed partly by permeation through the shell wall, which can only be determined with the knowledge of the shell permeability over a wide temperature range. A new method was developed to test the permeability of shells at temperatures ranging from 123K to 23 K. This method produced results at room temperature comparable to those using current setups. Arrhenius' relationship was observed from room temperature to 120K and the activation energy for permeation was determined for shells prepared under different processing conditions. The results will allow the permeability of shells to be predicted for various temperatures.**

## I. INTRODUCTION

Nuclear fusion is a promising source of energy for the future. One of the current approaches toward nuclear fusion is Inertial Confinement Fusion, which uses lasers to compress a spherical shell no larger than 1 mm filled with DT gas. The shells used in the OMEGA Laser System at the University of Rochester are hollow spheres made of Polyimide with walls of 3-5  $\mu\text{m}$  thick and weight of 0.2-0.4 mg (see Figure 1). The design of an OMEGA target calls for a solid 100  $\mu\text{m}$  thick layer of solid DT uniformly adhered to the inner surface of the shell. To prepare these cryogenic targets, the shells must first be filled to 1000 atm at 300K, then cooled slowly to 19K. The cooling process induces a pressure gradient across the shell wall due to non-uniform temperature distribution in the pressurization chamber<sup>1</sup>. To avoid too high of a pressure gradient, which will cause the shell to buckle or burst, the cooling rate must be slow. The exact rate of cooling can only be determined by knowing permeability (Kp) of the shell wall from cryogenic to room temperature. In this study, a new setup was developed to test the permeability of polyimide shells at a broad temperature range (see Figure 2). This setup can also be used to determine the properties of the polyimide shell prepared under the specific processing conditions at room temperature, which are well characterized, and at cryogenic temperatures, which are unknown.

## II. EXPERIMENTAL

The schematic drawing of the apparatus for measuring the shell  $K_p$  at low temperatures is shown in figure 2. The setup consists of the supply line, pressure transducer (MKS Instruments 722A, 1000 torr), temperature controller (Cole Parmer DigiSense), sample chamber (1 1/3 inch conflats with 3/8 inch pore), cooling mechanism, and leak detector (Edwards Spectron 600D). The sample chamber had a system of three sealed conflats. The permeation surface was glued to the middle conflat. Upstream of the sample chamber was the supply line containing Helium and the pressure transducer. A copper ring surrounding the chamber with two fingers immersed in nitrogen (77K) cooled the sample chamber. A 400-watt cartridge heater and a K-type thermal couple were attached to the copper housing to allow for temperature control. The temperatures measured include 130K, 200K, 251K, and 295K. The leak detector measured the Helium leak rate in the unit of standard cc/s, which was then converted to mol/s using the ideal gas law.

Equation 1:

$$n / t = (K_p \times A \times \delta P) / l$$

$n$  = mols of gas

$t$  = time (s)

$K_p$  = permeability constant

$A$  = surface area of membrane

$\delta P$  = pressure differential

$l$  = thickness of membrane

The shell-plate was prepared by drilling 6 shell-sized holes in a miniature brass plate (Area: 1.5 cm<sup>2</sup>, Thickness: 0.25 cm), as shown in figure 3. Six shells were glued to the plate using Epoxy, which is impermeable to gases, in a manner that covered the holes. Holes were then poked through the shells on the hemisphere below the brass plate. This allowed gas to enter the shell through the hole and permeate through only one layer of the shell membrane. This shell-plate was attached to the central conflat using Epoxy. The diameter of the shells used and the thickness of shell walls were measured using previously reported methods<sup>1</sup>.

This new setup was calibrated against existing setups, including a flat-film apparatus<sup>1</sup> and a Time Constant setup<sup>2</sup> for shells. The shells tested were either cured in N<sub>2</sub> or air<sup>1</sup>. The upstream pressure was approximately 1.4 atm, and the type and grade of gas used was UPC Helium.

### III. RESULTS & DISCUSSION

The accuracy of the measurements taken on the new shell-plate setup at room temperature is confirmed by comparing its results with those using other testing setups (as shown in Table 1). There are, however, minor differences between the data, which may be attributed to the following reasons:

- (1) Variations in the permeability due to the fundamental microstructure differences between film and shells. Processing conditions allow shells to be more uniformly thick than films due to the difference in surface area.
- (2) The pressures used for each apparatus are different. In the Time Constant setup, the shells are filled with 7.5 atm, while in the other two setups, only 1.4 atm is applied to the shells or film. The  $K_p$  of polymeric materials usually have a dependence on pressure, so the higher the pressure, the higher the  $K_p$ .

At low temperatures, the results obtained using the new setup also agree with previous measurements using flat films<sup>1</sup> (as shown in Figure 4). The temperature dependence of  $K_p$  of both air and  $N_2$  cured samples followed Arrhenius' relationship (Equation 2) over the experimental temperature range (Table 2). The thermal activation energy for permeation ( $E_p$ ) obtained from the slope of the linear relationships in Figure 4, which were 18.1 kJ/mol and 18.6 kJ/mol for  $N_2$  and air cured samples respectively, and the following equation.

Equation 2:

$$K_p = K_{p_0} \times e^{-E_p/RT}$$

It was also observed that the  $N_2$  and air cured samples maintained the same permeability relationships at low temperatures.

#### IV. CONCLUSION

Knowledge of permeability at a broad temperature range is important to Inertial Confinement Fusion experiments because permeation is a critical process for preparing cryogenic targets. With the new shell-plate setup, permeability of shells can now be measured at a broad temperature range. The activation energy for permeation has been determined for polyimide shells in this study, which will allow for the prediction of the shell permeability at low temperatures. It was also observed that shells prepared under various curing conditions maintained their permeability differences at cryogenic temperatures.

#### V. ACKNOWLEDGMENTS

My progress this summer would not be possible without the help of the entire Target Fabrication departments at the University of Rochester Laboratory for Laser Energetics. I would especially like to thank Dr. David Harding for incorporating me into his department. Sal Scarantino patiently helped me with my testing apparatus. Feng-Yu Tsai directed and supervised my entire project. He is the largest contributor to my progress, and I thank him for a great time this summer.

I would like personally to thank Dr. R. S. Craxton and all of University of Rochester Laboratory for Laser Energetics for allowing me to explore the world of scientific research. During my research time at the laboratory, I have learned more than any high school course could ever teach me. I hope that more students will be exposed to this wonderful program and will embrace the scientific frontier as I have this summer. Thanks again.

## VI. REFERENCES

1. F.-Y. Tsai, E.L. Alfonso, S.-H. Chen, and D.R. Harding, "Process vapor deposited polyimide," to be published in *J. App. Phys.*
2. F.-Y. Tsai, E.L. Alfonso, S.-H. Chen, and D.R. Harding, "Mechanical properties and gas permeability of polyimide shells fabricated by the vapor deposition method," *Fusion Technol.* 38(1), 83-89 (2000).
3. M. Bonino, R.Q. Gram, D.R. Harding, S.G. Noyes, J.M. Soures, and M.D. Wittman, in *Eleventh Target Fabrication Specialists' Meeting (Orcas Island, WA, 1996)*.
4. R.S. Craxton, R.L. McCrory, and J.M. Soures, "Progress in Laser Fusion," *Scientific American.* 225, 68-79 (1986).
5. L.M. Costello and W.J. Koros, "Temperature Dependence of Gas Sorption and Transport Properties in Polymers: Measurements and Applications," *Ind. Eng. Chem. Res.* 31, 2708-2714 (1992).
6. A. Lebovits, "Permeability of polymers to gases, vapors, and liquids," *Modern Plastics.* 139-150, 194-210 (March, 1966).

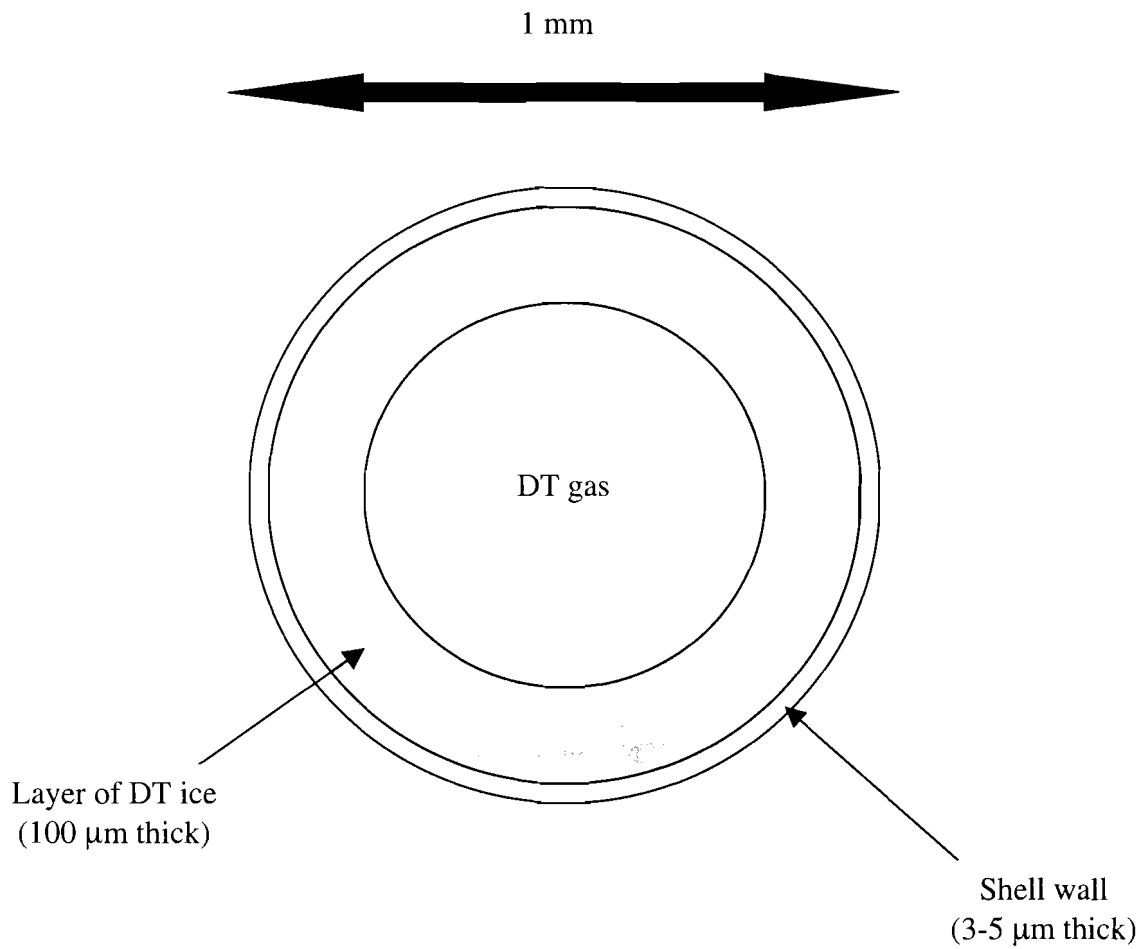


**FIGURE 1:** A schematic of the design of OMEGA targets.

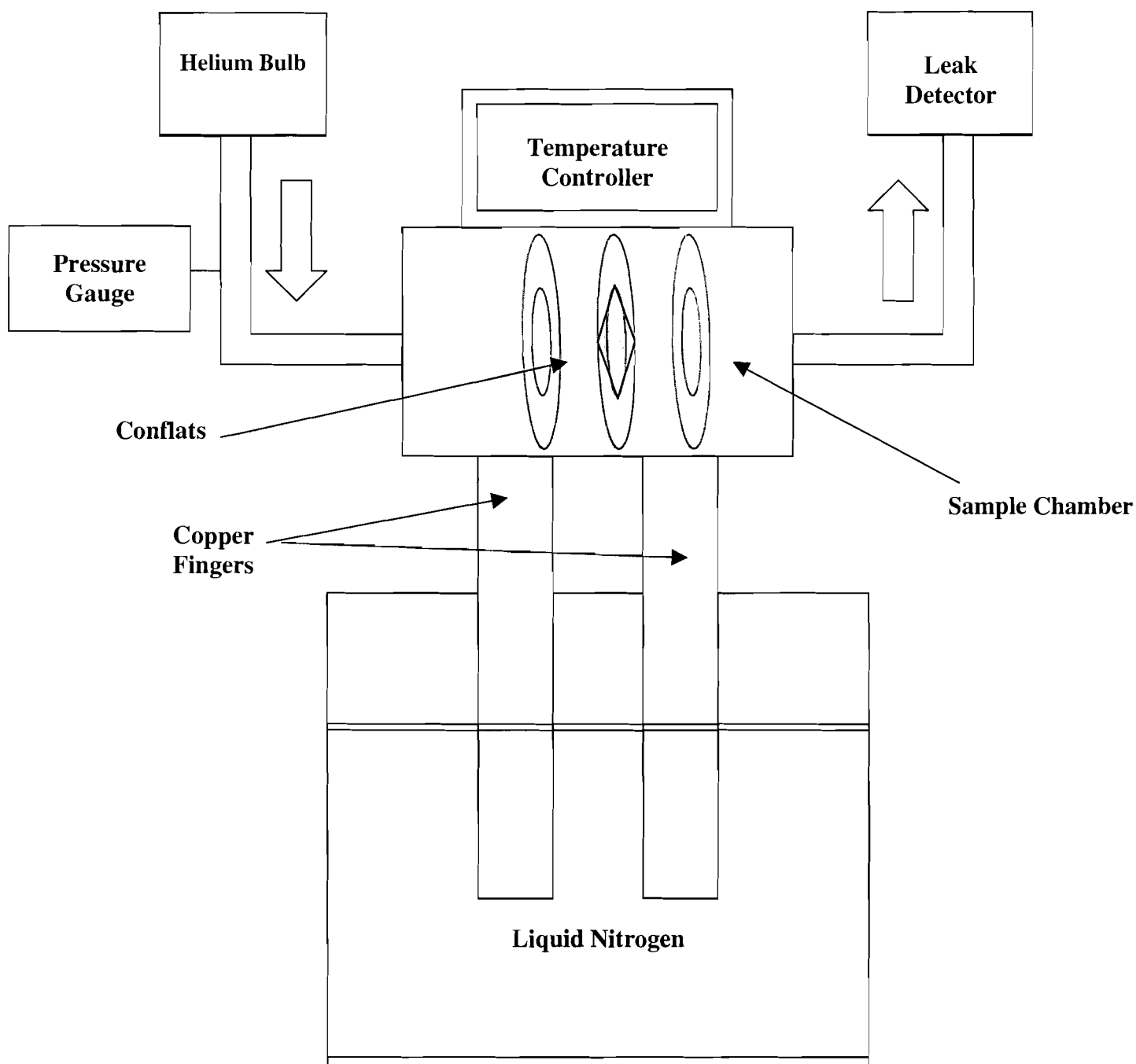


**FIGURE 2:** A schematic drawing of the experimental setup. Upstream of the sample chamber are the Helium reservoir and pressure gauge, and downstream is the leak detector. The three conflats create an airtight chamber where the film can be tested. Copper fingers extending from the sample chamber are dipped in liquid nitrogen. The temperature of the system is regulated by the temperature controller.

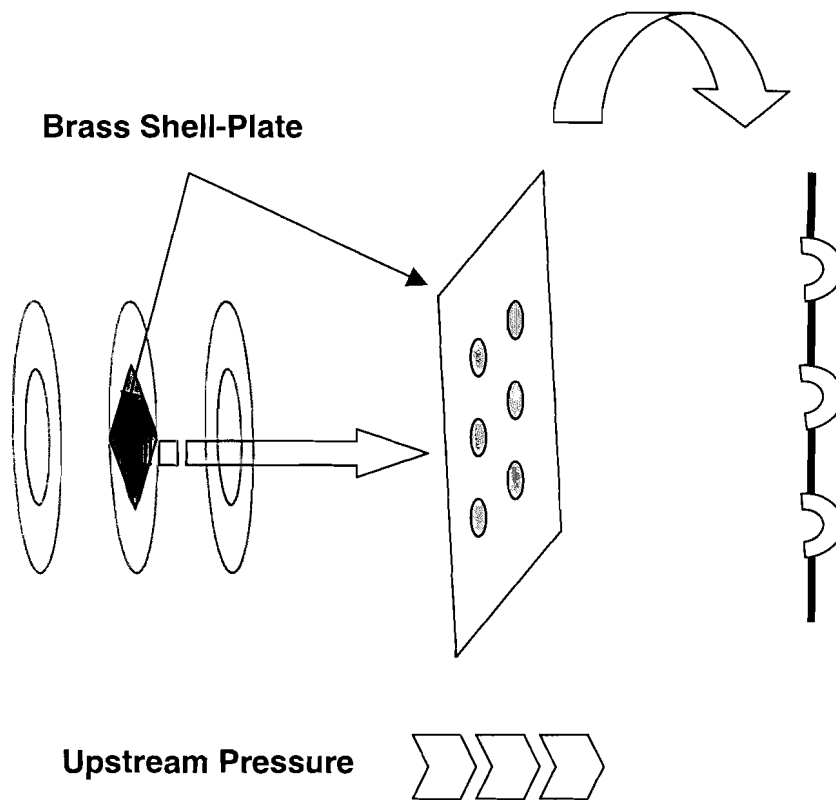


**FIGURE 3:** The design of the sample chamber. The shell holder was a brass plate with 6 holes drilled through it. Shells were glued to the plate using Epoxy glue and punctured on one side. The shell holder was attached to a conflat flange using Epoxy glue.

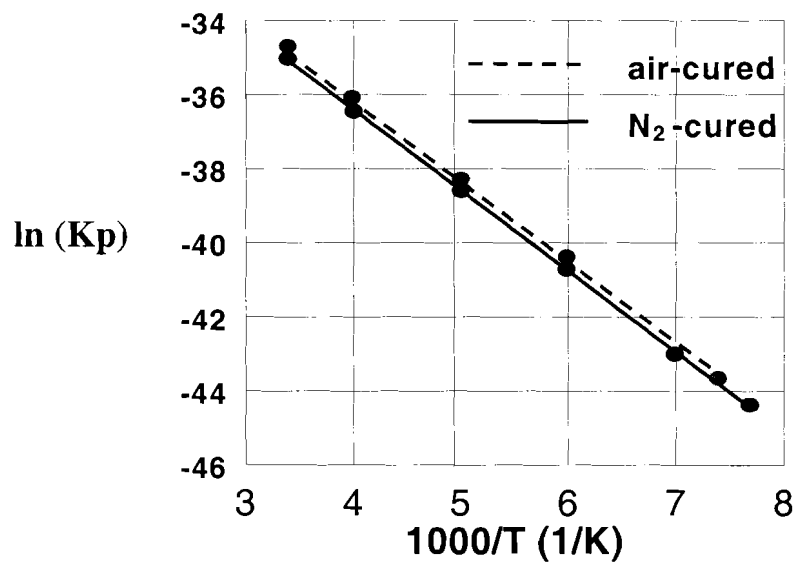


**FIGURE 4:** Temperature dependence of Helium  $K_p$  of air & N<sub>2</sub> cured samples.

$\frac{mol \cdot m}{sec \cdot Pa \cdot m^2}$	Time Constant	Flat-Film	Shell-plates
$K_p$	5.9E-16	4.6E-16	4.8E-16

**TABLE 1:** Comparison of the Helium permeability of polyimide measured using different setups. The permeability results of polyimide film tested in the flat-film setup were obtained from previous work.

$\frac{mol \cdot m}{sec \cdot Pa \cdot m^2}$		Temperature (K)			
		295	250	200	167
Curing Medium	Air	8.6E-16	2.4E-16	2.4E-17	3.0E-18
	N <sub>2</sub>	4.8E-16	1.2E-16	1.4E-17	1.6E-18

**TABLE 2:** Helium permeability of air & N<sub>2</sub> at cryogenic temperatures.

# **Inclusion Models of Laser Damage**

**Jeffrey Wilbur**

**Victor Senior High School**

**LLE Advisor: Prof. John C. Lambropoulos**

**Summer 2001**

## **ABSTRACT**

Inclusion models of laser damage were constructed using Mathematica v. 4.0. These models predict the effect of the inclusion interface on the damage threshold, by comparing inclusions with perfect and totally imperfect interfaces. The perfect interface models were based on the Goldenberg and Tranter heat conduction solution. With these models, the effects of variables such as pulse length and inclusion radius could be studied. An equation for the totally imperfect interface was then developed using relationships between these variables, and by taking into account that no heat conduction occurs between this interface and the surrounding matrix. With these models, scaling of the damage threshold was developed, and the models showed the effects of the different initial interfaces.

## **1. OVERVIEW**

### **1.1 Introduction**

Today, the study of laser damage is one of the most important and rapidly advancing fields in all of laser physics. This field of study investigates all aspects of damage in the laser system, ranging from physical damage on the laser, the lens, and the target, to the theoretical study of why this damage is occurring. This research is instrumental in the future of laser physics, and it is these various lens defects which are becoming a prominent obstacle in the creation of an efficient and practical laser-based system. The damage caused by lens defects is extremely costly, and prevents the laser system from working to its full potential. If this damage can be prevented, thousands of dollars can be saved, and the laser systems will be more efficient and productive.

### **1.2 Outline**

To work with the theoretical aspect of why laser damage occurs in the optics of the laser, it was necessary to create computational models that duplicated the physical properties of the laser lens. To develop these models, programs were created and conditions were simulated using

Mathematica v. 4.0. With the assistance of this program, the necessary calculations could be constructed and organized.

In order to correctly duplicate the physical properties of the lens, its material properties, as well as those of the defect, were examined. The material properties that were investigated mainly dealt with the properties of the absorbing inclusion, which were density, specific heat, thermal conductivity, and thermal diffusivity. Since these properties vary according to the composition of the defect, the calculations were performed using values from the most common types of inclusions.

After reviewing the physical properties of the absorbing inclusion, it was also necessary to consider the thermal interaction (heat conduction and heat flux) between the defect and the surrounding lens matrix. To examine this interaction, the investigation of the interface between these two materials was crucial. The two interface models used for these calculations were the perfect and totally imperfect interfaces. These types of interfaces are the extreme possibilities, and although they rarely occur, they provide the limits to a range of simulations in which all other interfaces are included.

After taking into account many of the possible variables that influence laser damage, the computational models could be run. These models were created using the laws of thermodynamics and the heat conduction equation, as well as the Goldenberg and Tranter solution (when looking at the perfect interface model). Through experimentation and simulation of different combinations of variables, I studied the effect of the radius of the inclusion on the damage threshold of the inclusion: it was determined that a specific combination of variables produced a worst case scenario. In this scenario, the lens was most prone to melting and damage. After this situation was examined, the effect of the individual variables was also determined, and a scaling of damage threshold for both the perfect and totally imperfect interface was constructed.

## **2. DEVELOPMENT OF INCLUSION MODELS**

### **2.1 Absorbing Inclusion Inside Non-Absorbing Matrix**

In order to set up the theoretical calculations in Mathematica, the physical properties of an inclusion model had to be duplicated. The model that was simulated was an absorbing spherical inclusion embedded inside a non-absorbing infinite matrix. In this model, the defect is located inside the non-absorbing lens. This is important because as the laser light is passed through the lens, the inclusion is the only material that will absorb any of the energy from the laser. The other light passing through the lens matrix is not absorbed, and does not have any effect on the system.

When programming this model into Mathematica, it was also necessary to make assumptions about the properties of defect, the interface, the matrix, heat flux, the laser pulse,

and the rise time of the laser. These assumptions simplified the calculations so that a general model could be used for all of the calculations. The first assumption that was made concerned the idea of how the inclusion absorbed energy from the laser. In this model, it was assumed that the energy absorbed by the inclusion was equal to the laser's energy flux ( $J/m^2$ ) multiplied by the inclusion cross sectional area ( $\pi R^2$  for a spherical inclusion of radius R.) There were also assumptions regarding the point at which damage actually occurs. In this model, it was assumed that damage occurs when the temperature at the center of the inclusion is equal to the inclusion's melting point.

The assumptions regarding the interface dealt with the difference between the perfect and imperfect interface. For the perfect interface, it was assumed that this interface allowed for complete heat conduction between the inclusion and the surrounding matrix. The opposite was assumed for the totally imperfect interface. In this interface, it was assumed that the interface was so insulating that it did not allow for any heat conduction or energy flow between the two materials. The shape and rise time of the laser pulse were also assumed. For this model, it was assumed that there was no rise time for the laser, meaning that as soon as the laser was activated, the beam was at its maximum power. Although these two assumptions are not very practical, because the laser pulse generally does have a curved shape with a rise time, they were used to develop the general model. The last assumption that was used in the creation of this inclusion model was that heat absorption is instantaneous and uniform over the inclusion. This was done to assure that the whole defect was affected by the laser energy, and that absorption was uniform across the whole inclusion.

The assumptions are summarized as follows:

Spherical inclusion;

Inclusion absorbs energy =  $(E \pi R^2)$ ;

Damage occurs when  $T_{center} = T_{mp}$ ;

Perfect interface: Complete heat conduction across interface;

Totally imperfect interface: No heat conduction across interface;

Laser: Square pulse shape and no rise time;

Instantaneous and uniform heat absorption.

## 2.2 Interface Equations

After the physical properties of the inclusion model had been created, the Mathematica v. 4.0 equations had to be designed and programmed. For these equations, the problem was divided into two different sections. One section deals with the perfect interface, and the other dealing with the totally imperfect interface. Each of these interface models needed a different equation because they each had different physical properties. For the perfect interface scenario, the Mathematica program could be based on the Goldenberg and Tranter solution [1952]. This

equation was used because it considered the effects of heat conduction across the perfect interface, and it allowed for the comparison between the damage threshold and the size of the inclusion. See Appendix 1 for a copy of the Mathematica v. 4.0 program [Wolfram, 1996].

The Goldenberg Tranter result for the perfectly conducting interface is

$$T_{\text{center}} = (R^2 A / k_1) F[k_1/k_2, tp D_1/R^2, (\rho_1 C_1)/(\rho_2 C_2)] \quad (1)$$

Here subscript 1 denotes the inclusion, and subscript 2 the matrix.  $k$  is thermal conductivity (W/m.K),  $D$  is thermal diffusivity (m<sup>2</sup>/s),  $tp$  is pulse duration,  $R$  is the inclusion radius,  $\rho$  is mass density (kg/m<sup>3</sup>), and  $C$  is heat capacity (J/kg.K). The quantity  $A$  (units W/m<sup>3</sup>) is power absorbed per unit volume in the inclusion, and found from the absorbed energy ( $E \pi R^2$ ) divided by the pulse duration ( $t$ ) and the inclusion volume ( $4 \pi R^3/3$ ). The form of the function  $F$  can be found in Goldenberg and Tranter [1952].

For the totally imperfect interface scenario, a new equation had to be created. In order to develop this formula, it was necessary to review the equation relating energy absorbed  $Q$  and temperature change  $\Delta T$  in a body of mass  $m$  and specific heat  $C$ :

$$Q = m C \Delta T \quad (2)$$

In order to manipulate this into a useable formula, it was necessary to substitute in for the mass  $m$ . Since mass is equal to density  $\rho$  multiplied by volume  $V$ , those new equations could be inserted instead in place of the mass:

$$E \pi R^2 = \rho V C \Delta T, \text{ or}$$

$$(E \pi R^2) = \rho (4/3 \pi R^3) C \Delta T \quad (3)$$

This formula could then be solved for the temperature change  $\Delta T$  and manipulated into a form that could be programmed into Mathematica. The result for the temperature rise at the center of inclusion with the totally imperfect interface equation is

$$T_{\text{center}} = 3E / [4R * (\rho C)] \quad (4)$$

## 2.2 Material Properties

After the perfect and totally imperfect interface equations had been programmed in Mathematica, their variables needed to be researched and examined. The variables that needed to be researched for the two equations were density, specific heat (at both room temperature of

three hundred degrees K and one thousand degrees K), and thermal conductivity (at both three hundred degrees K and one thousand degrees K). In order for this data to be relevant, these properties were recorded for thirteen different, but common defect materials. After recording all the values, it was then possible to further investigate the properties of these variables. For each defect material, both  $(\rho C)$  and thermal diffusivity ( $D = k / (\rho C)$ ) were calculated and their values were compared for all the materials, see Appendix 2.

The interesting fact that was discovered from this comparison was that while the density, thermal conductivity, and thermal diffusivity differed greatly among the various materials, the value of  $(\rho C)$  remained approximately constant. This was an important discovery which allowed the interface equations to be simplified by removing the variable  $(\rho C)$ . Since the  $(\rho C)$  value was approximately constant for all defect materials, it would not have any distinct influence in the damage threshold calculations.

### 3. CALCULATION RESULTS

#### 3.1 Procedure

The object of the interface calculations was to determine if a minimum radius  $R_{\min}$  existed, and if it caused a minimum damage threshold  $E_{\min}$ . In order to answer these questions, it was necessary to perform many calculations using the interface equations programmed into Mathematica. For each calculation, one variable was changed to determine how it affected both the  $R_{\min}$  and  $E_{\min}$  values. For each test, it was also necessary to determine the smallest  $R_{\min}$  value in order to calculate an accurate damage threshold value. While one variable was being tested, all others were kept constant to ensure that the calculations illustrated only the effects of one variable. After completing the calculations for the variable, the results were graphed and analyzed. The different variables tested were thermal conductivity of the inclusion ( $k_1$ ), thermal conductivity of the matrix ( $k_2$ ), thermal diffusivity of the inclusion ( $D_1$ ), time pulse of the laser ( $tp$ ), and the melting point of the inclusion ( $T_{mp}$ ),

#### 3.2 Perfect Interface Results

The first calculations that were done with the perfect interface equation revolved around determining the damage threshold of the inclusion. In these calculations, the initial goal was to compare the size of the inclusion to the damage threshold at that point. In these damage threshold calculations, the radius size  $R$  varied from  $0.1 \times 10^{-6}$  meters ( $0.1 \mu\text{m}$ ) to  $3 \times 10^{-6}$  meters ( $3 \mu\text{m}$ ).

After these results were graphed, an interesting fact was revealed, see Fig. 1. The graphs showed that there was a specific defect size ( $R_{\min}$ ) that caused the damage threshold to be at its lowest point ( $E_{\min}$ ). This showed that there was a worst defect size where the lens was most prone to damage. This calculation was then recreated using various pulse times  $tp$ , from  $1 \times 10^{-9}$

seconds to  $50 \times 10^{-9}$  seconds. These calculations also showed that the worst defect size existed at all the various time pulse lengths, although both the  $R_{\min}$  and  $E_{\text{cmin}}$  values changed at the different time pulse values  $t_p$ .

After comparing how the time pulse influenced the  $R_{\min}$  and  $E_{\text{cmin}}$  values, it was time to calculate the effects of the other variables: thermal conductivity of both the inclusion and matrix, ( $\rho C$ ), thermal diffusivity of the inclusion, and the melting point of the inclusion. In these calculations, both the  $R_{\min}$  and  $E_{\text{cmin}}$  values were calculated while observing the effects of the other variables.

After repeating the damage threshold calculations with the inclusion's melting point as the variable, it was observed that the  $E_{\text{cmin}}$  varied proportionally to melting point, see Fig. 2, while the melting point had no effect on the value of  $R_{\min}$ , see Fig. 3.

After repeating the damage threshold and minimum radius calculations with the time pulse of the laser as the variable, it was observed that both  $E_{\text{cmin}}$  and  $R_{\min}$  varied proportionally to the square root of the time pulse  $t_p$ . See Figures 4 and 5.

Then, the damage threshold and minimum radius calculations were repeated using first, the thermal conductivity of the matrix as the variable, and then, using ( $\rho C$ ) as the variable. With the thermal conductivity as the variable, it was observed that both  $E_{\text{cmin}}$  and  $R_{\min}$  varied proportionally to the square root of the thermal conductivity. With ( $\rho C$ ) as the variable, it was observed that  $E_{\text{cmin}}$  also varied proportionally to the square root of ( $\rho C$ ), see Fig. 6, but  $R_{\min}$  varied proportionally to the negative square root of ( $\rho C$ ), see Fig. 7.

### 3.3 Scaling of $E_{\text{cmin}}$ and $R_{\min}$

After observing the results from the perfect interface calculations, the relationships between the different variables (thermal conductivity, time pulse, melting point, ( $\rho C$ ), and both  $E_{\text{cmin}}$  and  $R_{\min}$  were revealed. By examining how each individual variable affected the damage threshold and minimum radius, two scaling equations were developed. These equations demonstrated the effects of the variables, and they helped to explain their relationship.

For the  $E_{\text{cmin}}$  scaling equation, each variable relationship was taken into account and examined. The calculations demonstrated that  $E_{\text{cmin}}$  varied as the square root of the time pulse, ( $\rho C$ ), and the thermal conductivity of the matrix, while varying proportionally to the melting point. Taking this data into account, and by matching the correct units, the  $E_{\text{cmin}}$  scaling equation was developed.

$$E_{\text{cmin}} = T_{\text{mp}} [t_p k_2 (\rho C)]^{1/2} f(k_1 / k_2) \quad (5)$$

with  $f$  a dimensionless function, see Fig. 8.

For the  $R_{\min}$  scaling equation each variable relationship was taken into account and examined. The calculations demonstrated that  $R_{\min}$  varied as the square root of the time pulse and the thermal conductivity of the matrix, but it varied as the negative square root of  $(\rho C)$ . They also showed that the melting point of the equation had no effect on the value of  $R_{\min}$ . Taking this data into account, and by matching the correct units, the  $R_{\min}$  scaling equation was developed.

$$R_{\min} = [tp \ k_2 * (\rho C)]^{1/2} \ g(k_1 / k_2) \quad (6)$$

Here, again,  $g$  is a dimensionless function, see Fig. 9.

### 3.4 Totally Imperfect Interface Results

For the totally imperfect interface calculations, the major objective was to determine the relationship between size of the inclusion and the inclusion's damage threshold. In order to find this relationship, it was necessary to use the imperfect interface equation that had been programmed into Mathematica. Since there was no heat flux or conduction across the totally imperfect interface, the calculation was much simpler. With thermal conductivity and diffusivity removed from the equation,  $E_{\min}$  was now proportional to the inclusion size  $R_{\min}$ . These calculations also showed that the damage threshold was not affected by the time pulse  $tp$  of the laser. These results are shown schematically in Fig. 10. In this scenario, the data shows that there is not an inclusion size that is most prone to damage, and only the melting point of the inclusion will determine how predisposed the inclusion site is to melting.

## 4. CONCLUSIONS

After reviewing the results of both the damage threshold and inclusion size calculations, the relationships of the different variables was established. These relationships were displayed in both the  $E_{\min}$  and  $R_{\min}$  scaling equations, and they helped to guide both the perfect and totally imperfect interface models. From these damage threshold calculations, it was determined that with the imperfect interface, the damage threshold was proportional to the radius of the inclusion multiplied by the time pulse of the laser. Although this information is very useful, the most important conclusion that can be drawn from these calculations is the idea that with a perfect interface, a worst defect size exists. At this worst size radius size, the damage threshold of the inclusion is at its lowest value, creating a situation where the inclusion is most prone to melting and damage. In these specific calculations, the worst defect size ranged from 40 to 300 nm, but this range is dependent on the material properties of the inclusion.

This idea of a worst defect size is very important to controlling the problem of laser lens damage. Knowing that a worst defect size will cause the most damage, it is important to look at

how to prevent the creation of this size defect. Since there is no way to control many of the natural inclusions that form in lenses, it is important to prevent inadvertent defects. When the lens is polished or coated, the size of the polishing abrasive slurry must be examined. Since polishing leaves some inadvertent defects in the lens, it is necessary to be sure these defects are not of the worst size. By first examining the size range of the worst defect, it would then be possible to use a polishing method that is less likely to cause this size defect. The polishing would still leave some inadvertent defects, but they would not be the size which is most prone to damage.

## **5. SUGGESTIONS FOR FURTHER WORK**

To further investigate how these calculations simulate the physical process of laser damage, it would be important to examine the effect of the laser's pulse shape and rise time. In our calculations, it was assumed that the laser had a square pulse shape and no rise time. In actuality, the laser does have a curved pulse shape and a rise time. In future work, to make these calculations more realistic, it might be important to investigate how the laser's properties influence the damage threshold and minimum size of the inclusion.

Another area to look at for further work would be in the details of absorption and heat transfer. It might be worth looking into how different wavelengths of light are absorbed by the inclusion, and if any specific wavelength has a greater effect on the damage threshold calculation. When looking at the details of heat transfer, it would be important to examine heat flux. More investigation is needed to determine if heat flux is instantaneous, and how a delayed heat flux might change the damage threshold calculations.

## **REFERENCES**

- Cengel, Yunus A. *Heat Transfer: A Practical Approach*. New York: The McGraw-Hill Companies, (1998).
- Exarhos, Gregory J. *Laser-Induced Damage in Optical Materials: 1998*. New York: The International Society for Optical Engineering, 1999.
- Goldenberg H. and M. A. Tranter M. A., Heat flow in an infinite medium heated by a sphere, *British Journal of Applied Physics*, vol. 3, pp. 296-298, 1952.
- International Critical Tables of Numerical Data, Physics, Chemistry, and Technology*. The McGraw-Hill Companies: New York, 1993.
- Stephen Wolfram. *The Mathematica Book*. Illinois: Wolfram Media, 1996.
- Touloukian, Y.S. *Thermophysical Properties of Matter and Substances*. Amerind Publishing Co., Washington DC, 1974.
- Wolf, Jonathan S. *AP Physics B*. Barron's, 1995.

```
In[156]:= f[R_, D1_, k1_, k2_, tp_, y_] :=
  (
    (Exp[-((y^2 * tp) / (R^2 / D1))] / y) *
    (
      (Sin [y] - (y * Cos[y])) /
      (
        ((1 - (k2/k1)) * Sin[y] - (y * Cos[y]))^2 +
        ((k2/k1) * y^2 * Sin[y]^2)
      )
    )
  )
```

```
In[157]:= a[R_, D1_, k1_, k2_, tp_, ymax_] := NIntegrate[f[R, D1, k1, k2, tp, y],
  {y, 0, ymax}, MinRecursion -> 0, MaxRecursion -> 100000]
```

```
In[158]:= try[ymax_] := NIntegrate[f[.01*10^-6, 3.5*10^-6, 8, 1.38, 30*10^-9, y],
  {y, 0, ymax}, MinRecursion -> 0, MaxRecursion -> 100000]
```

```
In[154]:= try[1]
```

```
Out[154]= 0.306125
```

```
In[160]:= try[1.2]
```

```
Out[160]= 0.306125
```

```
In[161]:=
```

```
a[.01*10^-6, 3.5*10^-6, 8, 1.38, 30*10^-9, 1.2]
```

```
Out[161]= 0.306125
```

```
In[162]:=
```

```
b[k1_, tp_, Tmp_, R_] := ((4 * k1 * tp * Tmp) / (3 * R))
b[8, 30*10^-9, 2000, .01*10^-6]
```

```
Out[163]= 64000.
```

```
In[164]:= c[k1_, k2_, R_, D1_, tp_, ymax_] := (1 /
  ((1/3) * (k1/k2) + (1/6) - ((2/ Pi) * Sqrt[k2/k1] * a[R, D1, k1, k2, tp, ymax])))
```

```
In[165]:= c[8, 1.38, .01*10^-6, 3.5*10^-6, 30*10^-9, 1.2]
```

```
Out[165]= 0.495518
```

```
In[166]:= Ec[k1_, tp_, Tmp_, R_, k2_, D1_, ymax_] :=
  b[k1, tp, Tmp, R] * c[k1, k2, R, D1, tp, ymax]
```

```
In[170]:= Ec[8, 30*10^-9, 2000, .01*10^-6, 1.38, 3.5*10^-6, 1.2]
```

```
Out[170]= 31713.1
```

## Material Properties

	P	C @ 300 K	C @ 1000 K	K @ 300 K	K @ 1000 K	W/(m <sup>2</sup> C)	W/(m <sup>2</sup> C)	PC @ 300 K	PC @ 1000 K	D @ 300 K
Units	kg/m <sup>3</sup>	J/(kg * C)	J/(kg*C)	W/(m <sup>2</sup> C)	W/(m <sup>2</sup> C)	W/(m <sup>2</sup> C)	W/(m <sup>2</sup> C)	J/(m <sup>2</sup> s)	J/(m <sup>2</sup> s)	m <sup>2</sup> /s
Au	19300	129	x	317	x	x	x	2.50E+06	2.50E+06	0.0001268
Al2O3	3960	756	1176	50	10	10	10	3.10E+06	3.10E+06	1.66667E-05
BeO	2980	1050	1890	275	50	50	50	3.10E+06	3.10E+06	8.87097E-05
CaF2	3170	924	1092	9.5	4	4	4	2.90E+06	2.90E+06	3.27586E-06
CaCO3	2940	840	840	3.5	1.5	1.5	1.5	2.50E+06	2.50E+06	0.0000014
GaAs	5316	315	357	33	27.5	27.5	27.5	1.70E+06	1.70E+06	1.94118E-05
HfO2	9680	294	378	1.75	1.75	1.75	1.75	2.80E+06	2.80E+06	0.000000625
MgF2	3110	1008	1260	33	x	x	x	3.10E+06	3.10E+06	1.06452E-05
MgO	3590	1050	1260	55	9	9	9	3.80E+06	3.80E+06	1.44737E-05
Si	2320	735	840	140	312	312	312	1.70E+06	1.70E+06	8.23529E-05
ThO2	10009	231	315	8	3.5	3.5	3.5	2.30E+06	2.30E+06	3.47826E-06
TiO2	4100	420	588	25	3.5	3.5	3.5	1.70E+06	1.70E+06	1.47059E-05
Y2O3	5010	420	630	0.95	1.6	1.6	1.6	2.10E+06	2.10E+06	4.52381E-07
max/min	834	813	6	33368	208	208	208	2.25	2.25	281

# Laser Damage Thresholds

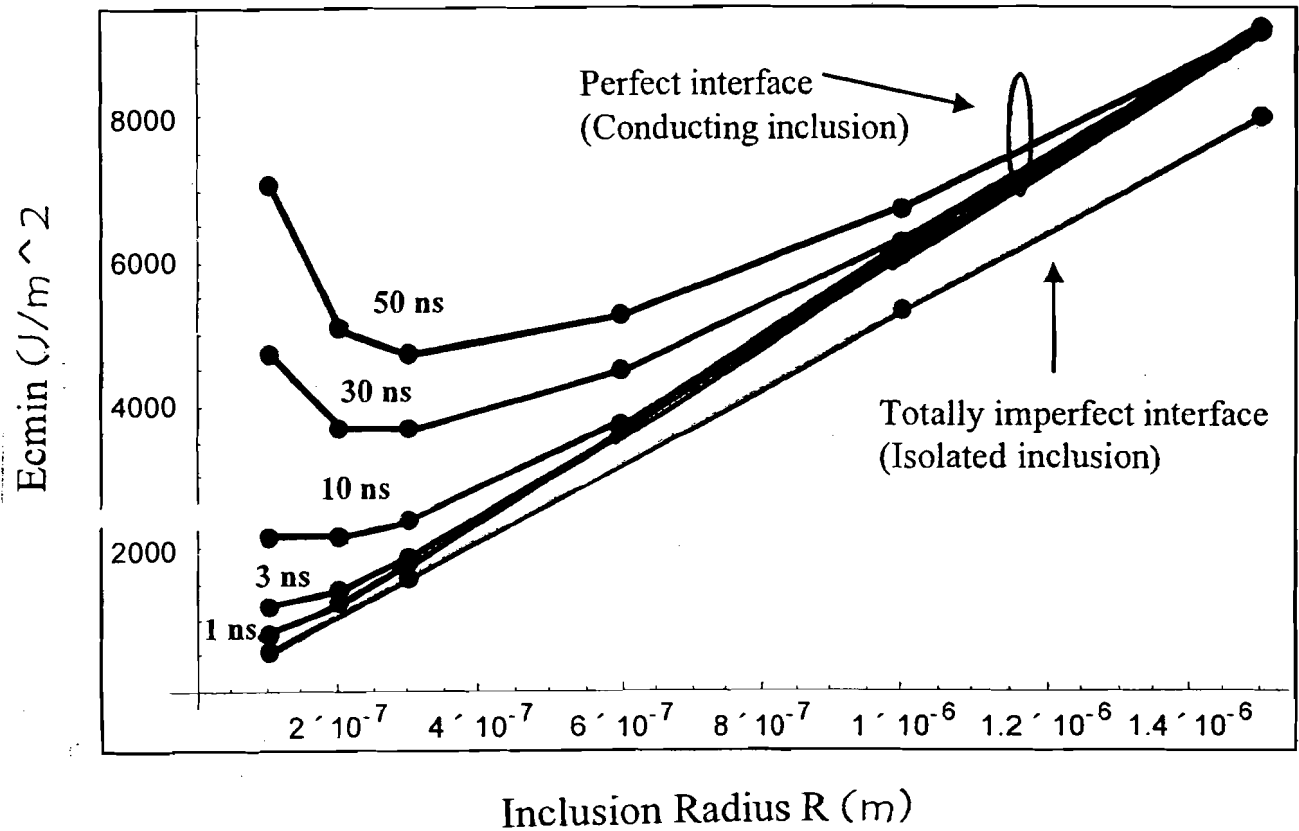


FIG. 1 The dependence of the laser damage threshold on inclusion radius  $R$  for various pulse durations  $t_p$ . The graph demonstrates the concept of minimum damage threshold. The graph also shows the result for the insulated inclusion (case of totally imperfect interface.)

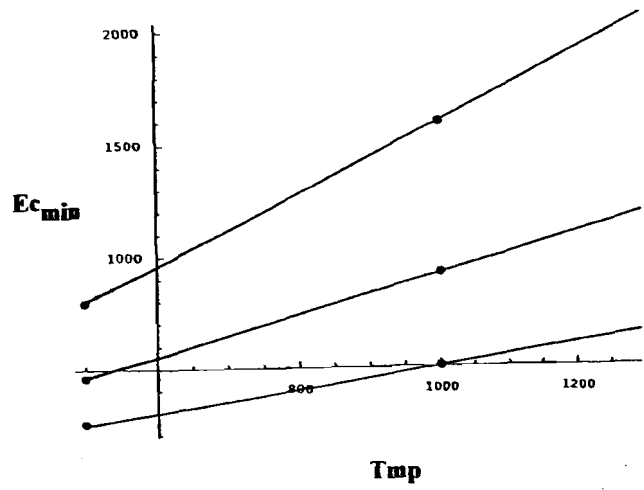


FIG. 2 Dependence of minimum laser damage threshold ( $J/m^2$ ) on the inclusion melting point (K).

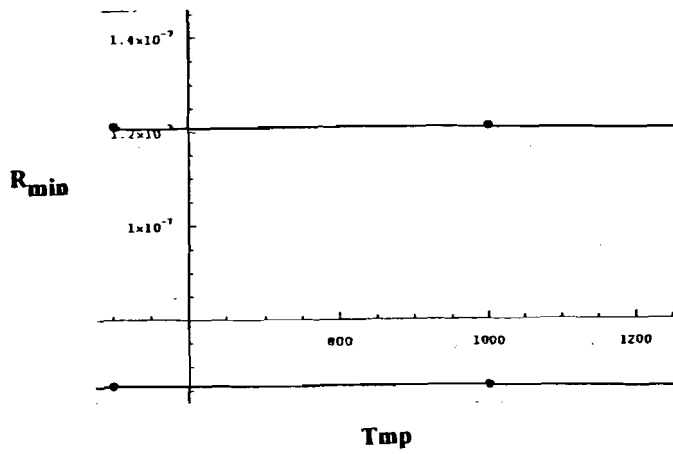


FIG. 3 Dependence of minimum inclusion size  $R_{min}$  ( $\mu m$ ) on inclusion melting point for two different pulse durations,  $t_p = 10$  ns (top) and  $t_p = 1$  ns.

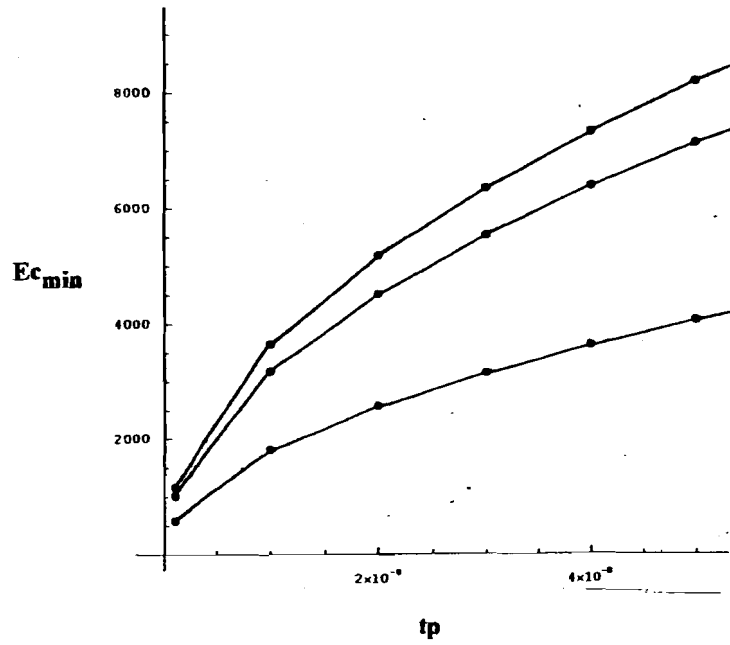


FIG. 4 Dependence of laser damage threshold ( $J/m^2$ ) on pulse duration (s).

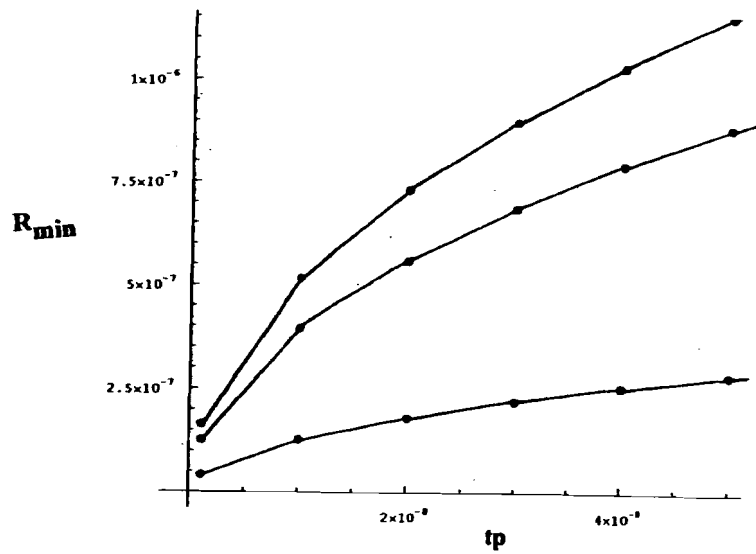


FIG. 5 Dependence of minimum inclusion size  $R_{min}$  (worst defect radius, m) on pulse duration (s).

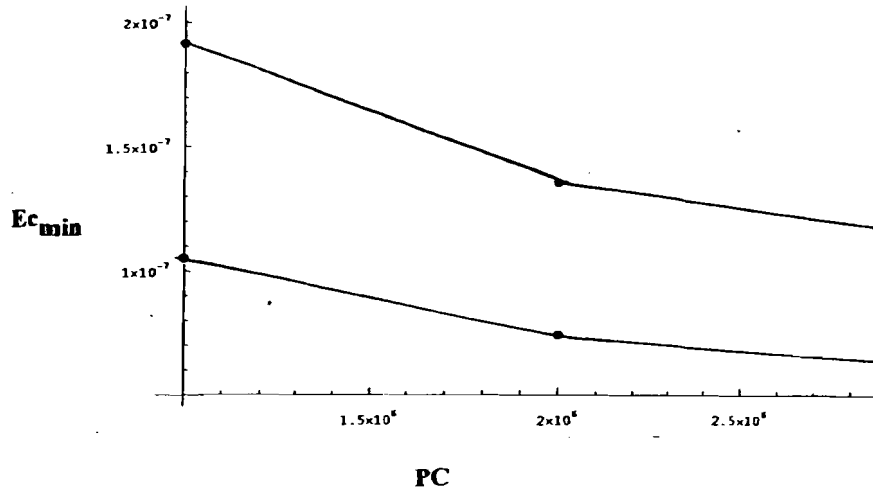


FIG. 6 Dependence of laser damage threshold ( $J/m^2$ ) on the product of mass density and heat capacity (product has units  $J/m^3.K$ ).

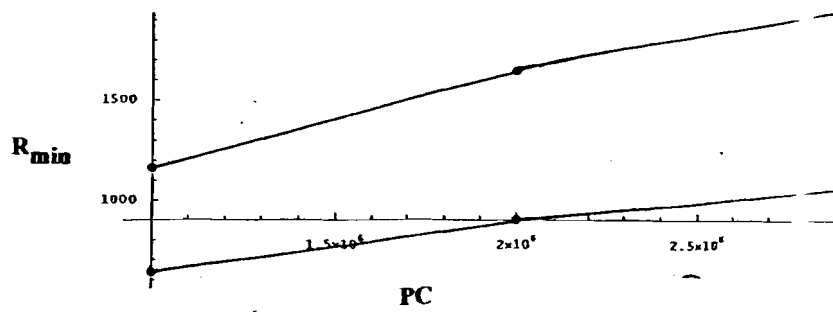


FIG. 7 Dependence of minimum inclusion size  $R_{min}$  (worst defect radius, m) on the product of mass density and heat capacity (product has units  $J/m^3.K$ ).

## SCALING: Minimum Areal Energy Density

---

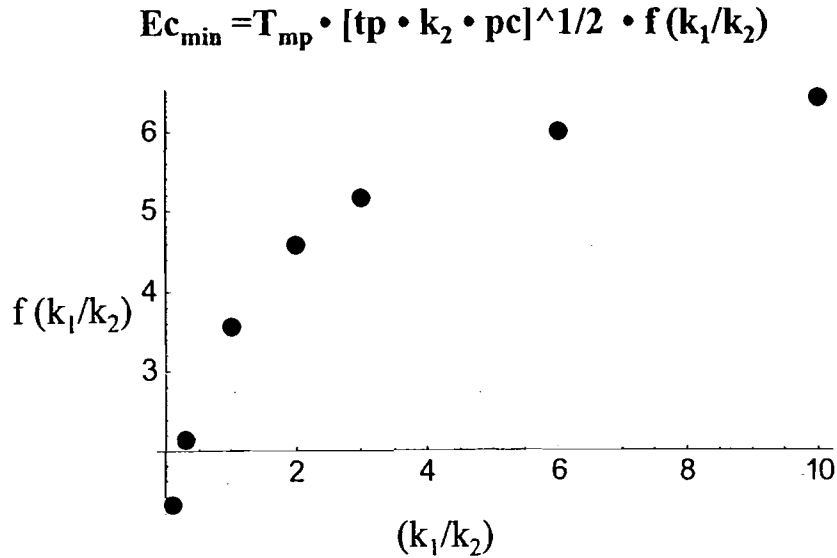


FIG. 8 Scaling of laser damage threshold  $E_{c_{min}} = T_{mp} [tp \cdot k_2 (\rho C)]^{1/2} f(k_1/k_2)$  on pulse duration  $tp$  and thermophysical properties of the matrix and inclusion. The function  $f$  is dimensionless.

## SCALING: Worst Defect Size

---

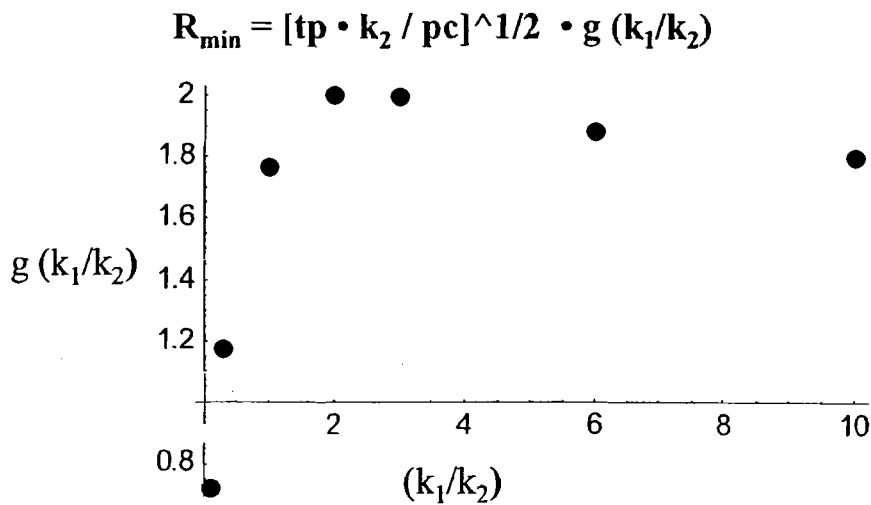


FIG. 9 Scaling of the minimum inclusion size  $R_{min}$  (worst defect radius)  $R_{min} = [tp \cdot k_2 \cdot (\rho C)]^{1/2} g(k_1/k_2)$ . The function  $g$  is dimensionless.

## Scaling: Effect of Interface

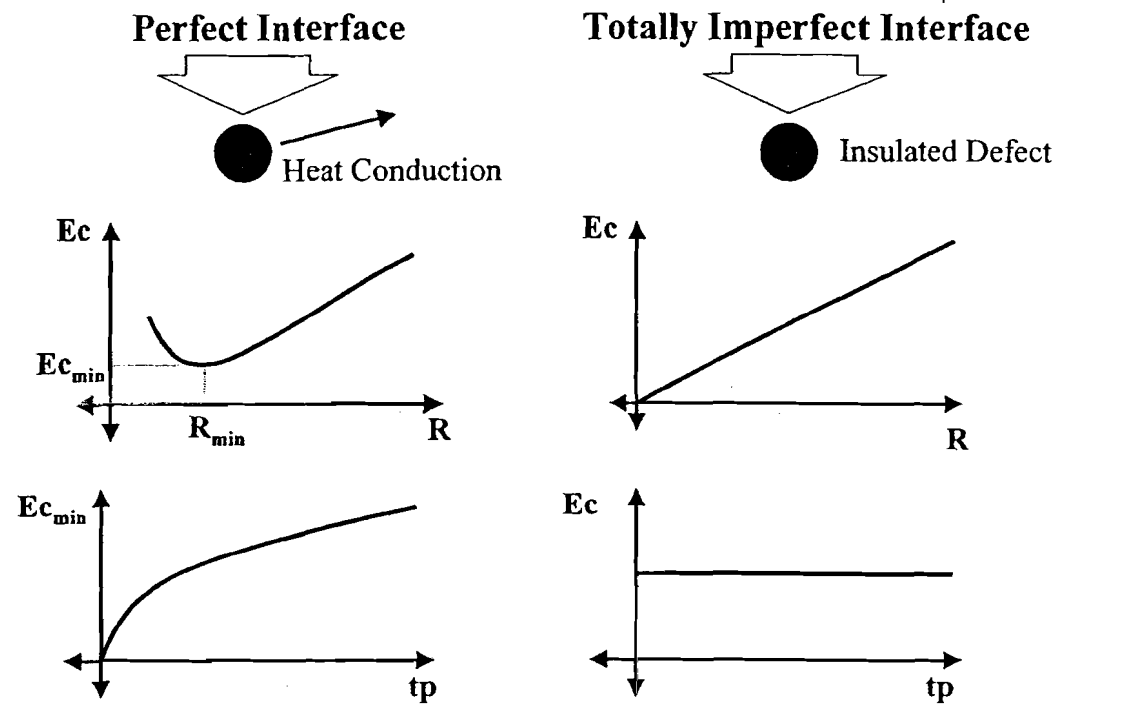


FIG. 10 Scaling of damage threshold ( $J/m^2$ ) on inclusion size and pulse duration for the case of the totally imperfect (insulating) inclusion.